MAGNETIC AND THERMAL PROPERTIES OF LOW-DIMENSIONAL SINGLE-CRYSTALLINE TRANSITION-METAL ANTIMONATES AND TANTALATES

by

Aaron Brandon Christian

A dissertation submitted in partial fulfillment
of the requirements for the degree

of

Doctor of Philosophy

in

Physics

MONTANA STATE UNIVERSITY
Bozeman, Montana

April 2017

DEDICATION

I dedicate this work to my mother, who showed me the world and instilled in me a profound wonder for it; and to my father, who cultivated that wonder by often asking Socratic questions. Both have been an encouraging driving force that allowed me to fulfill this accomplishment. Without them, I would be nothing more than a curious dreamer.

ACKNOWLEDGEMENTS

I would like to thank my advisor, Dr. John Neumeier, for introducing me to the interesting world of low-dimensional magnetism that has been central to this dissertation. His insight, and that of our collaborators, Dr. Mike Smith and Dr. Yi-Kuo Yu, have been considerably valuable to this work. I would also like to thank Dr. Alwyn Rebello for his mentorship in the laboratory during his time as a postdoctoral researcher. Additionally, I am immensely grateful to my colleagues: Jared Rice, David Buckingham, Aaron Schye, and Clay Hunt, who provided enduring friendships in dark times and in light.

Furthermore, I give thanks to my graduate committee as a whole; Drs. John Neumeier, Yves Idzerda, Recep Avci, Shannon Willoughby, and Randy Babbitt; and to the exceptionally helpful office staff and faculty, Margaret Jarrett, Sarah Barutha, Sherry Heis, Jodie Hirsch, Jeremy Gay, Norman Williams, Bo Glaspey, Larry Springer, and the countless others who work behind the scenes to keep the Physics Department functioning like a well-oiled machine.

Funding Acknowledgment

This work was kindly supported by the National Science Foundation under Contract No. DMR-0907036; and by the U. S. Department of Energy under Grant No. DE-SC0016156.

TABLE OF CONTENTS

TABLE OF CONTENTS – CONTINUED

LIST OF TABLES

LIST OF FIGURES

LIST OF FIGURES – CONTINUED

ABSTRACT

This work contributes to the study of magnetic interactions in the low-dimensional antiferromagnets $M(\mathrm{Sb,Ta})_2\mathrm{O}_6$, where M is a transition metal. By virtue of the trirutile structure, M-O-O-M chains propagate along [110] at $z = 0$ and $[1\bar{1}0]$ at $z = 1/2$ of the unit cell. These chains are separated along [001] by sheets of weakly-interacting diamagnetic ions. The spin-exchange coupling perpendicular to the chains is weak, permitting the low-dimensional classification. Single crystals have been grown using chemical vapor deposition and the floating zone method. Magnetization, in-field heat capacity, and high-resolution thermal expansion measurements have been performed along various axes, revealing significant anisotropy due to the peculiar magnetic structures and low dimensionality.

The Néel temperature, T_N, at which long-range order occurs is found to be unstable against the application of magnetic field above 2 T. Large fields tend to lower T_N of the set of moments with projections along the applied field. Moments which are aligned perpendicular to the field are significantly less affected. This can lead to the formation of a secondary peak in heat capacity when magnetic field is along either [110] or $[1\bar{1}0]$. The change in heat capacity at the location of the newly formed peak means there is a change in entropy, which depends upon the direction of applied field with respect to the magnetic moments. Consequently, an anisotropic magnetocaloric effect arises due to the unique magnetic structure. The anisotropic nature of this effect has potential applications in magnetic refrigeration.

1. INTRODUCTION

In the early 1900s, the presiding theory of magnetism was that put forth by Pierre Weiss who suggested magnetic materials are comprised of domains of ordered magnetic moments (micromagnets on the atomic scale). The direction of magnetic alignment could vary greatly between adjacent domains, but certain crystallographic axes, referred to as *easy axes*, could be favored by the moments. In 1920, a paper by Wilhelm Lenz [1] introduced the concept of constraining the magnetic moments' degree of freedom, allowing them to only point either up or down. This model was further developed in 1924 when Lenz handed the problem over to Ernst Ising, his graduate student at the time [2]. Ising simplified the model by assuming only nearest-neighbor interactions along a chain of atoms, thus ushering the study of low-dimensional magnetism. He ultimately determined that long-range order could not be established for the one-dimension chain and erroneously concluded this result for two and three dimensions as well.

Over the next decade, the model was largely dismissed by the scientific community because it was considered merely as an approximation to the competing *Heisenberg* model, which did not constrain the moments to only two directions. A breakthrough was made in 1936 by Rudolf Peierls [3] who, in part, corrected Ising's error by showing that a transition to long-range order was in fact possible for the two- and three-dimensional cases. The theoretical merits of the Ising model were slowly recognized over the following decades, eventually resulting in an increasing flood of publications on topics ranging from the general properties of phase transitions to developments in the theories of alloys [4], adsorption [5], and cooperative or collective phenom-

ena [6]. It can thus be argued that Ising helped ignite the theory of low-dimensional magnetism that continues to intrigue scientists to this day.

For many years after its introduction, the field of low-dimensional magnetism remained largely theoretical. It was not until the later half of the 20^{th} century that physical manifestations could be realized in bulk materials in cases where the magnetic coupling is highly anisotropic. The transition-metal antimonates and tantalates investigated in this dissertation are examples of such compounds. However, the vast majority of prior research has been conducted on polycrystalline samples, preventing a thorough investigation of possible anisotropy in magnetic susceptibility, thermal expansion, and in-field heat capacity measurements. This fact motivates my investigation into the magnetic properties of *single-crystalline* samples in the current study.

Trirutile transition-metal antimony and tantalum oxides have the chemical formula $M^{2+}(\mathrm{Sb,Ta})_2^{5+}\mathrm{O}_6^{2-}$, where M is the transition metal. With the exception of $MnSb_2O_6$, these compounds possess similar crystal structures, with the transition-metal ion residing in an octahedral environment. The crystal structure for these compounds is shown in Fig. 1.1; two unit cells and two M-O_6 octahedra are shown to illustrate the fact that the apexes of the octahedra point along the [110] direction at $z = 0$ and the $[1\bar{1}0]$ direction at $z = 1/2$. The oxygen occupancy does not allow the apexes to point along $[1\bar{1}0]$ at $z = 0$, or those at $z = 1/2$ to point along [110]. Two neighboring apexes create M-O-O-M linkages (dominant exchange pathways) that are important for the formation of one-dimensional (1-d) antiferromagnetic (AFM) chains [7]. These linkages are evident upon inspection of Fig. 1.1.

The $M(\mathrm{Sb,Ta})_2O_6$ compounds exhibit a wide range of interesting electrical and magnetic properties, most notably of which is the reduced dimensionality of the antiferromagnetic interactions. Their Néel temperatures T_N (the temperature at which long-range AFM order occurs) are near 10 K, but short-range magnetic order is

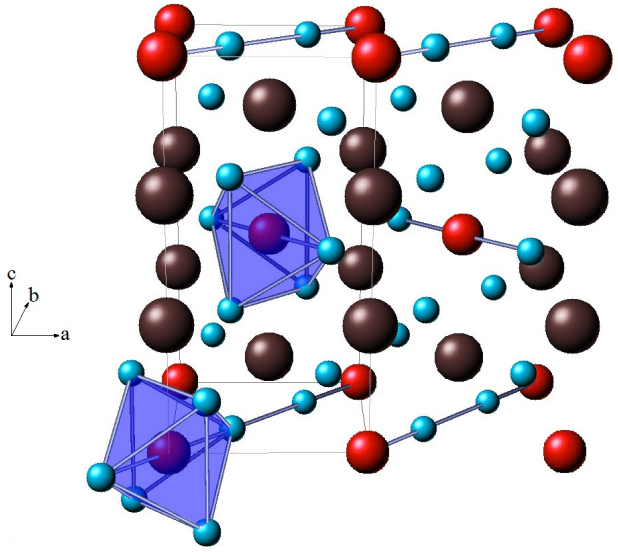

Figure 1.1: Tetragonal $P4_2/mnm$ crystal structure for $M(\mathrm{Sb,Ta})_2\mathrm{O}_6$. Except for the monoclinic distortion, this structure is valid for $\mathrm{CuSb_2O_6}$. The M atoms are red, oxygen atoms are blue, and (Sb,Ta) atoms are grey. The unit cell is illustrated by thin lines. The one-dimensional M-O-O-M linkages along the [110] and [1$\bar{1}$0] directions at $z = 0$ and $z = 1/2$, respectively, are illustrated by lines. Octaheda at $z = 0$ and $z = 1/2$ are shown; the apexes form the M-O-O-M linkages. Java Structure Viewer was used to create this figure.

evident [8, 9, 10, 11] well above T_N. Broad peaks in their magnetic susceptibilities indicate a deviation from the Curie-Weiss law of paramagnetism and are often characteristic of short-range antiferromagnetic order of magnetic moments on 1-d chains. The short-range nature of the order in this region is suggested by other measurements, such as Mössbauer spectroscopy [12] and heat capacity [9, 13]. In Mössbauer spectroscopy, the crystals are illuminated with gamma ray photons which can be absorbed by the atomic nuclei and re-emitted with less energy. The loss of photon energy occurs in discrete amounts equal to the energy emitted by the nuclei in the form of quantized vibrations of the lattice, called phonons. This technique is therefore able to probe minute changes in the energy levels of an atomic nucleus in response to its environment. Using this method, Takano and Takada [12] observed spectra for

$M\mathrm{Ta_2O_6}$ (M = Ni, Co, Fe) taken at 4.2 K, which demonstrated the coexistence of an internal magnetic field with an electric field gradient. According to them, this confirmed the presence of magnetic order.

The exchange coupling between the chains within $M(\mathrm{Sb,Ta})_2\mathrm{O_6}$ is typically weak [7, 14], which invites classification as quasi 1-d antiferromagnets. Short-range order, likely in the form of clusters of dimers, occurs below 100 K [15]. Long-range order is not expected for a 1-d chain of magnetic ions. However, they can undergo phase transitions (i.e., dimerization, or a spin-Peierls transition) through coupling with 3-d phonons [16, 17, 18]. Competition between nearest- and next-nearest-neighbor exchange energies (J_1 and J_2, respectively) is known to lead to spontaneous dimerization if the relationship between them is favorable [19].

1.1 Crystal Field Theory

To understand the magnetic structure, it is beneficial to review the influence of the ions' local environment on the shapes of the electron orbitals. In crystal field theory, the ligands (the ions that bind to a central metal ion to form a coordination complex) are considered as point charges. Their presence introduces an electric field at the central atom, resulting in a splitting of the d orbitals (a local *Stark Effect*). In an octahedral environment, like those in $M(\mathrm{Sb,Ta})_2\mathrm{O_6}$, the d orbitals split into three t_{2g} orbitals and two e_g orbitals. The difference in energy between the two sets of d orbitals is called the crystal field splitting energy, δ_o, where the subscript o stands for octahedral. The magnitude of the splitting depends on the charge on the transition metal ion, the principal quantum number, and the nature of the ligands. The lobes (the volumes in which there is high probability of finding the electrons) of the e_g

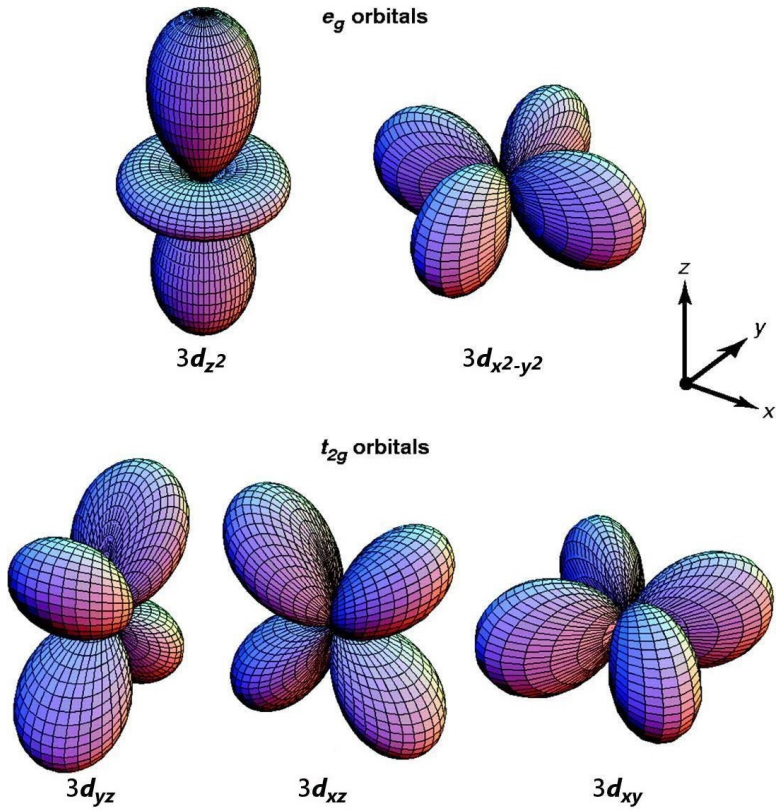

Figure 1.2: Angular distribution of the electron density of the d orbitals in an octahedral environment. The x, y, and z axes point to the vertices of the octahedron.

orbitals are directed toward the vertices of the octahedra (i.e. toward adjacent ions) while the t_{2g} orbitals are pointed along intermediate directions. (See Fig 1.2.) Large orbital overlap of the e_g orbitals with those of the ligands located at the vertices causes their electrostatic energy to be increased by $\frac{3}{5}\delta_o$. Likewise, the three t_{2g} orbitals each decrease in energy by $\frac{2}{5}\delta_o$. Therefore, the average change in energy due to the presence of the six negative ions at the vertices is zero.

The exchange energy P associated with Hund's first rule (which is the energy required to force two electrons to pair in the same orbital) discourages electrons from pairing in the t_{2g} orbitals. In the first row of transition metals from d^4 to d^7 ions,

P varies roughly from 2.48 eV to 3.72 eV, while δ_o ranges from 0.62 eV to 3.72 eV (for perspective, visible light contains photons with energies ranging from 1.8 eV to 3.1 eV). With such an overlap of energies, either energy can be greater depending upon the circumstance. If $\delta_o > P$, electrons will be forced into the lower orbitals and pair with each other, resulting in a low-spin configuration. On the other hand, if $\delta_o < P$, Hund's first rule applies and the electrons spread over the entire set of d orbitals, yielding the high-spin configuration [20].

1.1.1 Jahn-Teller Effect

When the ground state of an ion is degenerate, a geometric distortion occurs such that the degeneracy is lifted and a new equilibrium structure of lower symmetry is attained. This distortion is known as the Jahn-Teller effect [21]. To illustrate, if an odd number of electrons reside in the e_g orbitals, as is the case for Cu^{2+}, then the presence of the unpaired electron results in an imbalance of electrostatic forces leading to spontaneous symmetry breaking. In this situation, the orbitals along z are either stretched or compressed, which in turn distorts the arrangements of electrons in the x-y plane via the $3d_{x^2-y^2}$ suborbital. The orbital degeneracy is thus removed, further splitting the e_g and t_{2g} orbitals. (See Fig. 1.3 for an energy diagram.) The Jahn-Teller effect is said to be responsible for the monoclinic-to-tetragonal phase transition observed in $CuSb_2O_6$ at 380 K [22].

A weaker effect is observed when the unpaired electron(s) instead reside in the t_{2g} orbitals. This occurs for the high-spin configurations of Fe^{2+} and Co^{2+}. We can therefore anticipate a Jahn-Teller effect in $FeTa_2O_6$ and $Co(Sb,Ta)_2O_6$. These distortions can have an important effect on structural transitions and magnetic ordering.

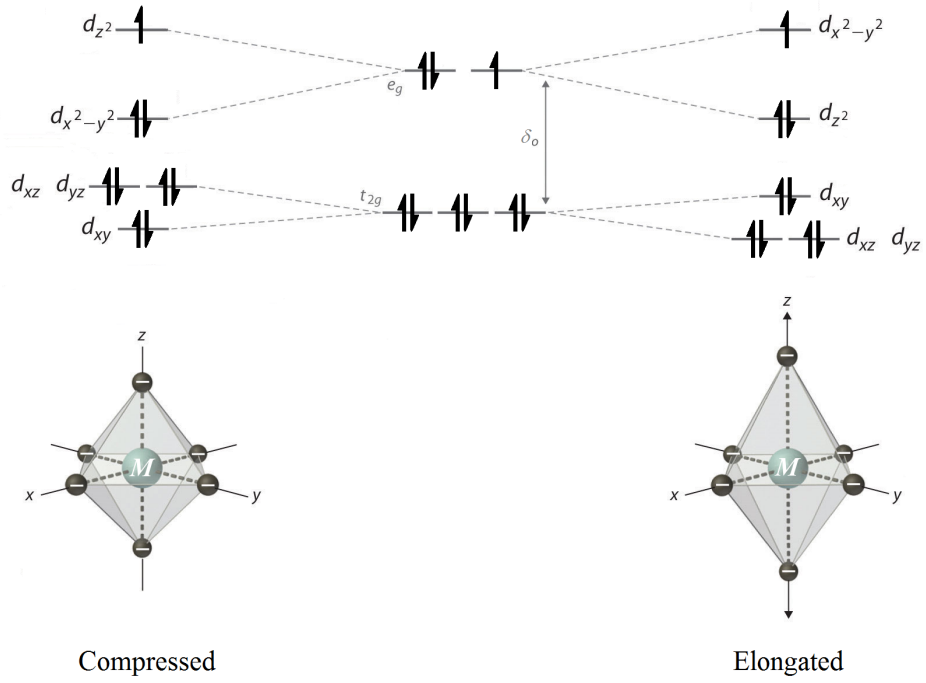

Figure 1.3: Jahn-Teller distortion of octahedral Cu^{2+}. When the unpaired electron resides in the d_{z^2} orbital (left), the octahedra is compressed along the z direction. Alternatively, an unpaired electron in the $d_{x^2-y^2}$ orbital (right) elongates the octahedra.

1.2 Superexchange

When magnetic ions are separated by nonmagnetic ions (i.e., those with all electron shells filled), a magnetic interaction can be mediated by the electrons in their nonmagnetic neighbors (often O^{2-}, as is the case for the current study). Magnetic order can then be established through *superexchange*. The orbital structure of the involved ions greatly influences this magnetic order. For example, the type of interaction (i.e. ferro- and antiferromagnetic) is influenced by the degeneracy and occupancy of the transition-metal orbitals. Meanwhile, the strength of the interaction is determined by the orbital overlap between those of the transition metal and the mediator

[23]. The more overlap between orbitals, the stronger the interaction will become. The overlap is determined both by the separation between the ions and the O-M-O angle. According to Whangbo *et al.* [24], an interaction should be considered strong if the separation between the two mediators (the O-O separation) is within the van der Waals distance (the distance that defines the size of the atom), and when both $\angle M$-O-O angles are in the range of 160° or larger. The fact that there are *two* mediating oxygen ions invites the nomenclature *super*-superexchange [24].

Qualitative super-superexchange pathways of interest are shown in Fig. 1.4. According to Hund's first rule, the electrons will fill the orbitals such that the outcome has a maximum spin multiplicity $(2S+1)$, where S is the quantum spin number. When an octahedral field splits the d orbital into three t_{2g} orbitals and two e_g orbitals, the former, having lower energy, fill up first. The $2p_x$, $2p_y$, and $2p_z$ orbitals of the O^{2-} ion are fully occupied. This arrangement allows for antiferromagnetic order to occur by the virtual sharing of electrons. On the left side of Fig. 1.4, spin-down electrons from the oxygen ion are able to temporarily occupy one of the unfilled orbitals of the transition-metal ion. During the electron's absence, a spin-down electron from the second oxygen is able to occupy the half-filled p orbital of the first. The only way for the transition metal on the right to share an electron would be if it contains an unpaired electron in the spin-down state. The ion (or rather the electrons therein) is free to rotate such that this condition is satisfied. Coupled magnetic ions therefore result in antiferromagnetic alignment.

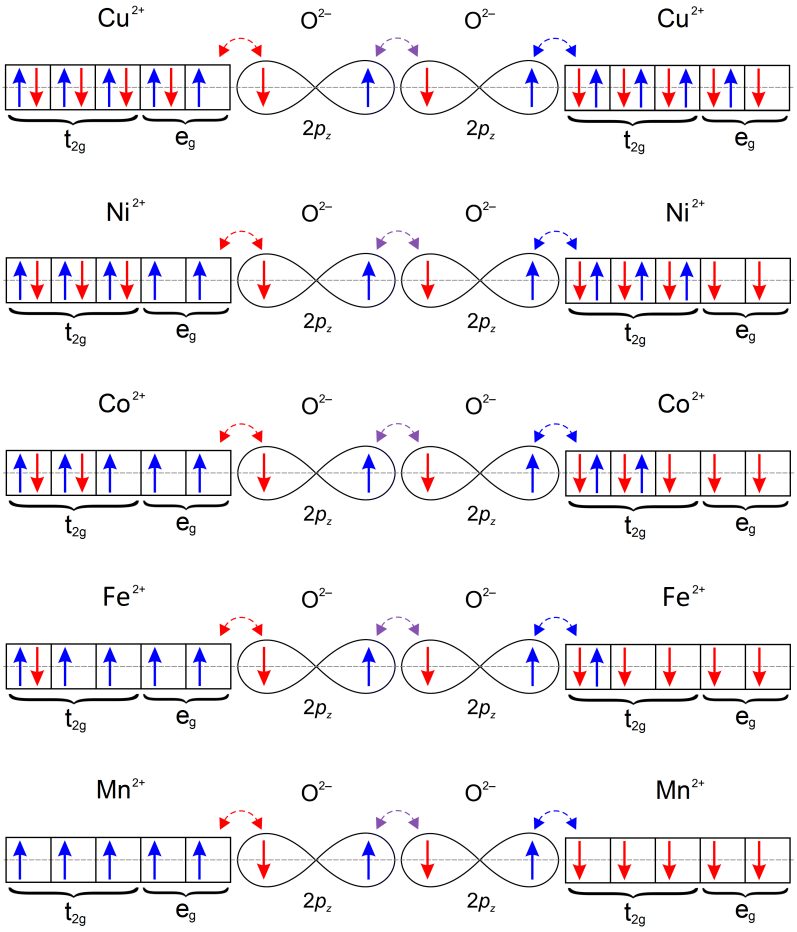

Figure 1.4: Super-superexchange of M-O-O-M pathways showing the antiferromagnetic alignment of transition-metal ions of various spins.

1.3 Proposed Magnetic Structures

Band structure calculations for $CuSb_2O_6$ reveal an unusual quasi 1-d magnetic ground state driven by orbital ordering, which is attributed to the presence of competing interactions between in- and out-of-plaquette[1] orbitals and strong electron correlations [7]. The calculations suggest that the dominant magnetic exchange is

[1]The plaquette is the square arrangement of oxygen ions that surrounds the transition metal ion. It is oriented perpendicular to the M-O-O-M chains.

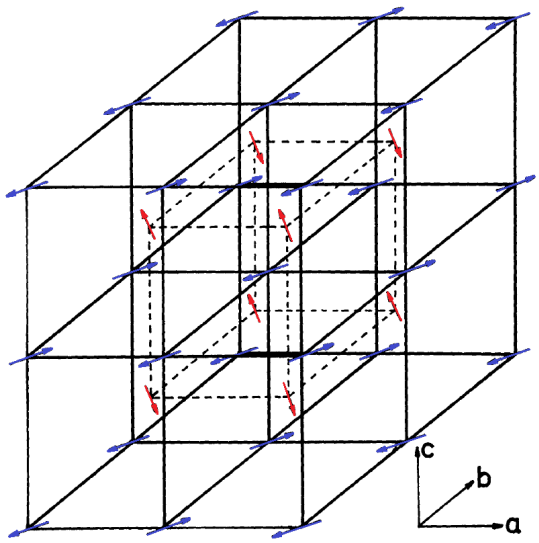

Figure 1.5: The two-sublattice model. All magnetic moments are constrained to the *a*-*b* plane. Moments of one sublattice (indicated by solid lines) are aligned parallel to [110] while moments of the other sublattice (indicated by dashed lines) are aligned parallel to $[1\bar{1}0]$.

along the [110] crystallographic direction at z = 0 and the $[1\bar{1}0]$ direction at $z = 1/2$. This exchange is directed along the apexes of the Cu-O_6 octahedra (i.e., via the out-of-plaquette oxygen ions) producing Cu-O-O-Cu linkages within the crystal structure. The directional aspect of the magnetic exchange suggests a *two-sublattice model* for the antiferromagnetic structure (see Fig. 1.5). One sublattice, at $z = 0$, has antiparallel magnetic moments along [110] with the moments lying purely in the *a*-*b* plane (i.e., no canting along [001]); the second magnetic sublattice, at $z = 1/2$, has its moments also lying purely in the *a*-*b* plane, but rotated 90° with regard to the first layer. Band structure calculations [7] suggest $J/J_{\perp} \sim 120$ for $CuSb_2O_6$.

There is disagreement, however, regarding the magnetically ordered state in $CuSb_2O_6$ determined from experiment. Nakua and Greedan [25] proposed two possible magnetic structures, based on powder neutron diffraction data. One of these,

the *orthogonal model*, has Cu magnetic moments ordered antiparallel along [110] at $z = 0$ and $[1\bar{1}0]$ at $z = 1/2$; it is identical to the two-sublattice model described above. Later, single-crystal neutron diffraction by Kato *et al.* [8] determined that the magnetic structure involved parallel alignment (i.e., ferromagnetic) of the magnetic moments along [010] and antiparallel alignment along [100], thus forming an antiferromagnetic structure with magnetic wave vector $(\pi/a,0,\pi/c)$. Subsequent single-crystal measurements by Gibson *et al.* [26] suggested ordering similar to the two-sublattice model, albeit with a slight tilting of the moments. The work by Kato *et al.* is the most detailed investigation/analysis, and their magnetic structure model agrees best with the anisotropy of the magnetic susceptibility χ [9]. More recent neutron diffraction experiments [27] also agree with Kato *et al.* This model, however, disagrees with the magnetic structure suggested by the magnetic exchange constants obtained from band structure calculations [7].

In the case of $NiTa_2O_6$, density functional theory (DFT) calculations performed by Law *et al.* [14] reveal $J/J_\perp \sim 65$ and that the dominant antiferromagnetic exchange path is along [110] at $z = 0$ and $[1\bar{1}0]$ at $z = 1/2$, which would result in the same two-sublattice model (or orthogonal model) for the antiferromagnetic structure as described above. In the same work, however, results from powder neutron diffraction (PND) suggested the antiferromagnetic structure previously reported by Ehrenberg *et al.* [28], also based on PND data. In this model, the Ni magnetic moments are ordered antiparallel along [110] at both $z = 0$ and $z = 1/2$, i.e. without the 90° rotation described above. This discrepancy was not addressed in Law's report. However, the DFT calculations and the absence of Ni-O-O-Ni bonds along [110] at $z = 1/2$ provide support for the two-sublattice model. Neutron diffraction on single crystals will likely be required to identify the antiferromagnetic structure with better certainty, given the presence of disorder below T_N in the PND data [28].

The magnetically-ordered state of $CoSb_2O_6$ also displays superexchange pathways along [110] (i.e., along Co-O-O-Co linkages), with a magnetic structure [29] that is described as similar to that of $FeTa_2O_6$. However, two magnetic structures were proposed [30] for $FeTa_2O_6$ using Mössbauer spectroscopy and powder neutron diffraction. Both models contain moments constrained to the *a*-*b* plane. The moments in Model I point along [110] and are arranged antiparallel along [100] and [001] but are parallel along [010]. Model II is more complex and contains a second sublattice that is rotated 90° to the first. This model is essentially the two-sublattice model described above. Models I and II cannot be distinguished if only powder neutron data is available. The Mössbauer spectrum was therefore used to eliminate Model I as a possible candidate. It was therefore concluded that Model II was the correct magnetic structure for $CoSb_2O_6$. The magnetic structure of $FeTa_2O_6$ was revisited, however, by Takano and Takada [12] who also performed Mössbauer measurements. They concluded the structure contains magnetic moments which are canted by 20° in the [001] direction. Thus the exact magnetic structure of $FeTa_2O_6$ remains ambiguous.

The proposed structure for $CoTa_2O_6$ is perhaps the most complex. Reimers *et al.* performed powder neutron diffraction with a Rietveld refinement [29]. They interpreted their results to be consistent with a rather elaborate structure with a $(4a, 4a, 4c)$ magnetic unit cell. They analyzed the structure in terms of a helical spin arrangement and indexed the magnetic reflections with a helix propagation vector $k_0 = (\frac{1}{4}, \frac{1}{4}, \frac{1}{4})$. They found that the data could be successfully fit using a model in which the two sublattices have different cone axes about which the spins rotate. The resulting structure contains moments constrained to the *a*-*b* plane at $z = 0$ and half of the moments at $z = 1/2$ oriented mostly along [001] while the other half are in the *a*-*b* plane (see Fig. 1.6a). Contrarily, Kinast *et al.* performed a series of measurements, also on polycrystalline samples, and concluded the magnetic

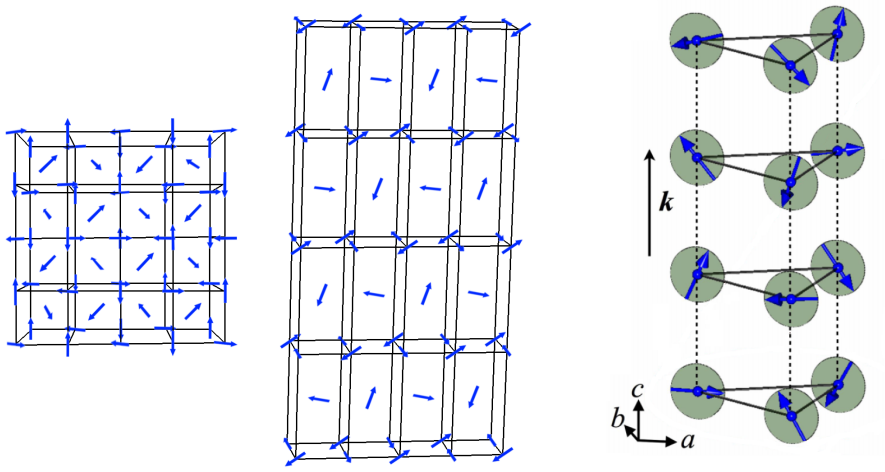

(a) $CoTa_2O_6$ (b) $MnSb_2O_6$

Figure 1.6: (a) The magnetic structure viewed along [001] (left) and [010] (right) for $CoTa_2O_6$ determined by Reimers *et al.* [29] (b) The magnetic structure of $MnSb_2O_6$ proposed by Johnson [33]. A cycloid propagates parallel to the *c*-axis with the moments constrained to the *a*-*c* plane.

structure to be consistent with the two-sublattice model described above [31, 32]. The work done for this dissertation will hopefully resolve the issues surrounding the determination of the magnetic structure of CoTa2O6, as well as FeTa2O6.

Turning now to $MnSb_2O_6$, which has a trigonal crystal structure, we can anticipate the ordered moments to be frustrated in the *a*-*b* plane. That is the say, if the moments are, for example, constrained to the *a*-*b* plane and two adjacent moments located at different vertexes of a triangle are antiferromagnetically aligned, then there is no possible orientation in which a moment at the third vertex can be antiferromagnetically aligned with the other two moments. The energetic solution to this frustration is for the moments to have projections along the *c*-axis. Reimers *et al.* [34] used neutron powder diffraction and magnetic susceptibility measurements to determine the magnetic structure below T_N. They observed incommensurate long-range antiferromagnetic order manifest as co-rotating cycloids with the rotation axis

in the a-b plane, i.e. the spins can have components *out* of the plane. Later, Johnson *et al.* [33] also determined the magnetic structure to be composed of co-rotating cycloids. In that report, the moments are said to be constrained to the a-c plane with the cycloid propagating parallel to the c-axis. The structure is depicted in Fig. 1.6b. Furthermore, they used band structure calculations of exchange energies for various directions and determined that the magnetic ground state for $MnSb_2O_6$ orders with a vector constrained to the Δ line of symmetry, namely the c-axis. In a more recent report, Kinoshita *et al.* [35] have suggested that the plane of rotation is tilted away from the c-axis by $13^\circ - 18^\circ$.

2. SAMPLE GROWTH AND CHARACTERIZATION

2.1 Crystal Growth

When searching for materials with chemical formula $M(\mathrm{Sb,Ta})_2\mathrm{O}_6$ for the current study, we find limited options. Charge neutrality requires the transition metal to be in a (2+) valence state. Furthermore, according to Westin [36], the ionic radius must be ≤ 0.78 Å (similar to the antimony and tantalum ionic radii $r_{Sb^{5+}} = 0.6$ Å and $r_{Ta^{5+}} = 0.7$ Å). The current investigation therefore covers M = Mn, Fe, Co, Ni, and Cu. Analogous non-magnetic compounds are synthesized using Zn and Mg.

Considerable effort to grow $\mathrm{FeSb_2O_6}$ was made in 1975 by Donaldson *et al.* [37] following the "original recipe" of Byström [38]. However, no success came of Donaldson's attempts and the group managed to synthesize only $\mathrm{FeSbO_4}$. A 2003 report by Berlepsch [39] revisited the $M\mathrm{SbO_4}$ and $M\mathrm{Sb_2O_6}$ compounds and the results shown in their report led to the presumption that a $\mathrm{FeSb_2O_6}$ compound with both $\mathrm{Fe^{2+}}$ and $\mathrm{Sb^{5+}}$ does not exist because it is more energetically favorable for the iron cation to adopt a higher oxidation state. Later, in 2006, Huang [40] reported that the existence of $\mathrm{Sb^{5+}}$ and $\mathrm{Fe^{2+}}$ in one compound is not possible, and that reports which claim to have grown $\mathrm{FeSb_2O_6}$ are actually $\mathrm{Fe(III)Sb(V)_{\frac{3}{2}}Sb(III)_{\frac{1}{2}}O_6}$ of the form $(\mathrm{FeSbO_4})(\mathrm{Sb_2O_4})_{\frac{1}{2}}$.

The difficulty encountered when attempting to synthesize $\mathrm{FeSb_2O_6}$ is not surprising when the electron configurations of iron and antimony are considered. Iron has an electron configuration of $[\mathrm{Ar}]3d^6 4s^2$, and thus has a tendency to give up the outer 2 electrons for a (2+) valency, or an additional third electron from the d orbital to make it half full, as preferred by Hund's rules. Antimony, with electron configuration $[\mathrm{Kr}]5s^2 4d^{10} 5p^3$, has a tendency to reach a valency of either (5+) or (3+), determined

by whether it releases all 5th-shell electrons, or just the 3 outer p-orbital electrons, keeping the $5s$-orbital filled. Consequently, the configuration resulting in Fe^{3+} and Sb^{3+} is the more energetically favorable oxidation state. Alternatively, tantalum has the electron configuration $[Xe]4f^{14}5d^{3}6s^{2}$ and therefore prefers the oxidation state Ta^{5+}, which would leave a filled valence shell. Thus the difficulties associated with synthesizing $FeSb_2O_6$ are not present for $FeTa_2O_6$.

2.1.1 Synthesis of Polycrystalline Samples

The $M(Sb,Ta)_2O_6$ samples were prepared by mixing stoichiometric amounts of the reagents shown in Table 2.1. A slight excess (about 5 percent) of Sb_2O_3 was used in the case of $CoSb_2O_6$ to prevent $Co_7Sb_2O_{15}$ from forming, as per the recommendation of Reimers *et al* [29]. The powders were pressed into pellets and sintered in an alumina crucible in air under the conditions provided in the table. (One exception is the case of $FeTa_2O_6$. The reagents for this compound have an excess of oxygen atoms, meaning the balanced reaction equation will result in $4FeTa_2O_6 + O_2$. To prevent the O_2 from recombining with Fe_2O_3, the compound was sintered in an atmosphere of hydrogen and argon at a ratio of 3:97. The excess oxygen therefore binds to the hydrogen forming H_2O.) After sintering, the pellets were cooled to room temperature at 2 °C/min and then re-ground and re-sintered 2-3 times (see Table 2.1) to obtain a pure phase, which was confirmed using X-ray Powder Diffraction.

2.1.2 X-ray Powder Diffraction

The powder samples were analyzed using X-ray Powder Diffraction (XRD). In this analysis, monochromatic CuKα x-rays (1.540562 Å) undergo Bragg diffraction by interacting with the various crystallographic planes of a sample. Powders, rather than

Table 2.1: $M(Sb,Ta)_2O_6$ Compound Synthesis Parameters. *The first firing of $ZnSb_2O_6$ was held at 600 °C. †Sintering was held in H:Ar atmosphere at a 3:97 ratio.

Compound	Reagents	Max Temp	Duration	No. of sinterings
$MgTa_2O_6$	$MgO + Ta_2O_5$	1000 °C	10 hours	3
$ZnSb_2O_6$	$ZnO + Sb_2O_3$	800 °C *	12 hours	2
$CuSb_2O_6$	$CuO + Sb_2O_3$	1000 °C	72 hours	2
$NiSb_2O_6$	$NiO + Sb_2O_3$	1100 °C	10 hours	2
$NiTa_2O_6$	$NiO + Ta_2O_5$	1200 °C	23 hours	3
$CoSb_2O_6$	$2Co_3O_4 + 6Sb_2O_3$	1050 °C	72 hours	2
$CoTa_2O_6$	$CoCO_3 + Ta_2O_5$	1050 °C	12 hours	2
$FeTa_2O_6$	$2Fe_2O_3 + 4Ta_2O_5$	1100 °C †	24 hours	3
$MnSb_2O_6$	$MnCO_3 + Sb_2O_3$	1100 °C	10 hours	3

single-crystals, are analyzed to ensure that all crystallographic directions are sampled by the beam. When the Bragg condition, $2d\sin\theta = n\lambda$, for constructive interference is satisfied, a peak in the measured x-ray intensity is obtained for that particular angle. The spectrum produced by this technique is unique for each compound. It can therefore be compared against known spectra to determine if a prepared sample matches the intended phase. XRD results for the antimonates are compared against previously verified spectra in Fig. 2.1. The results for the tantalate compounds are compared in Fig. 2.2. All samples show excellent agreement with the verified spectra reported from the International Centre for Diffraction Data (ICDD).

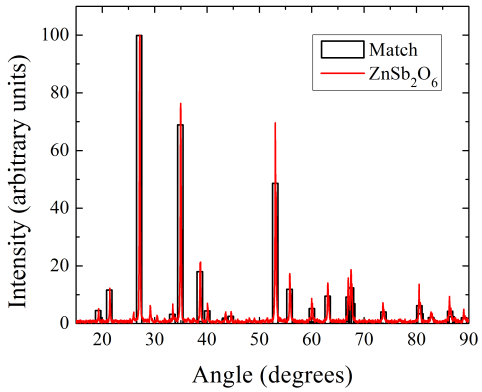

(a) $ZnSb_2O_6$

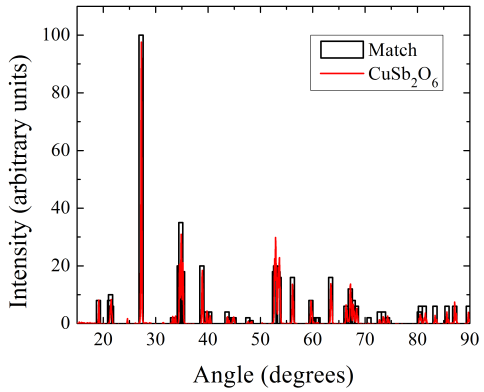

(b) $CuSb_2O_6$

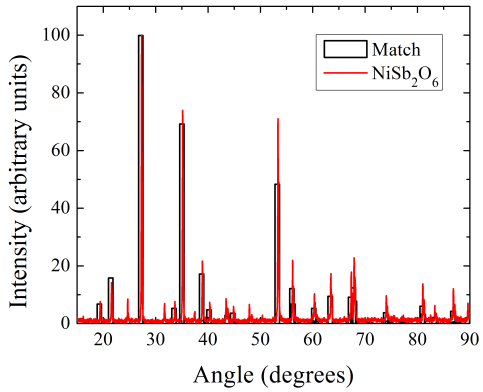

(c) $NiSb_2O_6$

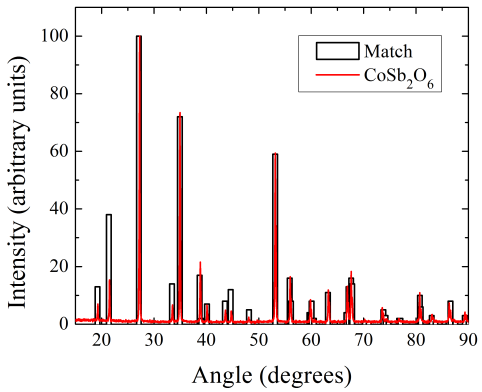

(d) $CoSb_2O_6$

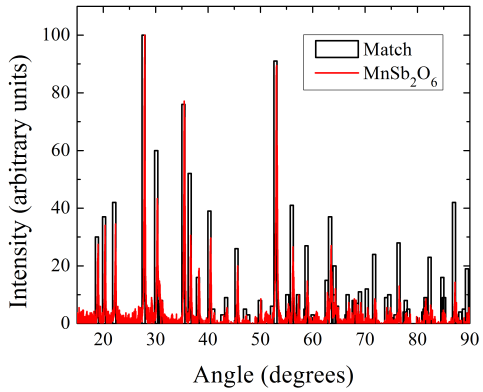

(e) $MnSb_2O_6$

Figure 2.1: X-ray Powder Diffraction Spectra for the Antimonates. Experimental data (red curves) have been normalized such that the tallest measured peak matches the intensity of the tallest peak from the verified spectra (hollow bars).

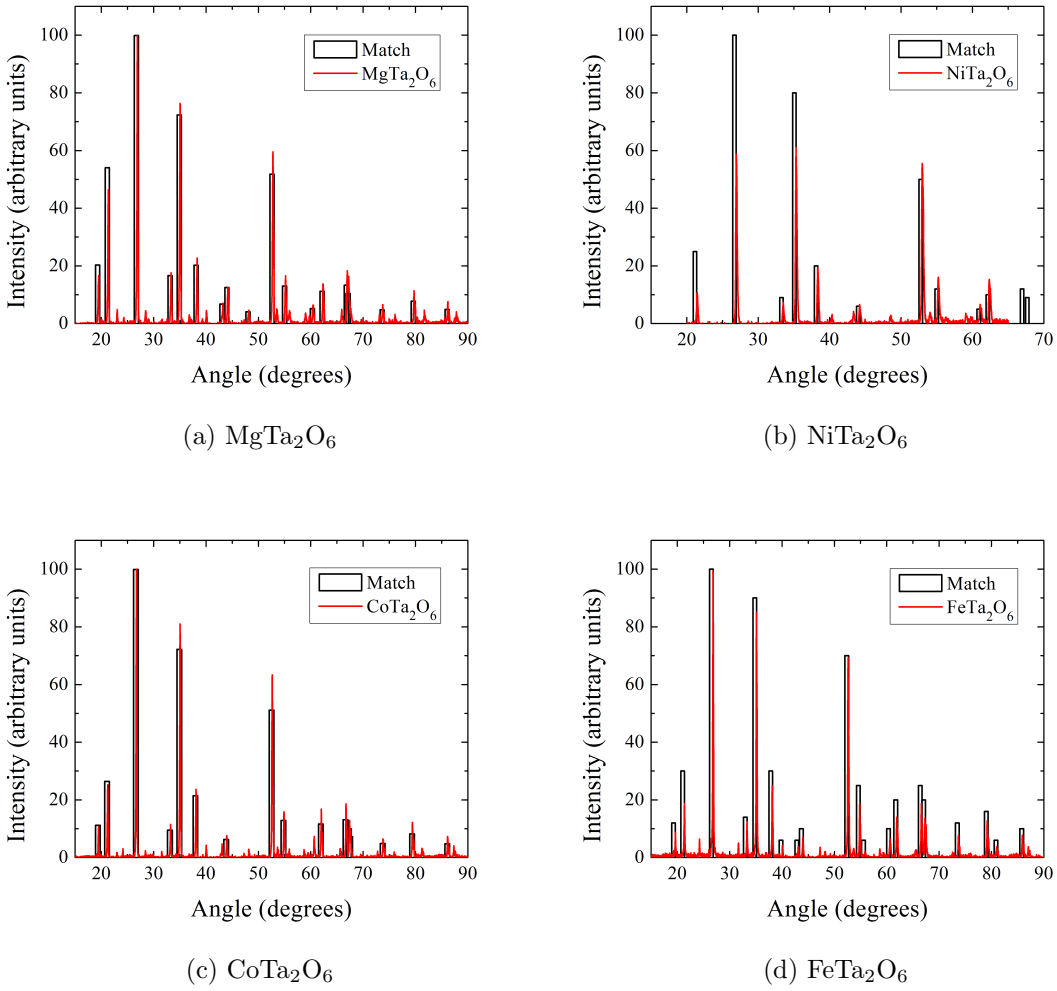

(a) $MgTa_2O_6$ (b) $NiTa_2O_6$

(c) $CoTa_2O_6$ (d) $FeTa_2O_6$

Figure 2.2: X-ray Powder Diffraction Spectra for the Tantalates. Experimental data (red curves) have been normalized such that the tallest measured peak matches the intensity of the tallest peak from the verified spectra (hollow bars).

2.1.3 Single-crystal Growth

MSb_2O_6 single crystals were grown using chemical vapor deposition (CVD). A small amount of powder, typically a gram, was transferred to a 1 cm $\times$ 15 cm quartz tube along with 100 mg of $TeCl_4$, which provides the chlorine gas that serves as the transport agent [41]. The tube was evacuated to 1.3 $\times$ 10^{-3} mbar before being sealed. The sealed ampoule was then placed in a tube furnace and heated at 220 °C

Table 2.2: Maximum Growth Temperatures for $M\mathrm{Sb_2O_6}$.

Compound	$\mathrm{ZnSb_2O_6}$	$\mathrm{CuSb_2O_6}$	$\mathrm{NiSb_2O_6}$	$\mathrm{CoSb_2O_6}$	$\mathrm{MnSb_2O_6}$
Temperature [°C]	800	920	900	930	900

for one hour, then brought to 380 °C at a rate of 50 °C per hour. It was held at this temperature for another hour before being raised to the maximum growth temperature (see Table 2.2) over the course of 3 hours. The ampoule remained at this temperature for 200 hours before cooling at a constant rate to room temperature over the course of 15 hours.

The thermal gradient (~ 4.5°C/cm) over the quartz ampoule allows the chlorine gas to transport the powder located at the high temperature region of the ampoule to the opposite (cooler) region, where it is deposited on the inner quartz surface as single crystals. A depiction of the thermal gradient is shown in Fig. 2.3. Samples were typically 3 to 5 mg, and often grew as bicrystals. Boundaries between the conjoined crystals were identified during the orienting process, which employed Laue x-ray diffraction. The unwanted crystals were removed via a delicate sanding process, which ultimately left the sample as a single crystal with six flat sides orthogonal to the adjacent faces.

The tantalate compounds were grown using the floating-zone method. This technique employs an image furnace consisting of two halogen lamps each located at a focus of an elliptical hemispheric mirror. The second focus of each mirror is located at a region called the hot (or *molten*) zone. All light emitted from either lamp therefore passes through this region. The high energy density allows the temperature of a sample placed at this location to increase drastically (see Fig. 2.4). For the compounds studied herein, we have employed a NEC Machinery Corporation model SC1-MDH optical image furnace with two 1500-watt lamps. A polycrystalline *feed* rod and a

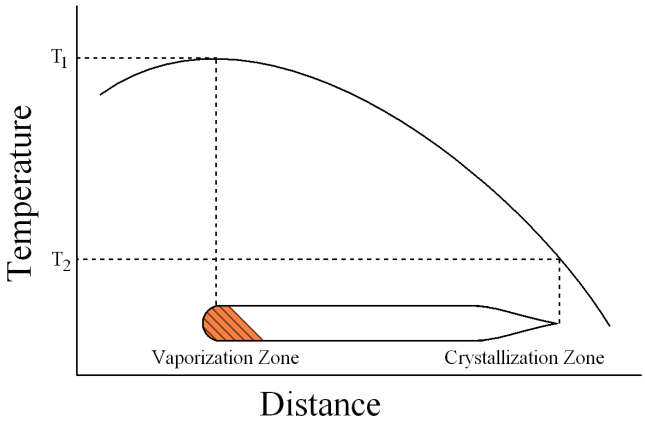

Figure 2.3: Depiction of the thermal gradient for chemical vapor deposition.

seed rod of the same material are vertically oriented collinear with the mutual focus of the two ellipsoid mirrors located where the two rods meet. The power of the lamps is then steadily increase while the rods counter rotate each at 30 rpm, ensuring uniform heating. When the temperature of the hot zone is sufficient to melt the ends of the two rods, they are brought together ("connected") and then slowly lowered through the hot zone. As the system moves through the hot zone, the bottom of the molten region cools and solidifies. The slow cooling allows for the formation of single crystals to occur. The molten material that leaves the hot zone is replaced by new material from the feed rod above.

To form the rods, small cylindrical balloons were filled with the powdered samples and hydrostatically pressed at 40 MPa. After extracting from the balloons, the resulting rods (3 mm in diameter and up to 60 mm in length) were hardened by sintering at 1000-1200 °C for 10 hours. Single crystals of $NiTa_2O_6$, $CoTa_2O_6$, and $FeTa_2O_6$ were grown[1] with the halogen lamps operating at 570 W, 460 W, and 423 W, respectively. All rotations rates were set to 30 rev/min (meaning a relative

[1]The samples of $NiTa_2O_6$ and $CoTa_2O_6$ used in this research were grown by Aaron Schye.

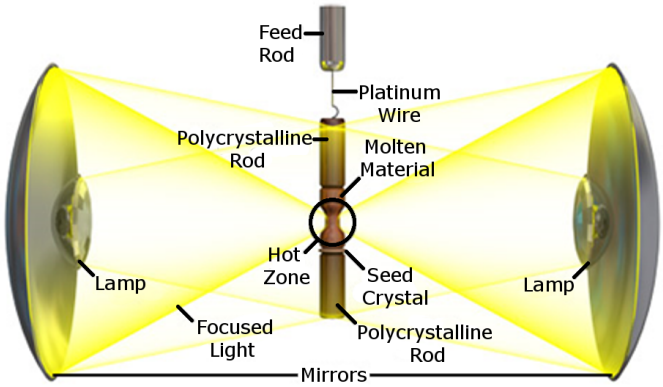

Figure 2.4: Schematic of the optical image furnace showing the elliptical cavities that focus the light from two 1500 W halogen lamps onto a hot zone where crystal growth occurs.

rotation of 60 rev/min). $NiTa_2O_6$ rods, in an oxygen atmosphere, and $CoTa_2O_6$ rods, in argon, were passed through the hot zone at 5 mm/h. Rods of $FeTa_2O_6$ were placed in an argon atmosphere and lowered through the hot zone at 1.0-1.8 mm/h. Growth rates for $FeTa_2O_6$ that are faster than 2 mm/h can result in cracked or otherwise compromised samples [42].

2.2 Laue Diffraction and Crystal Orientation

Orientation of the single crystals was performed with Laue diffraction in which x-rays with energies typically around 30-35 keV diffract and back-scatter onto Polaroid film, creating a pattern as exemplified in Fig. 2.5. In this type of diffraction, diffracted beams from individual *planes of a zone* (planes which are parallel to a single line, called the *zone axis*) all lie on the surface of an imaginary cone whose axis is the zone axis [43]. When the cone is intersected by the film, the diffraction spots appear along hyperbolas. Primary axes will occur at the intersection of many of these hyperbolas, which will appear as a spot typically brighter than others surrounding it. The pattern

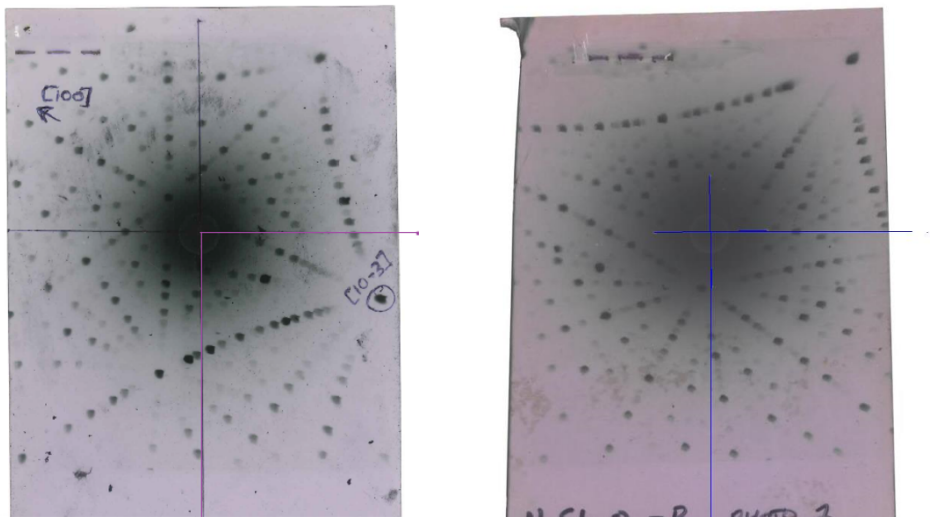

(a) Typical Laue pattern showing an intermediate axis of $NiSb_2O_6$

(b) Laue pattern centered near [001] of $NiSb_2O_6$

Figure 2.5: Polaroid photos showing some x-ray diffraction patterns. Typical exposure times are 12 to 15 minutes.

can be compared against a theoretical calculation using software such as QLaue [44], after inputting the necessary crystallographic parameters provided in the Appendix.

The orientation of the crystal may be changed using a goniometer. In the early days of crystallography, the magnitude of this change could be determined using Greninger charts, which allowed angular relations between zones and planes in a crystal to be directly read from an x-ray diffraction photograph. However, a new chart had to be produced if the distance between the sample and x-ray film was changed. More versatility, and perhaps better accuracy, can result from using instead the Greninger formulas (Eqs. 2.1 - 2.4), in conjunction with software such as Microsoft Excel, after the target spot's coordinates are measured from the film.

$$\mu = \sqrt{1 + \left(\frac{x'}{d}\right)^2 + \left(\frac{y'}{d}\right)^2} \tag{2.1}$$

$$a = \frac{1+\mu}{2}, \quad b = \frac{x'}{2d}, \quad c = \frac{y'}{2d} \tag{2.2}$$

$$\alpha = \frac{180^\circ}{\pi} \tan^{-1}\left(\frac{b}{a}\right) \tag{2.3}$$

$$\beta = \frac{180^\circ}{\pi} \tan^{-1}\left(\frac{c}{\sqrt{a^2+b^2}}\right) \tag{2.4}$$

In the above equations, x' and y' correspond to the distance of the target spot away from the point where the incident x-ray beam passes through the film. The value of d is taken to be the distance of the sample to the Polaroid, typically 39 to 41 mm. The quantities, α and β are the angles one must rotate the goniometer, horizontally and vertically, in order to center the target point, and therefore orient the desired crystal plane parallel with the film. If the crystal is oriented along a primary axis, the brightest straight lines which emanate from the central point will typically point to the other axes. These lines will always be perpendicular for cubic and tetragonal crystals. The next brightest set of lines between these will point in the direction of the corners of the unit cell. For a cubic crystal, these too will be perpendicular and point 45° between the "primary" lines. For a tetragonal crystal, however, these secondary lines will only be perpendicular and at 45° to the others when viewing along the c-axis. When viewing along the a- and b-axes, the bright secondary lines will neither be perpendicular, nor at 45° from the primary lines. Instead, their angle will be determined by the crystal parameters, such that $c = a \tan\theta$.

Laue diffraction can also be used to indicate crystal quality. Diffraction spots that are smeared might signify that the crystal has undergone a plastic deformation by

bending and/or twisting in which some portions of the crystal are disoriented from other portions. In some cases, this may be by as much as tens of degrees. If the diffraction spots are twinned, such that the photo has a "double-vision" appearance, this would suggest that the crystal itself is twinned, i.e. similar co-spacial lattices exist slightly offset from one another. Twinning is very difficult to avoid and in many instances impossible to remove. In the current investigation, a small amount of twinning was observed in some samples. However, the orientations of the twinned axes usually differed by less than a degree. Only samples with little or no observable twinning were chosen for study.

3. THEORY

In a chain of atoms, the magnetic interactions can lead to a variety of ground states which can be characterized by the sign and magnitude of the interaction. The spin-dependent part of the interaction of localized electrons at lattice sites i and j with spins $\mathbf{S_i}$ and $\mathbf{S_j}$ can be described [45] by a Hamiltonian of the form

$$\mathscr{H} = -2 \sum_{<ij>} J_{ij} \mathbf{S_i} \cdot \mathbf{S_j}, \tag{3.1}$$

where J is the coupling between electrons. Qualitatively, J describes the overlap of two electron orbitals of adjacent atoms. If two electrons reside in mathematically orthogonal orbitals ψ_i and ψ_j, then the exchange integral J_{ij} is given by [46]

$$J_{ij} = \int \psi_i^*(i)\psi_j^*(j)\frac{e^2}{r_{ij}}\psi_i(i)\psi_j(j)\mathrm{d}\tau. \tag{3.2}$$

The magnitude of the integral governs the strength of the exchange interaction. The value decreases very rapidly with distance; therefore the summation is usually restricted to nearest neighbors. The sign determines the relative orientation of the spins. A negative value of J_{ij} would cancel the negative sign of $\mathscr{H}$. To minimize the Hamiltonian, the two spins must be anti-aligned so that $\cos(\theta)$ associated with the dot product is (-1). Likewise, if J_{ij} is positive, parallel alignment leading to $\cos(\theta) = 1$ would keep the Hamiltonian negative and minimized. Some texts do not introduce a negative sign in the Hamiltonian, and therefore the signs of J associated with ferro- or antiferromagnetic alignment are opposite to that of the current case. The Hamiltonian above provides a firm foundation from which many thermodynamic and magnetic properties of a crystal can be derived. In practice, however, systems are often too complex to be solved exactly, and so approximation methods have been implemented. Equation (3.1) can be expanded in terms of couplings pertaining to

intralayer (in-plane) or interlayer (out-of-plane) interactions:

$$\mathscr{H} = -2 \sum_{<ij>} J_{xy}(S_{ix}S_{jx} + S_{iy}S_{jy}) + J_z S_{iz} S_{jz}. \tag{3.3}$$

It is beneficial to introduce two important parameters, d and D, which are the lattice and spin dimensionality, respectively. Imposing certain constraints on J_{ij} allows us to adopt different universality classes associated with particular values of d and D. The spin dimensionality reflects which spin components are coupled together and therefore relates to the anisotropy of the spin exchange. For example, when $J_{xy} = 0$, the spins are only able to take on spin-up or spin-down values, i.e. the spin dimensionality is $D = 1$ and $g_\perp$ is expected to be close to zero [14]. This describes the Ising model mentioned in the Introduction. When $J_z = 0$, the spins are constrained to the XY plane with spin dimensionality $D = 2$ and the aptly named XY model is obtained. Considerable anisotropy in the g-values, with $g_\perp >> g_\parallel$, is a prerequisite for the applicability of the XY model [47]. When $J_{xy} = J_z$, the interactions are isotropic and suggest that the magnetic ions reside in sites of high symmetry [47]. The spin dimensionality is then $D = 3$ and the Heisenberg model is established.

The arrangement of the magnetic ions within the lattice determines the value of the lattice dimensionality. The value of d is taken to be 1, 2, or 3 for ions arranged in chains, planes, or a 3-d network, respectively. The values of d and D are independent from one another, but only certain combinations result in phase transitions at finite temperatures. It has been shown [48] that transitions to long-range order cannot occur in $d = 1$ systems. Let us consider the change in free energy $\Delta F = \Delta U - T\Delta S$ from elementary thermodynamics. First assume that all spins are ferromagnetically aligned. If a break is introduced such that a domain wall exists between two ferromagnetic regions which are anti-aligned (i.e. all spin-up on one side and all spin-down on the other), the difference in internal energy is $\Delta U = 2J$. The change in

entropy ΔS depends upon the number of locations ($\Omega = N - 1$) along the chain where a domain wall can be placed, and is written $\Delta S = k_B \ln(N-1)$. Therefore $\Delta F = 2J - Tk_B \ln(N-1)$ which, for sufficiently large values of N, is negative for all temperatures. Because the free energy is lowered by domain wall excitations, long-range order cannot occur. A similar argument can be made for the antiferromagnetic case.

For the 2-d Ising lattice, domain walls can meander around a plane, separating large regions of spin-up and spin-down orientations. The energy associated with the domain wall is $\Delta U = 2LJ$ where L is the number of ions along its length. Here, the number of states is $\Omega = 2^L$ and therefore $\Delta F = 2LJ - Tk_B L \ln(2)$. It follows that $\Delta F > 0$ for $T < \frac{2J}{k_B \ln(2)} = T_c$, i.e. the system is stable against the creation of domain walls below $T_c = 2.885 J/k_B$. The 2-d Ising lattice is the only 2-d system capable of a phase transition. This is shown more rigorously by Onsager [49]. Likewise, the Mermin-Wagner theorem [50] predicts that no long-range order occurs for $T > 0$ in a 2-d Heisenberg antiferromagnet. The lowest lattice dimensionality capable of a phase transition for the XY and Heisenberg models is $d = 3$. However, phonon coupling between the magnetic moments and the lattice can assist in phase transitions in models with reduced dimensionality [16, 51]. In this sense, such compounds are thus referred to as *quasi* one- or two-dimensional.

Given the quantum mechanical complexities, exact solutions for the thermodynamic properties are difficult to obtain, especially when spin degrees of freedom are considered. Many physicists have resorted to various approximations in order to describe the system, often with satisfactory results. Some useful models of magnetic susceptibility are discussed in the following section.

3.1 Theoretical Models of Magnetic Susceptibility

The magnetic properties of any material originate from the magnetic moments of the individual atoms. The moment of a free atom manifests from three sources: the spin of the atom's electrons, their orbital momentum, and the change in the orbital momentum induced by an applied field [52]. The first two sources provide a paramagnetic contribution to the magnetization, while the third provides a diamagnetic contribution. The magnetization, M, is a vector field that expresses the (volume or molar) density of the magnetic moments. If the moments align with an external field and relax into disorder when it is removed, then the material is paramagnetic. In a paramagnet, magnetization is a linear function of the applied field when $\mu B/k_B T << 1$. Alternatively, if the moments align in the direction opposite to that of the applied field, then the material is diamagnetic. When the direction of the moments are opposite to those of their neighbors, the material is antiferromagnetic.

The behavior of the magnetic susceptibility, $\chi = \partial M/\partial H$, can reveal information about the coupling between ions and the different energy levels involved in the system. However, the transition metals studied in this dissertation contain various spin values which display different degrees of freedom. Therefore each value of S requires a different theoretical model to describe the measured susceptibility. Models necessary to the following investigation are discussed below.

3.1.1 $S = 1/2$ Heisenberg Chain

The magnetic interaction with $S = 1/2$ is the simplest, and therefore the most understood, spin system. Much of the work has been pioneered by Bonner and Fisher [53] who calculated various thermodynamic properties of the 1-d chain containing up

to 11 individual spins. Their theory relied on Monte Carlo calculations on finite models to obtain limiting ratios involving specific heat maxima, magnetic susceptibility maxima, and the temperatures where those maxima occur. From their results, one can obtain Heisenberg exchange couplings using the ratios

$$\chi_{max}|J|/Ng^2\mu_B^2 \approx 0.07346, \tag{3.4}$$

$$k_B T_{max}/|J| \approx 1.282, \tag{3.5}$$

$$\chi_0|J|/Ng^2\mu_B^2 = 0.050661 \approx 1/2\pi^2, \tag{3.6}$$

where N is the number of magnetic ions, g is the Landé g-factor, and χ_0 is the magnetic susceptibility at zero temperature. More recently, these ratios were determined more explicitly by Eggert, Afflect, and Takahashi [54] and refined by Klümper and Johnston [55, 56] using 6th order polynomials, along with the substitution $|J| \rightarrow |J|/2$ in order to describe a uniform chain rather than a chain of non-interacting dimers. The ratios in Eqs. 3.4 - 3.6 then equate to 0.146 926 279(1), 0.640 851 0(4), and $1/\pi^2$, respectively.

Using the Bonner-Fisher model [53, 57, 58], the intrachain susceptibility for a 1-d Heisenberg AFM $S = 1/2$ system can be fit using the equation

$$\chi_{intra} = \frac{Ng^2\mu_B^2}{k_B T} \frac{0.25 + 0.14995x + 0.30094x^2}{1 + 1.9862x + 0.68854x^2 + 6.0626x^3}, \tag{3.7}$$

where

$$x = \frac{|J_{intra}|}{2k_B T}. \tag{3.8}$$

According to the mean-field approximation [59, 60], the interchain susceptibility saturates at low temperature to the constant value

$$\chi_{inter} = -\frac{Ng^2\mu_B^2}{2J_{inter}}. \tag{3.9}$$

Some authors will ignore the factor of 2 multiplying the exchange constant in the denominator, absorbing it into the definition of J.

3.1.2 $S = 1$ Heisenberg Chain

Magnetic systems with integer spins are said to display a spin gap in the excitation spectrum between the spin-singlet and spin-triplet ground states, whereas half-integer spins are said to be gapless. This is known as Haldane's conjecture [61] and has been both experimentally and theoretically demonstrated [62, 63]. Souletie *et al.* [64] have derived a phenomenological expression for the magnetic susceptibility of an antiferromagnetic $S = 1$ Heisenberg chain with periodic boundary conditions (i.e. a *ring*) to minimize finite size effects. Additionally, the ring consists of an even number of spins (up to $n = 20$) to avoid frustration effects. They determined susceptibility using the density-matrix renormalization group technique [65]. Their result

$$\chi = \frac{Ng^2\mu_B^2}{k_BT}(0.125e^{-0.451J/k_BT} + 0.564e^{-1.793J/k_BT}) \tag{3.10}$$

has been applied to the magnetic behavior of Y_2BaNiO_5 and $Ni(C_2H_8N_2)_2NO_2ClO_4$, which are claimed to be the archetype [63] of the Haldane gap systems, with remarkable correspondence, suggesting the validity of the expression.

Below the transition temperature, the magnitude of the Haldane gap, Δ, can be inferred from the magnetic susceptibility through the expression [66]

$$\chi = \chi_0 + Ce^{-\Delta/k_BT}. \tag{3.11}$$

The χ_0 term is the temperature independent paramagnetism, often attributed to the Van Vleck susceptibility. Some authors [64, 67] include a $1/\sqrt{T}$ factor preceding the exponential which follows from field-theory mapping. This factor is related to the relativistic magnetic properties in the nanometric scale magnon dispersion [64, 68].

The value of the Haldane gap is estimated [69] as $\Delta \approx 0.41J$, where J is the exchange constant obtained through susceptibility fits such as Eqs. 3.10. This estimate of Δ has been confirmed and reiterated by a number of theoretical papers [62, 67, 70].

3.1.3 $S = 3/2$ Ising Chain

The Co^{2+} ion is regarded as the best example of an Ising ion [71]. To the best of my knowledge, there is no expression found in the literature for the magnetic susceptibility of a $S = 3/2$ ion that takes into account the spin degrees of freedom. Therefore, in anticipation of applying the Ising model to $Co(Sb,Ta)_2O_6$, we shall derive an expression for $S = 3/2$ by following the method outlined by Carlin [47]. Let us consider only the $\boldsymbol{S_z}$ operator whose eigenvalues for spin $\frac{3}{2}$ are $+\frac{3}{2}$, $+\frac{1}{2}$, $-\frac{1}{2}$, and $-\frac{3}{2}$. For a dimer, there will then be a total of 16 possible states. The Hamiltonian for a pair of spins is chosen as

$$\boldsymbol{H} = -2\mathrm{J}\boldsymbol{S}_{\mathrm{z}1}\boldsymbol{S}_{\mathrm{z}2} + \mathrm{g}\mu_{\mathrm{B}}\mathrm{H}_{\mathrm{z}}(\boldsymbol{S}_{\mathrm{z}1} + \boldsymbol{S}_{\mathrm{z}2}), \tag{3.12}$$

which has eigenvalues shown in Table 3.1.

Table 3.1: Eigenvalues for the $S = 3/2$ Ising model Hamiltonian.

Spin	3/2	1/2	−1/2	−3/2
3/2	$-\frac{9}{2}\mathrm{J} - 3\mathrm{g}\mu_{\mathrm{B}}\mathrm{H}_{\mathrm{z}}$	$-\frac{3}{2}\mathrm{J} - 2\mathrm{g}\mu_{\mathrm{B}}\mathrm{H}_{\mathrm{z}}$	$\frac{3}{2}J - \mathrm{g}\mu_{\mathrm{B}}\mathrm{H}_{\mathrm{z}}$	$\frac{9}{2}\mathrm{J}$
1/2	$-\frac{3}{2}\mathrm{J} - 2\mathrm{g}\mu_{\mathrm{B}}\mathrm{H}_{\mathrm{z}}$	$-\frac{1}{2}\mathrm{J} - \mathrm{g}\mu_{\mathrm{B}}\mathrm{H}_{\mathrm{z}}$	$\frac{1}{2}\mathrm{J}$	$\frac{3}{2}\mathrm{J} + \mathrm{g}\mu_{\mathrm{B}}\mathrm{H}_{\mathrm{z}}$
−1/2	$\frac{3}{2}J - \mathrm{g}\mu_{\mathrm{B}}\mathrm{H}_{\mathrm{z}}$	$\frac{1}{2}\mathrm{J}$	$-\frac{1}{2}\mathrm{J} + \mathrm{g}\mu_{\mathrm{B}}\mathrm{H}_{\mathrm{z}}$	$-\frac{3}{2}\mathrm{J} + 2\mathrm{g}\mu_{\mathrm{B}}\mathrm{H}_{\mathrm{z}}$
−3/2	$\frac{9}{2}\mathrm{J}$	$\frac{3}{2}\mathrm{J} + \mathrm{g}\mu_{\mathrm{B}}\mathrm{H}_{\mathrm{z}}$	$-\frac{3}{2}\mathrm{J} + 2\mathrm{g}\mu_{\mathrm{B}}\mathrm{H}_{\mathrm{z}}$	$-\frac{9}{2}\mathrm{J} + 3\mathrm{g}\mu_{\mathrm{B}}\mathrm{H}_{\mathrm{z}}$

These energies can then be used in the partition function, $\mathrm{Z} = \mathrm{e}^{-<\boldsymbol{H}>/k_BT}$, leading to the equation

$$\begin{aligned}\mathrm{Z} = {} & \mathrm{e}^{(\frac{9}{2}\mathrm{J}+3\mathrm{g}\mu_{\mathrm{B}}\mathrm{H}_{\mathrm{z}})/\mathrm{k_B}T} + \mathrm{e}^{(\frac{1}{2}\mathrm{J}+\mathrm{g}\mu_{\mathrm{B}}\mathrm{H}_{\mathrm{z}})/\mathrm{k_B}T} + \mathrm{e}^{(\frac{1}{2}\mathrm{J}-\mathrm{g}\mu_{\mathrm{B}}\mathrm{H}_{\mathrm{z}})/\mathrm{k_B}T} + \mathrm{e}^{(\frac{9}{2}\mathrm{J}-3\mathrm{g}\mu_{\mathrm{B}}\mathrm{H}_{\mathrm{z}})/\mathrm{k_B}T} \\ & + 2\mathrm{e}^{(\frac{3}{2}\mathrm{J}+2\mathrm{g}\mu_{\mathrm{B}}\mathrm{H}_{\mathrm{z}})/\mathrm{k_B}T} + 2\mathrm{e}^{(-\frac{3}{2}J+\mathrm{g}\mu_{\mathrm{B}}\mathrm{H}_{\mathrm{z}})/\mathrm{k_B}T} + 2\mathrm{e}^{(\frac{3}{2}\mathrm{J}-2\mathrm{g}\mu_{\mathrm{B}}\mathrm{H}_{\mathrm{z}})/\mathrm{k_B}T} \\ & + 2\mathrm{e}^{(-\frac{3}{2}\mathrm{J}-\mathrm{g}\mu_{\mathrm{B}}\mathrm{H}_{\mathrm{z}})/\mathrm{k_B}T} + 2\mathrm{e}^{-\frac{1}{2}\mathrm{J}/\mathrm{k_B}T} + 2\mathrm{e}^{-\frac{9}{2}\mathrm{J}/\mathrm{k_B}T}.\end{aligned} \tag{3.13}$$

The Helmholtz free energy can be determined through use of the partition function as $F = -k_B T \mathrm{lnZ}$. We can then use this expression to determine the molar magnetization, M_{mol}, defined as

$$M_{mol} \equiv -N_A \frac{\partial F}{\partial B} = \frac{N_A k_B T}{\mu_0} \left(\frac{\partial \mathrm{lnZ}}{\partial \mathrm{H_z}} \right)_T , \tag{3.14}$$

where N_A is Avogadro's number. In doing so, we arrive at a fraction which contains fourteen terms in the numerator and ten in the denominator. Using a computational program, such as Wolfram Mathematica, we can use the value for M to find the susceptibility, $\chi = \mu_0(\partial \mathrm{M}/\partial \mathrm{B_z})_T = (\partial \mathrm{M}/\partial \mathrm{H_z})_T$. For the sake of brevity, I will not include the full form in this text, as it contains 37 terms. However, for small magnetic fields (in the limit as $\mathrm{H_z} \to 0$), the susceptibility reduces to

$$\chi = \frac{N_A g^2 \mu_B^2}{k_B T} \frac{\mathrm{e}^{\frac{3J}{k_B T}}(2 + \mathrm{e}^{\frac{2J}{k_B T}} + 8\mathrm{e}^{\frac{3J}{k_B T}} + 9\mathrm{e}^{\frac{6J}{k_B T}})}{1 + 2\mathrm{e}^{\frac{3J}{k_B T}} + \mathrm{e}^{\frac{4J}{k_B T}} + \mathrm{e}^{\frac{5J}{k_B T}} + 2\mathrm{e}^{\frac{6J}{k_B T}} + \mathrm{e}^{\frac{9J}{k_B T}}}. \tag{3.15}$$

This solution describes the magnetic susceptibility with H along an easy axis. Note also that the derivation was done for a mole of dimers. Therefore if one wishes to apply this equation to a mole of magnetic ions, then an additional factor of 2 is required in the denominator. For the case of the two-sublattice models of the antimonates and tantalates, a factor of two is introduced in the denominator to account for only half of the spins contributing to the total susceptibility above the Néel temperature.

3.1.4 Heisenberg Chains of Arbitrary Spins

Prior to the advancements in computational physics, much progress in the theory of one-dimensional magnetism was made by Fisher [72]. A solution to the Heisenberg chain in the limit as $S \to \infty$ (i.e. when the spin is treated as a classical vector) came in the form

$$\chi = \frac{C_0 g^2}{12T} \frac{1 + L(x)}{1 - L(x)}, \tag{3.16}$$

where L is the Langevin function $L(x) = \coth(x) - 1/x$ and $x = (1/2)J/k_BT$. Upon decreasing temperature, the susceptibility of an antiferromagnet passes through a broad maximum whose height was determined by Fisher to be $\chi_{max}/\chi_0 = 1.2045$ at the temperature $T_{max} = 0.2382|J|/k_B$. At zero temperature, it approaches the limit $\chi_0 = C_0 g^2/12|J|$, where $C_0 = N_A\mu_B^2/k_B$. Fisher's model is frequently used for a large but finite spin S in the form

$$\chi_{mol} = \frac{C_0 g^2 S(S+1)}{3T}\frac{1+u}{1-u}, \tag{3.17}$$

with $u = \coth[2JS(S+1)/k_BT] - k_BT/[2JS(S+1)]$. However, this model does not take into account the spin degrees of freedom of larger spin values. Therefore the exchange constants determined using this model should serve simply as a guide.

With the advancements in computational physics in recent years, many theoretical physicists have been able to simulate a wide arrangement of magnetic and thermodynamic behavior via quantum Monte Carlo calculations and density-matrix renormalization group techniques. These simulations can then be fitted using Padé approximations to very high precision and compared with experimental results. While the final expressions may not be derived from first principles, they can nevertheless yield estimates of the exchange couplings. This procedure has been performed by Law *et al.* [73] for Heisenberg antiferromagnetic spin chains with S ranging from 1 to $\frac{7}{2}$ in half-integer steps. They begin with the Padé approximation of the form

$$f(x) = \frac{\sum_{i=0}^{m} A_i x^i}{1 + \sum_{j=1}^{n} B_j x^j}. \tag{3.18}$$

For simplicity, they define a reduced susceptibility $\chi^* = \chi_{mol} \times (J_{NN})/(N_A\mu_B^2 g^2)$, where χ_{mol} is the measured molar susceptibility and J_{NN} is the nearest-neighbor intrachain coupling. Similarly, we may define a reduced temperature, $T^* = k_BT/J_{NN}$. We set $f(x)$ equal to χ^* and introduce the factor $S(S+1)/3T^*$ in order to reproduce

the standard Curie-Weiss behavior at higher temperature. We must also introduce an exponential, e^{Δ/T^*}, to account for the Haldane energy gap at low temperature for integer spins. To ensure $\chi^* \propto 1/T$ at high temperatures, the authors set $A_0 = 1$. Equation 3.18 then takes the form

$$\chi^* = \frac{S(S+1)}{3T^*} \times e^{\Delta/T^*} \times \frac{1 + \sum_{i=1}^{m} A_i T^{*-i}}{1 + \sum_{j=1}^{n} B_j T^{*-j}}. \tag{3.19}$$

Substituting back in for the expressions of the reduced susceptibility and reduced temperature yields the final result

$$\chi_{mol} = \frac{N_A \mu_B^2 g^2 S(S+1)}{3k_B T} e^{\frac{\Delta J_{NN}}{k_B T}} \left(\frac{1 + \sum_{i=1}^{m} A_i (\frac{J_{NN}}{k_B T})^i}{1 + \sum_{j=1}^{n} B_j (\frac{J_{NN}}{k_B T})^j} \right). \tag{3.20}$$

The coefficients, A_i and B_j, for spins 1, $\frac{3}{2}$, 2, and $\frac{5}{2}$ are given in Table 3.2.

Table 3.2: Coefficients for the Padé approximation susceptibility reprinted from Law *et al.* [73]

S	1		3/2		2		5/2	
Δ	-0.41191		0		-0.090700		0	
i,j	A_i	B_j	A_i	B_j	A_i	B_j	A_i	B_j
1	0.67855	1.6000	0.48166	2.9834	0.97148	4.8815	1.6396	7.4637
2	1.2698	2.6533	0.91348	5.8136	3.1730	15.600	8.3090	36.873
3	0.65478	2.5159	0.11791	7.3541	2.4097	31.416	14.390	109.08
4	0.14123	1.6783	0.0054266	2.2637	0.068357	38.668	1.3478	317.81
5	0.087773	0.41951	-6.5501 $\times 10^{-7}$	0.12999	0.0045027	-0.19057	0.0062667	50.137
6	-9.1750 $\times 10^{-5}$	0.041205	0.0000	0.0000	-1.5760 $\times 10^{-5}$	0.023805	-3.5355 $\times 10^{-5}$	0.93478
7	0.0000	0.0000	0.0000	0.0000	-2.8681 $\times 10^{-7}$	-2.2655 $\times 10^{-4}$	-1.3877 $\times 10^{-8}$	-0.0038182

Useful ratios of thermodynamic quantities have also been determined by M. E. Lines [74] who related the exchange constant to the temperature at which the maximum susceptibility occurs. This was done using high-temperature series expansion and spin-wave theory applied to the antiferromagnetic susceptibility of a Heisenberg lattice for various spin values. Later, de Jongh [75] refined the results by adding additional terms to the series, as well as using the height of the broad susceptibility maximum, claiming that more reliable estimates of the exchange constants could be obtained. The resulting ratios are arranged in Table 3.3. These ratios serve as a quick estimate of the exchange coupling, and have been used many times throughout the literature of 1-d compounds.

Table 3.3: Estimated values for the temperatures at which the maxima occur in the antiferromagnetic susceptibility Heisenberg lattices. Table is reproduced from de Jongh and Miedema [75].

S	$\frac{1}{2}$	1	$\frac{3}{2}$	2	$\frac{5}{2}$	∞
$\frac{k_B T_{max}}{\lvert J\rvert S(S+1)}$	2.53(5)	2.20(2)	2.10(1)	2.07(1)	2.05(1)	2.01(1)
$\frac{\chi_{max}\lvert J\rvert}{N_0 g^2 \mu_B^2}$	0.0469(1)	0.0521(1)	0.0539(1)	0.0547(1)	0.0551(1)	0.0561(1)
$\frac{\chi_{max} T_{max}}{C}$	0.356	0.344	0.340	0.340	0.339	0.338

3.2 Heat Capacity

Heat capacity is an extensive property of matter, which means that it scales with the sample size. It is equal to the amount of heat added or removed from an object divided by the resulting temperature change. To better compare this property against other samples of different sizes, the heat capacity is normalized by mass, volume, or molar amount, giving the *specific heat*. Thermodynamically, the specific heat $C(T)$ is

related to the amount of entropy S at a given temperature T. Therefore, both $C(T)$ and S approach zero as $T \to 0$ in accordance with the Third Law of Thermodynamics.

3.2.1 Determining Magnetic Entropy From Specific Heat

Of great interest to the following investigations is the amount of *magnetic* specific heat. To determine the theoretical maximum value, we begin using the standard definition of entropy $S_m = k_B \ln \Omega$, where Ω is the number of distinct microscopic states available to the system. For a particular atom, the maximum number of different possible states of quantum number $\mathcal{J}$ for a given combination of L and S is $2S + 1$, and is called the *spin multiplicity*. Here, L and S are the usual quantum orbital angular momentum and spin angular momentum, respectively. For a mole of atoms, the number of microstates will therefore be the spin multiplicity raised to Avogadro's number. Since the heat capacity, and in turn the entropy, has been normalized by the number of moles in the crystal samples, we may write the total possible magnetic entropy as:

$$S_m = k_B \ln \Omega, \tag{3.21a}$$

$$= k_B \ln[(2S+1)^{N_A}], \tag{3.21b}$$

$$= N_A k_B \ln(2S+1), \tag{3.21c}$$

$$= R \ln(2S+1). \tag{3.21d}$$

Experimentally, the change in magnetic entropy over a specific temperature range at constant H can be determined from the heat capacity of the $M(\mathrm{Sb,Ta})_2\mathrm{O}_6$ sample and subtracting from it the heat capacity data of a nonmagnetic analog, namely $\mathrm{ZnSb_2O_6}$ or $\mathrm{MgTa_2O_6}$. We therefore write the magnetic portion of the heat capacity (at constant pressure) as $\delta C_P = C_P^{\mathrm{total}} - C_P^{\mathrm{nonmagnetic}}$. We may replace C_P with δC_P in

the well-known equation $T\mathrm{d}S = C\mathrm{d}T$ and solve for $\mathrm{d}S$. Upon integrating, we arrive at the expression for the change in magnetic entropy

$$\Delta S_m(T) = \int_{T_{\min}}^{T_{\max}} \left(\frac{\delta C_P(T)}{T} \right) \mathrm{d}T. \tag{3.22}$$

By plotting Eq. 3.22 and comparing its saturation value with Eq. 3.21d, we can determine the approximate percent of magnetic moments that remain disordered after cooling through a temperature range ΔT.

3.2.2 Short-Range Order

A broad hump observed in *magnetic* heat capacity above the Néel temperature T_N is often due to short-range order. At lower temperatures, only the lower energy levels will be populated with low probability of transitions between levels. Consequentially, entropy, and therefore C_m goes to zero as T goes to zero. At higher temperatures, both lower and upper energy levels are equally populated and the energy scales of thermal excitations are irrelevantly large, thus transition probability is insignificant. Only when the temperature is on the order of $(E_2 - E_1)/k_B$, where E_1 and E_2 are the energies associated with the lower and excited state, do transitions occur at an appreciable degree. As transitions occur, there is a large change in entropy for a small change in temperature, leading to a large term in C_m (see Tari [76]).

To characterize the resulting broad peak in C_m, let us define the separation $\Delta = (E_2 - E_1)/k_B$. In the context of short-range order, this difference in energy is associated with gap between the local AFM ordered state and the paramagnetic state. The partition function can be written as

$$Z = \sum_{i=1}^{2} exp(-E_i/k_B T). \tag{3.23}$$

The average thermal energy is then

$$E = k_B T^2 \left(\frac{\partial \ln Z}{\partial T} \right) = E_1 + \frac{k_B \Delta}{1 + e^{(\Delta/T)}}. \tag{3.24}$$

Specific heat can be obtained by taking the derivative with respect to temperature and multiplying by Avogadro's number to yield

$$C = R \left(\frac{\Delta}{T} \right)^2 \frac{e^{(\Delta/T)}}{[1 + e^{(\Delta/T)}]^2}. \tag{3.25}$$

This function exhibits a broad maximum when plotted versus temperature and is nearly identical to the magnetic heat capacity derived for a mole of ions in the dimerized state [47]. We can find the center of the peak, T_{max}, by making the substitution $u = (\Delta/T)$ and setting $\partial C/\partial u = 0$. This leads to the transcendental equation

$$e^u = \frac{u + 2}{u - 2}, \tag{3.26}$$

which has the solution $u \approx 2.399$, and in turn $T_{max} = \Delta/u \approx 0.42\Delta$. Therefore the temperature associated with the peak in magnetic heat capacity is directly proportional to the difference in energy levels. Substituting this value for T_{max} into Eq. 3.25 yields $C_{max} = 3.6$ J/mol K.

3.3 Magnetocaloric Effect

The magnetocaloric effect (MCE) is a basic physical property of magnetic solids. It can be characterized as either an adiabatic temperature change or an isothermal change in entropy, ΔS_m, upon application of an external magnetic field. The sign and magnitude of these changes between the initial and final states depend on various factors. These include the amount of material, the interatomic coupling, and the temperature of the maxima in ΔS_m which usually occurs around the magnetic phase

transition. Large MCEs are usually found in materials with strong magnetic ordering, such as ferromagnets, but the effect can also be observed in antiferromagnets, albeit to a lesser degree.

3.3.1 Maxwell Relation

A useful relation pertaining to the magnetocaloric effect can be derived from the equation for the Helmholtz free energy, $F = E - TS$, where the enthalpy, E, equals $U - \mu_0 HM$. Noting that $\mathrm{d}E = \mathrm{d}U - \mu_0 H\mathrm{d}M - \mu_0 M\mathrm{d}H = T\mathrm{d}S - \mu_0 M\mathrm{d}H$, it immediately follows that

$$\mathrm{d}F = \mathrm{d}E - T\mathrm{d}S - S\mathrm{d}T = -\mu_0 M\mathrm{d}H - S\mathrm{d}T. \tag{3.27}$$

Mixed partial derivatives are identical for functions with continuous second derivatives. That is to say they obey the general expression

$$\frac{\partial}{\partial y}\left(\frac{\partial z}{\partial x}\right)\bigg|_y = \frac{\partial}{\partial x}\left(\frac{\partial z}{\partial y}\right)\bigg|_x. \tag{3.28}$$

Applying Eq. 3.28 to the right side of Eq. 3.27, we obtain the Maxwell relation

$$\left(\frac{\partial M}{\partial T}\right)\bigg|_H = \frac{1}{\mu_0}\left(\frac{\partial S}{\partial H}\right)\bigg|_T. \tag{3.29}$$

Equation 3.29 is fundamental to the magnetocaloric analysis later in this dissertation.

3.3.2 Magnetocaloric Temperature Shift

The change in temperature of a magnetocaloric material in response to a change in magnetic field can be determined first by observing the chain rule on the entropy differential element, $\mathrm{d}S$:

$$\mathrm{d}S = \left(\frac{\partial S(T,H)}{\partial T}\right)\bigg|_H \mathrm{d}T + \left(\frac{\partial S(T,H)}{\partial H}\right)\bigg|_T \mathrm{d}H. \tag{3.30}$$

If the temperature rises slowly enough that we can assume the process to be adiabatic so that $\mathrm{d}S = 0$, then the two terms in Eq. 3.30 are equal in magnitude and opposite in sign. We can then write

$$\left(\frac{\partial S(T,H)}{\partial T}\right)\bigg|_H \mathrm{d}T = -\left(\frac{\partial S(T,H)}{\partial H}\right)\bigg|_T \mathrm{d}H. \tag{3.31}$$

The left term is related to heat capacity $C(T,H)$ through the the well-known thermodynamic relation

$$C(T,H)_H = T\left(\frac{\partial S(T,H)}{\partial T}\right)\bigg|_H. \tag{3.32}$$

Note that this heat capacity is for the whole system and contains magnetic, electronic, and lattice contributions. The right term in Eq. 3.31 can be replaced by the derivative of the magnetization as per Eq. 3.29. What remains is the following relation

$$\left(\frac{C(T,H)}{T}\right)\bigg|_H \mathrm{d}T = -\mu_0\left(\frac{\partial M(T,H)}{\partial T}\right)\bigg|_H \mathrm{d}H. \tag{3.33}$$

Isolating the temperature differential element and integrating over the applied field range results in the change in temperature

$$\Delta T = -\mu_0 \int_0^{H_{\max}} \left(\frac{T}{C(T,H)}\right)\left(\frac{\partial M}{\partial T}\right)\bigg|_H \mathrm{d}H. \tag{3.34}$$

It is clear from this relation that the largest change in temperature will result either when the heat capacity C is low or when there is a rapid change in M with respect to temperature. Low heat capacity usually occurs at low temperature, which limits the influence of the T/C term. The largest contribution therefore comes from large variations in $M(T)$, i.e. near a magnetic phase transition. Because both C and T can only be positive, the sign of ΔT is determined by sign of $\partial M/\partial T$. Antiferromagnetic transitions should therefore accompany a negative change in temperature, while ferromagnetic transitions should result in a positive change.

4. MAGNETIZATION

4.1 Introduction

While magnetization measurements performed on poly-crystals or powders can provide useful information about the behavior of the magnetic moments in an applied field, an even greater understanding can be obtained with the use of single-crystalline samples. The behavior of χ for various orientations of H can reveal possible anisotropy and lend insight into a sample's magnetic structure. The antiferromagnetic easy axis can be determined by a sudden drop in the magnetization upon cooling since the anti-aligned moments tend to cancel. Measurements along a hard axis often result in a magnetization that saturates to a constant value as $T \rightarrow 0$. If, however, H is applied parallel to the axis along which the moments lie, $\chi \rightarrow 0$ [52]. Identification of the easy and hard axes is essential to any thorough investigation of a sample's magnetic properties.

The magnetization data in the following sections were obtained using vibrating-sample magnetometry (VSM) provided by the Physical Properties Measurement System (PPMS). The magnetometer has a resolution of about 10^{-6} emu [77] and is capable of measuring within the temperature range $1.9 < T < 400$ K. The change in temperature during a measurement can be set between 0.01 and 12 K/min. Rates for the experiments reported herein were typically 0.1 to 1 K/min to allow the samples to reach temperature equilibrium. A magnetic field between 0 and 90,000 Oe can be provided by a longitudinal superconducting solenoid composed of a Nb-Ti alloy embedded in copper [78]. The field is estimated to have a uniformity which deviates only 0.01% over a 5.5 cm region.

The samples are affixed to either a quartz or G-10 fiberglass sample paddle using Duco cement. The cement can be diluted with acetone to adjust the viscosity if needed. The sample paddle is then attached to a long sample rod that is driven by a linear transport motor at a frequency $f = 40$ Hz through a coil installed in the PPMS. A voltage is induced within the detection coils due to the changing magnetic flux as the sample vibrates. The induced voltage can be determined through the use of Lenz's Law

$$\mathcal{E}_{coil} = -\frac{\mathrm{d}\phi}{\mathrm{d}t} = -\left(\frac{\mathrm{d}\phi}{\mathrm{d}z}\right)\left(\frac{\mathrm{d}z}{\mathrm{d}t}\right), \tag{4.1}$$

where z is the vertical sample position given by $z(t) = A\cos(2\pi ft)$. The oscillation amplitude A is typically 1-3 mm. The quantity $(\mathrm{d}\phi/\mathrm{d}z)$ is proportional to the magnetization M with a coupling constant c, which has units of Oe m emu^{-1} [77]. The induced voltage within the coil is therefore

$$\mathcal{E}_{coil} = 2\pi fcMA\sin(2\pi ft). \tag{4.2}$$

Lock-in detection allows the coefficient of Eq. 4.2 to be accurately measured [79]. With all other quantities known, the magnetization M is easily extracted.

4.2 Magnetic Susceptibility

Traditionally, magnetization M is defined as the sum of magnetic moments per sample volume, which has units of (A m^2)/m^3 = A/m, the same as the magnetic field H. Magnetic susceptibility χ is defined as the partial derivative of M with respect to an applied field. Very often, M is linear in H for attainable field strengths (as in antiferromagnets and paramagnets, for example), and so the susceptibility can be written as $\chi = M/H$. Since M and H have the same dimensions, χ is a dimensionless quantity. However, it is most often the case that M is reported in CGS units of

emu cm^{-3}. (Note that 10^3 emu = 1 A m^2.) The PPMS used to measure magnetic properties of the samples in the following sections only reports the magnetic moment (in emus), and not actually M. It is therefore the choice of the user to normalize to volume, mass, or molar quantity depending upon if they wish to report χ_{vol} [dimensionless], χ_{mass} [cm^3/kg], or χ_{mol} [cm^3/mol], respectively. Here we shall use the molar magnetic susceptibility.

4.2.1 $CuSb_2O_6$

The magnetic susceptibility χ below 300 K was measured with H along various crystallographic directions to investigate the anisotropy. The data were corrected for diamagnetism and plotted in Fig. 4.1a. $\chi(T)$ fails to tend toward zero below $T_N = 8.7$ K for any of the applied field directions. The moments seem to be ordered perpendicular to [001] (i.e., perpendicular to the c direction). The decrease of χ below T_N is more significant when H is applied along [010] than when H is applied along [100]. Therefore, it seems reasonable to deduce that the alignment of the moments in $CuSb_2O_6$ is nearly parallel to [010], which agrees best with two of the neutron diffraction data reports [8, 27]. The preference of the moments to align more along the [010] axis may be associated with the distorted oxygen octahedra caused by the Jahn-Teller effect, leading to weak differences in the magnetocrystalline energy between the a and b axes.

The height and position of the peak in $\chi(T)$ can be compared against that of an ($S = 1/2$) antiferromagnetic uniform Heisenberg chain obtained from the EAT theory discussed in Section 3.1.1. The observed ratios are provided in the rightmost column of Table 4.1 and are in good agreement with the theory [54]. This analysis has also been done by Prokofiev *et al.* who obtained comparable results. The agreement

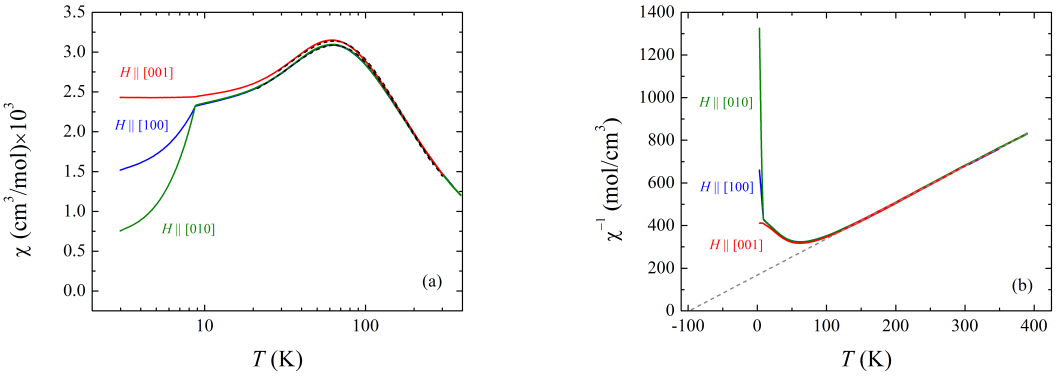

Figure 4.1: (a) Magnetic susceptibility χ versus temperature T for $CuSb_2O_6$ in an applied field, $\mu_0 H = 0.5$ T. A transition to long-range order occurs at $T_N = 8.7$ K. Dashed black lines are fits using the Bonner-Fisher model of Eq. 3.7. (b) Inverse magnetic susceptibility $1/\chi$ versus temperature T. The dotted lines are Curie-Weiss fits for $T > 125$ K extrapolated to illustrate the T intercepts.

allows us to analyze the data more confidently using the Bonner-Fisher model for a ($S = 1/2$) Heisenberg chain provided by Eq. 3.7. The expression was applied to both the $H \perp [001]$ and $H \parallel [001]$ data shown in Fig. 4.1a. The model and the observed data are in good agreement, resulting in an exchange coupling $J/k_B = 98(2)$ K and Landé g-factors $g_\parallel = 2.35(1)$ and $g_\perp = 2.37(1)$ for H within the magnetic plane and $H \parallel [001]$, respectively. The value of the exchange constant is very close to $J/k_B = 93$ K determined by Heinrich *et al.* [22]. Unfortunately the theory cannot distinguish between inter- and intrachain exchange coupling.

Additional analysis of $\chi(T)$ was conducted using the Curie-Weiss equation $\chi = C/(T - \theta) + \chi_0$ that describes paramagnetism. Deviation from this behavior signifies the presence of short-range antiferromagnetic interactions. Here, θ is the Curie-Weiss temperature, χ_0 is a temperature-independent constant and C is the Curie-Weiss constant. The data were fit for $T > 125$ K, which is above the region ($T < 115$ K) where local 1-d antiferromagnetic order appears (see Section 5.2). The

Table 4.1: Comparison of calculated physical parameters for the AFM $S = 1/2$ Heisenberg chain. Values in the far right column are in good agreement with Eq. (3.4) for a *uniform* chain, indicating that the model accurately describes $CuSb_2O_6$.

Axis	χ_{max} (cm^3/mol)	T_{max} (K)	J/k_B (K)	g	$\frac{\chi_{max} J}{N g^2 \mu_B^2}$
a	3.089×10^{-3}	62.5	97.5	2.34	0.147
b	3.095×10^{-3}	62.2	97.1	2.33	0.148
c	3.150×10^{-3}	61.9	96.6	2.35	0.147

results are shown graphically by the dashed lines in Fig. 4.1b. The effective magnetic moment can be determined by comparing C with the theoretical value

$$C = \frac{N g^2 \mu_B^2 \mathcal{J}(\mathcal{J}+1)}{3k_B} = \frac{N \mu_{\text{eff}}^2}{3k_B}, \tag{4.3}$$

where N is the number of moles, $\mathcal{J}$ is the quantum number associated with the total angular momentum $L+S$, μ_B is the Bohr magneton, and g is the Landé g-factor. The orbital-angular momentum, L, is typically quenched for 3d ions [80], making $\mathcal{J} = S$. The values of μ_{eff} determined from the various curves are in agreement, as expected for the paramagnetic state, resulting in $\mu_{\text{eff}} = 2.17(1)\mu_B$.

4.2.2 $Ni(Sb,Ta)_2O_6$

Magnetic susceptibility χ of $NiSb_2O_6$ and $NiTa_2O_6$ was measured over the temperature range 2 K < T < 300 K and corrected for temperature independent diamagnetism associated with the core electrons ($\chi_{dia} = -112 \times 10^6$ cm^3/mol) [81]. The results are shown in Fig. 4.2. A broad maximum centered near 34 K for the antimonate and 25 K for the tantalate is immediately apparent. This difference in temperature indicates a larger intralayer exchange coupling between magnetic ions in the antimonate, i.e. the exchange coupling associated with magnetic order is able to better compete against thermal vibrations. All measurements of χ with $H \perp [001]$

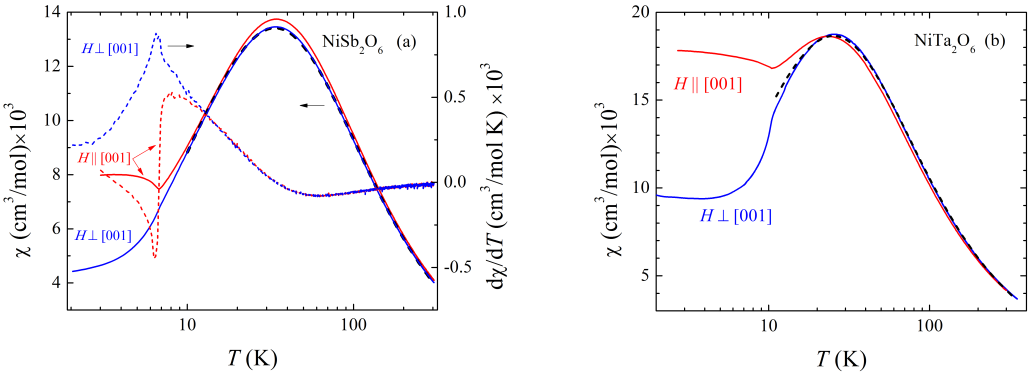

Figure 4.2: (a) Magnetic susceptibility χ versus temperature T for $NiSb_2O_6$. Applied field is $\mu_0 H = 0.2$ T. The short-dashed lines are the derivatives $d\chi/dT$ (right scale) shown to emphasize the transition at $T_N = 6.7(1)K$. (b) $\chi(T)$ for $NiTa_2O_6$ with applied field $\mu_0 H = 0.1$ T. Long-range order occur at $T_N = 10.5$ K. For each plot, black dashed lines are fits using Eq. 3.20 for $S = 1$.

(which include $H \parallel [110]$, $H \parallel [1\bar{1}0]$, $H \parallel [100]$, and $H \parallel [010]$) are nearly identical in appearance for either compound. The saturation of $\chi(T)$ to constant values as $T \to 0$ reveals there is no single direction in either compound along which all the moments are aligned.

The transition to long-range order is observed as a cusp-like minimum in $\chi_{H\parallel[001]}$ and as a change in slope of $\chi_{H\perp[001]}$ near $T_N = 6.7$ K for $NiSb_2O_6$ and $T_N = 10.5$ K for $NiTa_2O_6$. This transition when $H \perp [001]$ in the former compound is subtle and better observed when plotted as $d\chi/dT$. Curie-Weiss fits have been applied above $T = 100$ K (not shown) and values for the magnetic moments were obtained with the use of Eq. 4.3. The analysis results in $\mu_{\text{eff}} = 3.32(2)\mu_B$, $\theta = -49.6(4)$ K, and $\chi_0 = 1.8(2) \times 10^{-4}$ cm^3/mol for $NiSb_2O_6$ and $\mu_{\text{eff}} = 3.26(2)\mu_B$, $\theta = -30.7(4)$ K, and $\chi_0 = 2.7(3) \times 10^{-4}$ cm^3/mol for $NiTa_2O_6$. The magnetic moments of both compounds are very close to the value $3.2\mu_B$ typical for the Ni^{2+} ion with $S = 1$ [82]. The temperature-independent constant is often attributed to Van Vleck paramagnetic

susceptibility. Van Vleck contributions of $\chi_0 \sim 2 \times 10^{-4}$ cm^3/mol are typical for these compounds [14, 73].

Law *et al.* [14] previously investigated magnetic susceptibility of powder samples of $NiTa_2O_6$. They fit their data to the expression for a ($S = 1$) Heisenberg chain reviewed in Section 3.1.4. The curve approximated the data very well resulting in a Landé-factor $g = 2.140(2)$ and exchange coupling $J/k_B = -18.92(2)$ K along the chains. While they do not provide the actual value, Law *et al.* claim the interchain coupling is about two orders of magnitude smaller than the intrachain coupling. The same analysis is repeated here for $Ni(Sb,Ta)_2O_6$ over the temperature range 10 K < T < 300 K (see black dashed curves in Fig. 4.2a). For $NiSb_2O_6$, the fit yields $J/k_B = -26.0(1)$ K and $g = 2.297(3)$ with a temperature independent offset $\chi_0 = 1.2(1) \times 10^{-4}$ cm^3/mol. Similarly for $NiTa_2O_6$ (Fig. 4.2b), we obtain $J/k_B = -19.41(2)$ K and $g = 2.355(1)$ with a temperature independent offset $\chi_0 = 5.9(8) \times 10^{-5}$ cm^3/mol. The slight discrepancy between the current values and those provided by Law *et al.* is likely due to the single-crystalline nature of our samples. The larger exchange constant determined for the antimonate reaffirms the statement above concerning the temperature around which the broad maximum is centered and its relation to the coupling between ions. The values of χ_0 are comparable to those obtained from the Curie-Weiss analysis. The Landé g-factor is in the neighborhood of 2.25 typical for Ni^{2+} ions in an octahedral environment [71], suggesting the above model is reasonable. An alternate fit using an Ising model [83] with $S = 1$ was attempted in the current investigation (not shown) but the result failed to capture the curve below 40 K in the case $NiSb_2O_6$. In the case of $NiTa_2O_6$ the fit resulted in unrealistic parameters.

4.2.3 $Co(Sb,Ta)_2O_6$

The magnetic susceptibility χ of $CoSb_2O_6$ and $CoTa_2O_6$ at $\mu_0 H = 0.2$ T is shown in Fig. 4.3. In each case, data obtained with $H \perp [001]$ are identical within experimental uncertainty. The data were corrected for the temperature-independent diamagnetism, $\chi_{dia} = -112 \times 10^{-6}$ cm^3/mol [81]. A transition due to long-range antiferromagnetic order is observed at $T_N = 13.45$ K for $CoSb_2O_6$ and $T_N = 6.12$ for $CoTa_2O_6$. The fact that the data for $H \perp [001]$ and $H \parallel [001]$ do not tend toward zero as $T \to 0$ suggests that the moments are not aligned along any single axis. Cooling in magnetic field (FC) and cooling in zero magnetic field, followed by application of field (ZFC), exhibited no difference in $\chi(T)$. This conflicts with a prior report [84], where the FC susceptibility differed from the ZFC susceptibility below the broad peak. The authors attributed this behavior to spin-freezing, which must be associated with the polycrystalline nature of their samples.

Anisotropy is observed in the broad peaks of $\chi(T)$; specifically, peaks for $H \perp [001]$ occur at higher temperature than peaks for $H \parallel [001]$. This suggests the intralayer coupling is stronger than the interlayer coupling. Such behavior in χ is very different from the other compounds discussed previously, which were determined to contain Heisenberg (isotropic) interactions. Doubly-ionized cobalt ions, on the other hand, are said to be among the best examples of Ising ions [71]. Anisotropy is therefore expected both in χ and in the values of J/k_B between measurements with H applied parallel and H applied perpendicular to [001].

In the case of $CoTa_2O_6$, the height of the broad peak, χ_{max}, with $H \parallel [001]$ is greater than χ_{max} with $H \perp [001]$; the opposite of that observed in the antimonate. Both compounds contain cobalt ions with moments indicative of high-spin states, so the magnitude of χ should be similar. The observed difference must then be

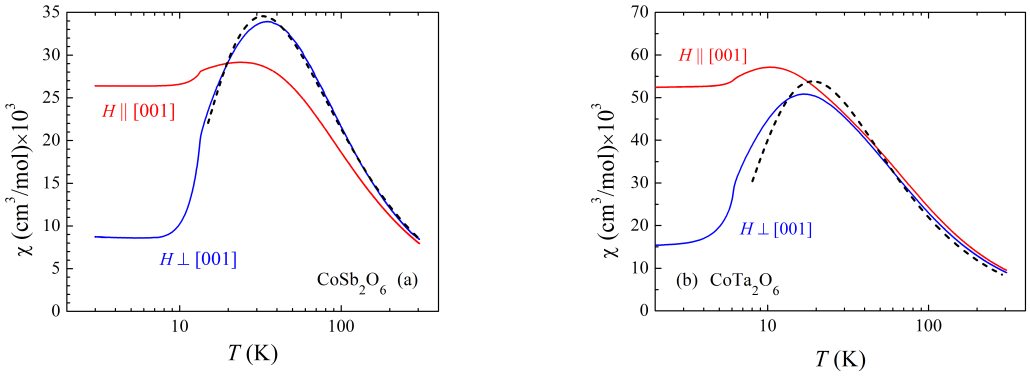

Figure 4.3: (a) Magnetic susceptibility χ versus temperature T for $CoSb_2O_6$. The broad peaks are centered at 23.6 K and 34.3 K. Long-range order occur at $T_N = 13.45$ K. (b) Magnetic susceptibility χ versus temperature T for $CoTa_2O_6$. The broad peaks are centered at 10.4 K and 16.9 K. Long-range order occur at $T_N = 6.12(5)$ K. In both figures, $\mu_0 H = 0.2$ T. Black dashed curves are theoretical fits using the $S = 3/2$ Ising model from Eq. 3.15.

associated with short-range order. The behavior suggests a stronger intralayer and interlayer coupling present in the antimonate than in the tantalate.

The Curie-Weiss equation was fit to $\chi(T)$ above 100 K. Equation 4.3 was used to obtain the effective magnetic moments and Van Vleck susceptibility shown in Table 4.2. For comparison, $\mu_{\text{eff}} = 4.62(1)\mu_B$ was reported for a polycrystalline sample of $CoSb_2O_6$ [29]. The observed magnetic moment reveals that the Co^{2+} ions are in the $S = 3/2$ state with $g = 2.43$. Deviation from $g = 2.00$ is common for 3d elements with their d-shells more than half full, and is associated with the spin-orbit interaction. For Co^{2+} with $S = 3/2$, a typically observed value [82] for μ_{eff} is $4.8\mu_B$, close to what is observed here. The average of the Curie-Weiss temperatures for $CoSb_2O_6$ is similar to $\theta = -32.4$ K reported for a polycrystalline sample [29]. The temperature-independent paramagnetism χ_0 is comparable to the Van Vleck value $\chi_{VV} \sim 4.0 \times 10^{-4}$ cm^3/mol observed in Co^{2+} [85].

Table 4.2: Results of Curie-Weiss analysis for $Co(Sb,Ta)_2O_6$.

Compound	Axis $\parallel H$	μ_{eff} [μ_B]	θ [K]	χ_0 [cm^3/mol]
$CoSb_2O_6$	[100]	4.6827(1)	−24.95(2)	$3.36(3) \times 10^{-4}$
	[010]	4.667(1)	−25.84(5)	$1.77(3) \times 10^{-4}$
	[001]	4.697(1)	−47.18(6)	$6.14(3) \times 10^{-4}$
$CoTa_2O_6$	[100]	4.713(1)	−23.0(1)	$4.53(5) \times 10^{-4}$
	[010]	4.691(1)	−22.7(1)	$4.65(6) \times 10^{-4}$
	[001]	4.973(3)	−27.7(1)	$2.25(6) \times 10^{-4}$

To model the general behavior of $\chi(T)$ associated with the a-b plane, we turn to the expression for the ($S = 3/2$) Ising model derived in Section 3.1.3. The results are shown in Fig. 4.3 as black solid curves. The fits yield $g_{\parallel} = 2.4442(5)$ and $J/k_{\text{B}} = -10.603(6)$ K for $CoSb_2O_6$ and $g_{\parallel} = 2.34(2)$ and $J/k_B = -6.1(2)$ K for $CoTa_2O_6$. The ratio of the exchange couplings is comparable to that reported for polycrystalline $CoSb_2O_6$ and $CoTa_2O_6$ [29]. Unfortunately, Ising model expressions for $\chi_{\perp}$ (i.e. when field is along a hard axis) are not well established, especially for $S > 1/2$. Therefore, reliable extraction of interlayer exchange coupling remains elusive.

4.2.4 $FeTa_2O_6$

Magnetic susceptibility of powder samples of $FeTa_2O_6$ has been analyzed previously by Eicher *et al.* [30]. They attempted to characterize the magnetic interactions by fitting the data using a $d = 2$, $D = 3$ (planar Heisenberg) model with $S = 2$. This attempt failed to provide a reasonable g-factor and was therefore rejected. A second attempt using a planar $S = 1/2$ Ising model resulted in a better fit at low temperature, but underestimated χ above ~ 25 K. The inability to fit the high temperature data was attributed to an absence of Van Vleck contributions of the excited levels which

become important as the temperature increases. However, Van Vleck contributions are much too small to account for the observed discrepancy. This fact was pointed out by Muraoka *et al.* [86] who also analyzed the magnetic susceptibility of powder samples. They derived a lengthy expression for a two-dimensional Heisenberg model with a single-ion anisotropy term K (called D in the original text) which could be adjusted to describe how Ising-like or Heisenberg-like the system behaved. Their analysis resulted in a good fit with nearest-neighbor interactions $J/k_B = -0.41$ K, $g_{\parallel} = 2.98$, $g_{\perp} = 1.13$, and $K/k_B = 6.8$ K. The value of the single-ion anisotropy was considered large, leading Muraoka *et al.* to claim $FeTa_2O_6$ to be Ising-like.

Magnetic susceptibility versus applied field for a single-crystalline sample of $FeTa_2O_6$ has been measured and is shown in Fig. 4.4a. The center of the broad maxima occur at 9.8 K and 15.3 K for H parallel and perpendicular to [001], respectively. The behavior is very similar to $CoTa_2O_6$, in that χ_{max} for $H \parallel [001]$ is greater than χ_{max} for $H \perp [001]$ and suggests an Ising-like anisotropy. From the Curie-Weiss law (see Fig. 4.4b) we obtain $\chi_0 = 3.38(2) \times 10^{-4}$ cm^3/mol, $\theta = -7.51(2)$ K, and $\mu_{\text{eff}} = 5.005(1)\mu_B$ for $H \parallel [110]$ and $\chi_0 = 4.50(2) \times 10^{-4}$ cm^3/mol, $\theta = -7.29(3)$ K, and $\mu_{\text{eff}} = 4.90(2)\mu_B$ for $H \parallel [001]$. The value of the effective moment suggests a high-spin state (the low-spin state contains no unpaired electrons, resulting in no effective moment).

A fit using the 1-d Heisenberg chain provided by Eq. 3.20 was attempted, but was not able to capture the data around the broad maximum (see dashed grey curve in Fig. 4.4a). However, an ($S = 2$) Ising model derived by following the steps outlined in Section 3.1.3 was applied to the data for $H \perp [001]$ with much greater success. The fit (shown as a black solid line) captures the data rather well, resulting in $J/k_B = -2.888(6)$ K and $g = 2.134(1)$. While this model is derived using basic first

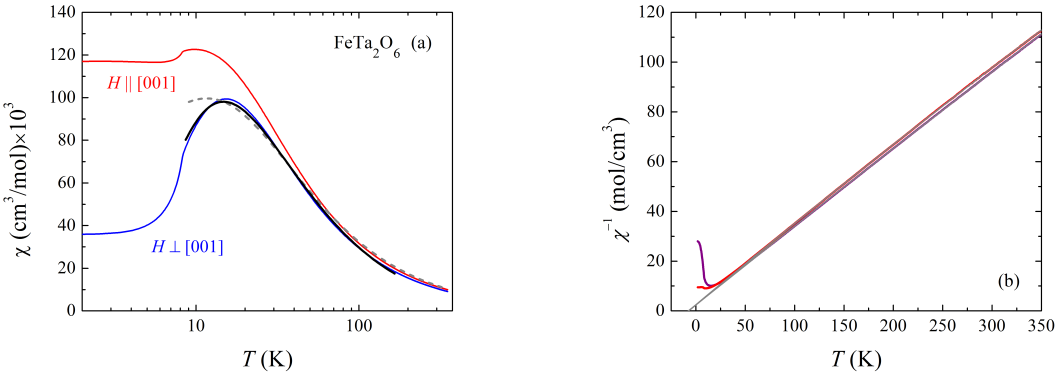

Figure 4.4: (a) Magnetic susceptibility χ versus temperature T for $FeTa_2O_6$ with $\mu_0 H = 0.1$ T. Long-range order occurs at $T_N = 8.24(7)$ K. The data is fit well above T_N using a $S = 2$ Ising model represented by the black solid line. The dashed grey curve is that of the $S = 2$ Heisenberg model using Eq. 3.20, which does not fit the data as adequately. (b) Inverse magnetic susceptibility $1/\chi$ versus temperature T. The dotted lines are Curie-Weiss fits for $T >$ K extrapolated to illustrate the T intercepts.

principles, it nevertheless helps support the claim by Muraoka *et al.* that $FeTa_2O_6$ shows properties characteristic of an Ising system.

4.2.5 $MnSb_2O_6$

Magnetic susceptibility measurements were performed on a single-crystalline $MnSb_2O_6$ sample with field parallel to [100], [010], [110], and [001]. The data were corrected for the diamagnetic contribution associated with closed atomic shells (-114×10^{-6} cm^3/mol) and are shown in Fig. 4.5a. Susceptibility measured with $H \parallel [001]$ tends toward zero below $T_N = 11.9(1)$ K, suggesting that the magnetic moments are anti-aligned along this axis, in agreement with the previous reports [33, 35]. Measurements with field perpendicular to [001] are identical within experimental uncertainty. The inverse susceptibility χ^{-1} is linear above ~ 50 K (see Fig. 4.5b) and was fit using the Curie-Weiss equation, yielding $\theta = -21.73$ and $\mu_{\text{eff}} = 5.909\mu_B$ for

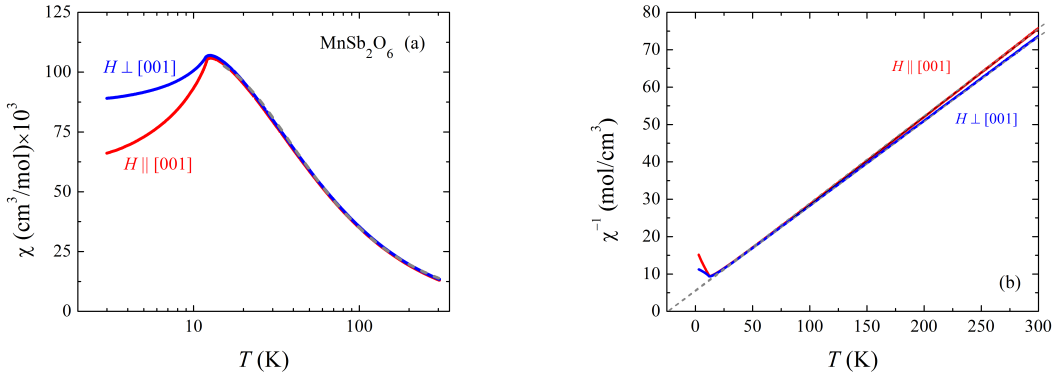

Figure 4.5: (a) Magnetic susceptibility χ versus temperature T for $MnSb_2O_6$ with $\mu_0 H = 0.1$ T. The dashed grey curve is the fit given by Eq. (3.20). χ with H parallel to [100], [010], [110], and $[\bar{1}10]$ are identical. (b) Inverse magnetic susceptibility $1/\chi$ versus temperature T. The dotted lines are Curie-Weiss fits for 50 K $< T <$ 300 K extrapolated to illustrate the T intercepts.

$H \parallel [001]$ and $\theta = -23.99$ and $\mu_{\text{eff}} = 5.922\mu_B$ for $H \perp [001]$. The Curie-Weiss temperatures are comparable to the value $\theta = -19.6$ K reported by Johnson *et al.* [33]. The magnitudes of the magnetic moments are in agreement with the spin-only moment $5.92\mu_B$ for $(S = 5/2)$ Mn^{2+} [82] as well as the value initially measured by Reimers *et al.* using a Curie-Weiss fit above 200 K. Below this temperature, the susceptibility they measured deviated from the Curie-Weiss law, which they attributed to short-range order. The onset of short-range order occurs much lower in the current study on single-crystals.

As shown in Section 3.1.4, Law *et al.* calculated the magnetic susceptibilities of Heisenberg antiferromagnetic spin chains for various spin values, including $S = 5/2$, using Padé approximations [73]. Their results were compared against the susceptibility of the well-known 1-d chain compound $(CH_3)_4N[MnCl_3]$ (also called TMMC), which contains spin 5/2 atoms in order to extract associated coefficients. Here we apply their result, Eq. (3.20), with the coefficients for $S = 5/2$ shown in Table 3.2

to the data in Fig. 4.5a over the temperature range 14 K − 300 K. The fit yields a vertical offset of 0.00169(1) cm^3/mol attributed to the temperature-independent Van Vleck paramagnetism. A nearest-neighbor intrachain spin-exchange interaction was found to be $J_{NN}/k_B = 2.478(2)$ K, corresponding to 0.213 meV. This quantity falls below the range of DFT-calculated values (0.4-2.2 meV) for coupling along various directions reported by Johnson *et al.* [33]. While the fit agrees visually with the data, the discrepancy in the exchange coupling may reflect a possible shortcoming of Eq. (3.20).

4.3 Magnetization and Spin-Flop Transitions

Measuring magnetization versus applied field while holding temperature constant and below T_N can provide insight concerning not only the direction of magnetic moments with respect to the principle axes but also an approximation of the anisotropy energy. If, upon application of an external magnetic field H, the magnetic moments remain collinear with the easy axis, then the change in free energy per unit volume is given by [87]

$$\Delta F = -\int_0^H \mu_0 \chi_\parallel H \mathrm{d}H = -\frac{1}{2}\mu_0 \chi_\parallel H^2. \tag{4.4}$$

For moments which lie perpendicular to the easy axis, the anisotropy fields produce a restoring torque that prevents the moments from fully aligning with the field. Instead, the moments will cant slightly and produce a small net magnetization. $\chi_\parallel$ is then replaced by $\chi_\perp$ in Eq. 4.4. If the anisotropy energy, K, does not equal zero we will have $\Delta F = K - \frac{1}{2}\mu_0 \chi_\perp H^2$ for the perpendicular orientation. Since $\chi_\perp > \chi_\parallel$ for an antiferromagnetic material at temperatures below T_N, the parallel orientation would be the ground state (lowest energy) provided H is not too large. At a certain critical

field H_{SF} where the energy of the two orientations are equal, we have [87]

$$-\frac{1}{2}\mu_0\chi_{\parallel}H_{SF}^2 = K - \frac{1}{2}\mu_0\chi_{\perp}H_{SF}^2. \tag{4.5}$$

Solving for K, we obtain the value

$$K = \frac{1}{2}\mu_0(\chi_{\perp} - \chi_{\parallel})H_{SF}^2. \tag{4.6}$$

For $H < H_{SF}$, the moments which started out parallel to the easy axis will remain parallel. For $H > H_{SF}$, the moments will rotate to be perpendicular to the field, then subsequently cant and thereby increase the net magnetization. This phenomenon is called a spin-flop transition, also known as a Morin transition. The value of H_{SF} can be determined from M versus H plots at locations where a steep increase in the magnetization occurs, followed by quick reduction of the slope. Spin-flop transitions will only be observed when a component of the applied field lies along an easy axis. In Eq. 4.6, $\chi_{\perp}$ and $\chi_{\parallel}$ are the values of the magnetic susceptibility determined from VSM measurements obtained at the lowest measured temperatures. With these two quantities and H_{SF}, we can easily approximate the anisotropy energy K. This analysis serves only as a guide, however; as the critical field has a slight temperature dependence due, in part, to the increase of $\chi_{\parallel}(T)$ below T_N. For this reason, M versus H plots are usually measured at the lowest temperature allowed by the experimental setup, where the magnetic order is most stable against thermal vibrations.

4.3.1 $CuSb_2O_6$

The field dependence of the magnetization of $CuSb_2O_6$ at 3 K is shown in Fig. 4.6. A spin-flop transition where the spins turn from parallel orientation to a perpendicular orientation, and thereby lowering their energy, is observed around 1.25(5) T for the a- and b-axes but not the c-axis. This provides further evidence that the magnetic

moments are constrained to the a-b plane. The larger jump in the data when $H \parallel [010]$ compared to when $H \parallel [100]$ indicates the moments are aligned more with the b-axis than the a-axis. The anisotropy observed between the a- and b-axes is likely a result of the monoclinic distortion that occurs below 380 K [88].

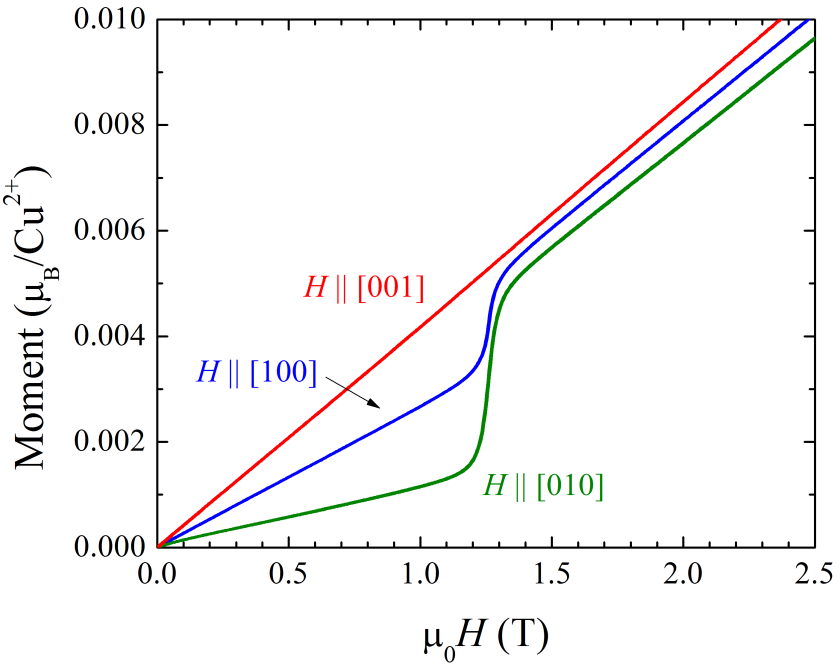

Figure 4.6: Magnetic field dependence of the magnetization of $CuSb_2O_6$ at 3 K.

The spin-flop transition has been observed to occur at lower fields for lower temperatures [9]. This means that the spin-flop configuration is more energetically favorable (lower in energy) than the antiferromagnetic state. This is due to the lowering of total energy of the spin-flop configuration compared to the antiferromagnetic state with increasing anisotropy and coupling strength as temperature decreases [9]. In other words, at lower temperatures where vibrational energy is less and the antiferromagnetic state is more established, magnetic fields can more easily dominate over spin coupling. At higher temperatures, but still below T_N, higher magnetic fields (by

about 5 percent) are required to induce a spin-flop [9]. This is because at higher temperatures, m_z, being the component of the magnetization parallel to the external field, decreases (due to precession) for spin cones whose axis is parallel to the field. Therefore a higher field is necessary in order for the $-m_z \cdot B$ term to overcome the anisotropy term. Increasing temperature up to T_N will also increase magnetization due to thermal vibrations which assist in the canting of the spins in a magnetic field.

4.3.2 $Ni(Sb,Ta)_2O_6$

The magnetization versus field for $NiSb_2O_6$ up to 9 T at 2 K is shown in Fig. 4.7a. A spin-flop transition is observed at $\mu_0 H_{SF} = 8.125(5)$ T when the applied field is along either [110] or $[1\bar{1}0]$, i.e. when field is applied along the moments of a sublattice. No spin-flop transition is observed for $0 < \mu_0 H < 9$ T applied along [100], [010], or [001]. Instead, a quadratic increase of the magnetization with respect to H is observed. The fact that the increase is nonlinear may be due to a small percentage of moments reorienting to the spin-flop configuration even when $H < H_{SF}$. The resulting rise in magnetization increases the effective magnetic field strength felt by other moments, in addition to the external field driving the initial alignment, thereby further increasing the magnetization.

Magnetization versus applied field for $NiTa_2O_6$ is shown in Fig. 4.7b. No spin-flop transition is observed for applied fields up to 9 T. The slope of $M(H)$ for $H \perp [001]$ is comparable to the analogous curves for $NiSb_2O_6$. However, the slope for $H \parallel [001]$ is almost two times greater for $NiTa_2O_6$. This is reflected in the fact that T_N occurs closer to the peak of the broad susceptibility maximum in $NiTa_2O_6$ than in $NiSb_2O_6$ (see Fig. 4.2). Therefore, at low temperature $\chi_\perp$ (and, in turn, the magnetization) is able to saturate to a value much larger than $\chi_\perp$ of the analogous antimonate.

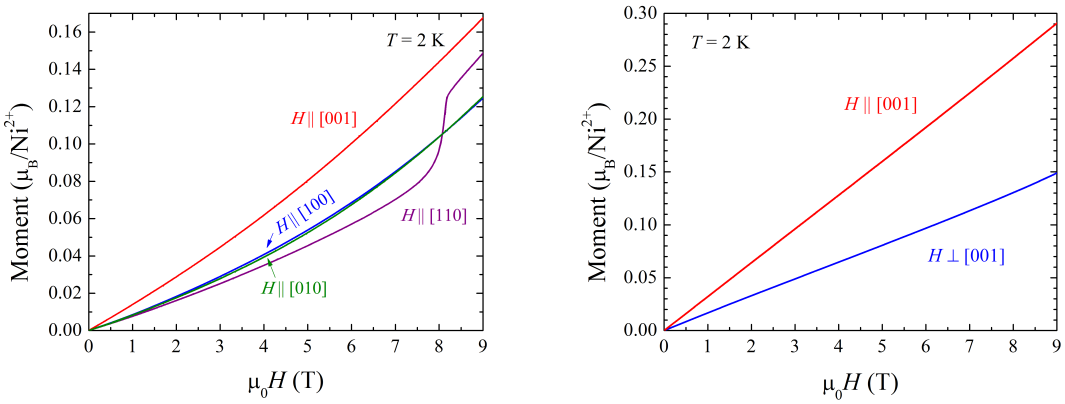

(a) $NiSb_2O_6$ (b) $NiTa_2O_6$

Figure 4.7: (a) Magnetic moment versus magnetic field of $NiSb_2O_6$ at $T = 2$ K. A spin-flop occurs at $H_{SF} = 8.125$ T for field applied along [110] or [1$\bar{1}$0]. (b) Magnetic moment versus magnetic field for $NiTa_2O_6$ at $T = 2$ K. No spin-flop transition is observed for applied fields up to 9 T.

The higher spin-flop field value in the case of $NiTa_2O_6$ strongly suggests that the anisotropy energy is larger.

The magnetization of a powder sample of $NiTa_2O_6$ has been measured by Law *et al.* [14] in fields up to 60 T using a pulse-field magnetometer. They observed an inflection in the $M(H)$ data at 12.80(5) T which broadens with increasing temperature. Above T_N, the feature disappears and the data for subsequent measurements at higher temperature become identical. This feature thus has the behavior of a spin-flop transition and its value will be of great use in later sections.

4.3.3 $Co(Sb,Ta)_2O_6$

Magnetization was measured for $CoSb_2O_6$ from 0 to 9 T at 3 K (see Fig. 4.8)a. The data reveal a linear trend for $H \parallel [001]$. Magnetization for $H \perp [001]$ was measured for field applied along the [100], [010], and [110] crystallographic directions.

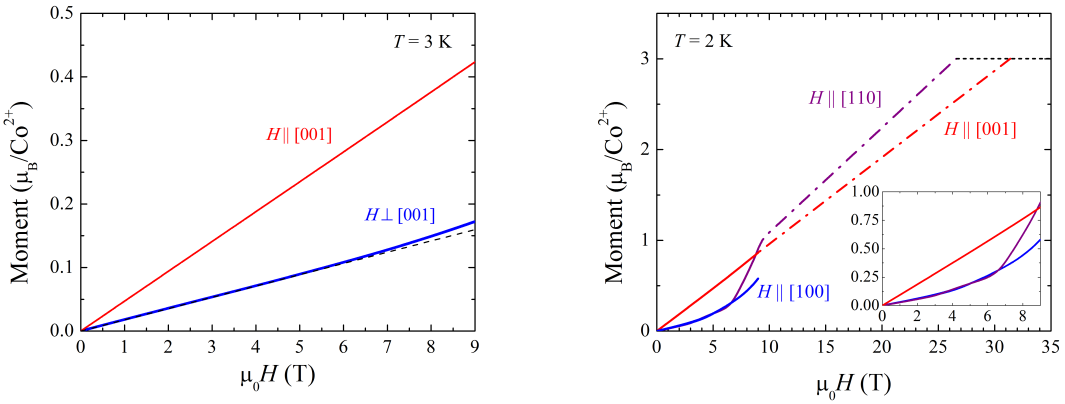

(a) $CoSb_2O_6$ (b) $CoTa_2O_6$

Figure 4.8: (a) Magnetic moment versus magnetic field of $CoSb_2O_6$ at $T = 3$ K. The c-axis is linear while the a-axis deviates slightly from linearity (shown by the dashed line) near 6.5 T. (b) Magnetic moment versus magnetic field for $CoTa_2O_6$ at $T = 2$ K. A spin-flop transition is observed near 8.0(5) T for $H \parallel [110]$. Curves for $H \parallel [100]$ and $H \parallel [010]$ are identical.

The data lie directly on top of one another, with only minor discrepancies that can be attributed to misalignment of the sample on the sample holder. A minor deviation from linearity beginning above $\sim$ 6.5 T for $H \perp [001]$ is observed which is likely caused by the reorienting or spins in anticipation of a spin-flop at a field just above 9 T. Unfortunately the PPMS cannot apply fields high enough to investigate this region. To the best of my knowledge, no value for H_{SF} has been determined for $CoSb_2O_6$ to confirm this presumed spin-flop.

M versus H data for $CoTa_2O_6$ is shown in Fig. 4.8b. No spin-flop transition is observed for H applied along the c-axis, suggesting there are no moments with a component along [001] in the ordered state. This is contrary to the magnetic structure proposed by Reimers [29] but agrees with the two-sublattice model proposed by Kinast *et al* [31, 32]. The curves for $H \parallel [100]$ and $H \parallel [010]$ are identical and show a slight non-linear increase with field. For $H \parallel [110]$, a minor change in slope occurs near 2.8 T

and a more prominent spin-flop transition is signified by the kink near $\mu_0 H = 7.1(1)$. At a field strength significantly higher than H_{SF}, all the moments within the sample would fully align. Applying additional field strength with the moments in the fully aligned configuration would have no effect on the magnetization, which is said to be saturated at that constant value M_{sat}. The current laboratory setup is unable to achieve fields high enough to observe this phenomenon. However, if all the moments were aligned with the applied field, we would therefore observe that $M_{sat}/N \approx n\mu_{\mathrm{B}}$, where N is the total number of spins and n is the number of unpaired electrons per magnetic ion. (Note that $n\mu_{\mathrm{B}}$ is *not* the effective moment obtained from the Curie constant.) When an anisotropy field, H_A, is present in the crystal lattice, the field at which the magnetization saturates will be either higher or lower depending upon if the external field is applied parallel or perpendicular to the c-axis, respectively. The anisotropy field is defined as the sum of internal factors that contribute to the deviation from an ideal isotropic system. These factors include single-ion (crystal-field) anisotropy and dipole-dipole interactions. The critical fields for the saturated phase will differ from twice the exchange field H_E by $\pm H_A$. We can therefore write the well-known linear relations

$$\frac{M_{[110]}}{H} = \frac{M_{sat}}{2H_E - H_A} \tag{4.7}$$

$$\frac{M_{[001]}}{H} = \frac{M_{sat}}{2H_E + H_A}. \tag{4.8}$$

The left sides of Eqs. 4.7 and 4.8 can be approximated using the slopes of extrapolated M versus H curves above H_{SF}. The value of M_{sat} is taken to be $3\mu_{\mathrm{B}}$. The above analysis leads to $\mu_0 H_A = 1.76$ T and $\mu_0 H_E = 14.8$ T for $CoTa_2O_6$. As an affirmation of these results, the values of the exchange and anisotropy fields can be used to predict the spin-flop transition through the relation [47]

$$H_{SF} = \sqrt{2H_E H_A - H_A^2}. \tag{4.9}$$

This analysis leads to $\mu_0 H_{SF} = 7.0$ T, in good agreement with the observations of Fig. 4.8b.

4.3.4 $FeTa_2O_6$

Magnetization of $FeTa_2O_6$ versus applied field was measured at 2 K and the results are shown in Fig. 4.9. No deviation from linearity is observed for $H \parallel [001]$. For measurements with $H \parallel [110]$, a minor change in slope occurs near 3.5 T while a clear spin-flop transition occurs at 7.07(9) T. The former feature is likely due to the canting of moments perpendicular to the field. This feature was also observed by Chung *et al* who noted that the behavior of the spin-flop does not seem to be affected by the field induced by the canted moments [89]. This would indicate that the coupling between the two sublattices is likely to be weak, as expected for low-dimensional compounds.

Following the procedure of the previous section, the $M(H)$ curves are extrapolated above 9 T up to the saturated magnetization value, $M_{sat}/N = 4\mu_B$. (The variation in slope of the $H \parallel [110]$ curve above and below the spin-flop field is a clear indication that only the set of moments which are perpendicular to the applied field are participating in the magnetization at lower fields. The larger slope above the spin-flop transition indicates that *both* sets of moments participate.) The slopes of the two extrapolated curves have been used in Eqs. 4.7, 4.8, and 4.9 to determine $\mu_0 H_A = 1.89$ T, $\mu_0 H_E = 8.64$ T, and $\mu_0 H_{SF} = 5.4$ T. The calculated value of the spin-flop field is about midway between the two changes in slope observed in $M(H)$. The anisotropy field is comparable to that observed in $CoTa_2O_6$, whereas the exchange field is about half that of the cobalt compound.

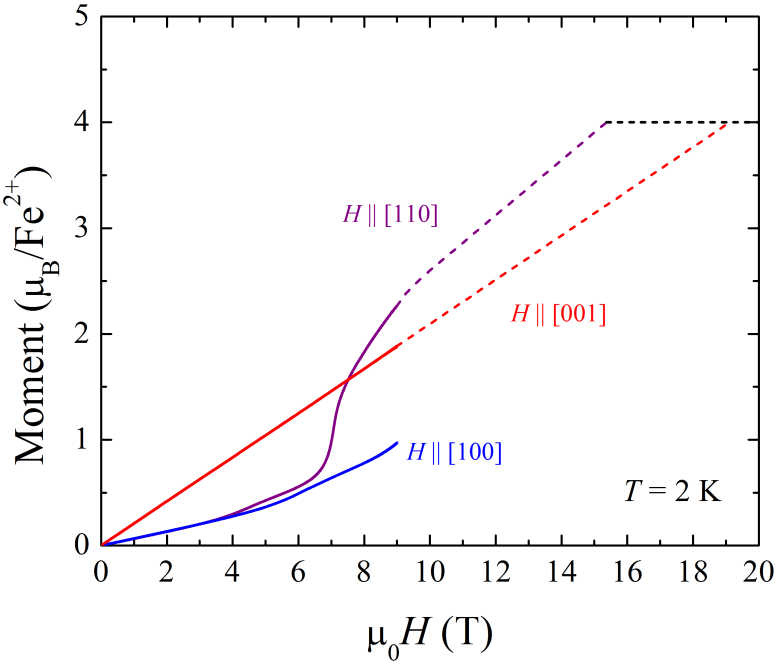

Figure 4.9: Magnetic field dependence of the magnetization of $FeTa_2O_6$ at $T = 2$ K. A spin-flop transition is observed near $\mu_0 H = 7$ T for fields parallel to [110].

4.3.5 $MnSb_2O_6$

The field dependence of the magnetization of $MnSb_2O_6$ at 2 K is shown in Fig. 4.10. Unlike the other compounds previously measured, $MnSb_2O_6$ shows a spin-flop transition when a field $\mu_0 H_{SF} = 0.94$ T is applied *parallel* to the c-axis. This difference is due to its trigonal crystal structure as well as the chiral magnetic structure containing moments that rotate in planes which contain the c-axis [33]. No spin-flop is observed for fields applied perpendicular to [001]. The magnetization above and below H_{SF} is very linear, indicating the usual gradual canting of the moments with field. A similar measurement conducted on a powder sample has been done previously by Werner *et al.* [90] using a pulsed field up to 30 T. They observed the magnetization saturate to $4.9\mu_B/Mn^{2+}$ at 25.3 T, implying $\mu_0 H_E = 12.7$ T. The saturation value is similar

to $4.6\mu_B$ determined by Reimers *et al.* [34] by applying an $S = \frac{5}{2}$ Brillouin function fit to the magnetic moment data and extrapolating to zero kelvin. The reduction in effective moment from the commonly measured value for Mn^{2+} was ascribed to quantum spin fluctuations.

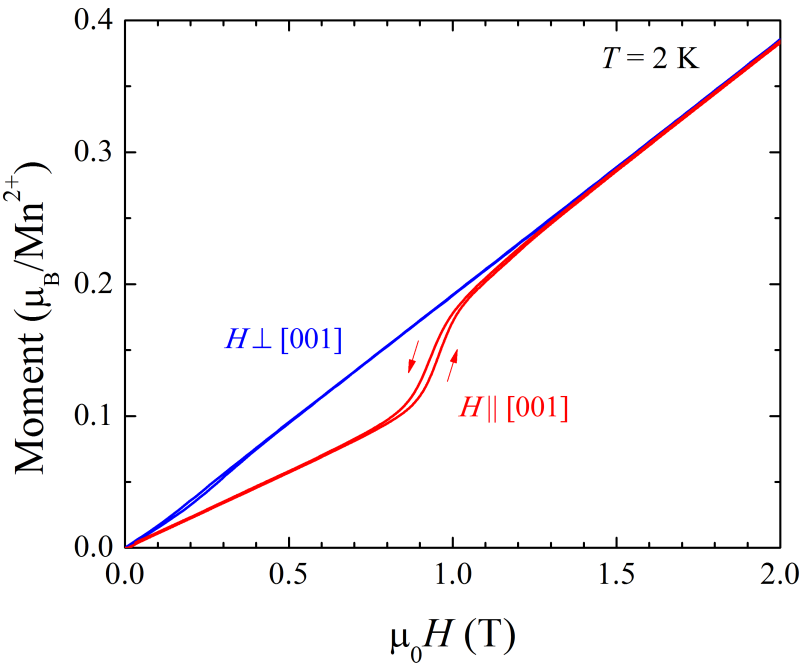

Figure 4.10: Magnetic field dependence of the magnetization of $MnSb_2O_6$ at $T = 2$ K. A spin-flop transition is observed near $\mu_0 H = 0.94$ T for fields parallel to [001].

A very narrow hysteresis loop is associated with the spin-flop transition in Fig. 4.10. This loop could not be observed in Werner's data using a polycrystalline sample. Upon increasing H, the antiferromagnetic phase remains stable up to a field value $\mu_0 H_1 \approx 0.95$ T, beyond which the system switches to the spin-flop configuration. If the system starts in the spin-flop phase and the field is then decreased, this phase will remain stable down to a field $\mu_0 H_2 \approx 0.93$ T below which the antiferromagnetic phase is recovered. The critical field H_{SF} at which both phases have the same energy

is intermediate between H_1 and H_2. Similar hysteresis loops have been observed in other antiferromagnetic compounds in which a small degree of inhomogeneity was the suspected cause [91, 92]. In the references cited, it is discussed that such inhomogeneities may act as supposed pinning centers for spin-flop states on the surface. These sites might then stall, or halt, their progression inside the bulk of the sample. The phases may therefore be sustained within fields beyond the thermodynamic transition.

With the use of Eq. 4.9, estimated values for the exchange field H_E and single-ion-anisotropy field H_A for samples measured at $T = 0$ K can be found through the use of the following relation [93, 94, 95]

$$\frac{H_2}{H_1} = \frac{2H_E - H_A}{2H_E + H_A}. \tag{4.10}$$

Applying the above relations to the data from Fig. 4.10 results in $\mu_0 H_E = 4.58$ T and $\mu_0 H_A = 0.097$ T. The value of the exchange field is less than half of the value suggested by Werner's measurement. However, minor changes in H_1 and H_2 can greatly affect the calculated values of H_E and H_A. Presumably, the discrepancy in H_E is due to the fact that the data used in Eq. 4.10 was taken at 2 K rather than $T = 0$ K for which the equation was derived. Assuming the value $\mu_0 H_E = 12.7$ T from Werner's measurement, the anisotropy field is reevaluated to be $\mu_0 H_A = 0.035$ T. This value agrees with that of Werner *et al.* calculated using antiferromagnetic resonance data [90] and is within the range 0.01-0.09 T typical for Mn^{2+} ions [96].

A more subtle hysteresis loop can be noticed around $\mu_0 H = 0.2$ T applied perpendicular to the c-axis. The presence of this loop is likely a result of the $\sim 13^\circ$ tilt of the spin-spiral plane away from the c-axis suggested by Kinoshita *et al.* [35]. The fact that it is observed at lower fields is explained by noting that m_z, the component of the magnetic moment parallel to the field, is much smaller in this configuration.

Therefore a much smaller applied field, $\mu_0 H_{SF} \sin(13^\circ) = 0.21$ T, is required to induce a spin-flop.

4.4 Discussion

This chapter has shown magnetization data of $M(\mathrm{Sb,Ta})_2\mathrm{O}_6$ single crystals with field applied along various crystallographic axes. With the exception of the trigonal $\mathrm{MnSb_2O_6}$, all compounds investigated here show a broad peak in $\chi(T)$ regardless of the direction of the applied field. As mentioned previously, this indicates a deviation from the Curie-Weiss law that describes paramagnetism and demonstrates the onset of short-range antiferromagetic order. All compounds undergo a transition to long-range antiferromagnetic order indicated by a change in slope at temperatures below that of the broad maximum. For samples with tetragonal crystal structures, the $\chi(T)$ data obtained in low fields with $H \perp [001]$ are identical within experimental uncertainty. However, spin-flop transitions occur when the applied field is parallel to either [110] or $[1\bar{1}0]$, indicating that there exist sets of magnetic moments parallel to either of these directions. Additional information concerning the arrangement of the moments with respect to each other, such as the arrangement along principle axes, cannot be determined precisely with these measurements alone. More thorough investigations using neutron diffraction on single-crystalline samples are necessary. However, the two-sublattice model described in Section 1.3 is a likely candidate for $\mathrm{Ni(Sb,Ta)_2O_6}$ and $\mathrm{CoSb_2O_6}$.

The magnetic susceptibility versus temperature for each compound has been fitted using expressions describing either Heisenberg or Ising type interactions. It has been shown that $\mathrm{Co(Sb,Ta)_2O_6}$ and $\mathrm{FeTa_2O_6}$ can be fit well using Ising models. This

Table 4.3: The table shows relevant parameters used to calculate the coupling constants via the relations provided in Table 3.3.

Compound	C	T_N	T_{max}	χ_{max}	$\lvert J\rvert/k_B$	$\frac{\chi_{max}T_{max}}{C}$
	[cm^3 K/mol]	[K]	[K]	[cm^3/mol]	[K]	–
$CuSb_2O_6$	0.6271	8.7(1)	61.8	0.003057	32.6	0.301
$NiSb_2O_6$	1.3491	6.7(1)	34.2	0.013459	7.77	0.341
$NiTa_2O_6$	1.3595	10.5(1)	25.5	0.018939	5.80	0.355
$CoSb_2O_6$	2.6595	13.5(1)	35.0	0.033921	4.44	0.446
$CoTa_2O_6$	2.7952	6.2(1)	16.9	0.050812	2.15	0.307
$FeTa_2O_6$	3.1320	8.2(1)	15.3	0.099376	1.23	0.485
$MnSb_2O_6$	4.3752	11.9(1)	12.6	0.107027	0.70	0.308

comes as little surprise since Co^{2+} and Fe^{2+} ions are well known to be Ising ions [13, 71, 89]. The remaining compounds were successfully fit using Heisenberg models. Models employed in this investigation used appropriate spin values and spin degrees of freedom where necessary, rather than the generic "infinite spin" model [72]. The values of the exchange coupling determined from these fits is correlated to the temperature of the broad peak maxima which decreases with increasing magnetic moment. That is to say, when the exchange coupling in large, as in the case of $CuSb_2O_6$, the clusters of moments are able to antiferromagnetially align at higher temperature than compounds with weaker exchange coupling. Thus the susceptibility begins to deviate sooner from Curie-Weiss behavior upon cooling.

The values of the Curie-Weiss constant and height of the broad peak in χ, along with their ratios, can be compared against those expected for the Heisenberg model using a spin-wave theory as discussed in Section 3.1.4. Parameters used here are those taken from measurements with $H \perp [001]$. The exchange constants given in Table 4.3

have been calculated using the ratios provided by Table 3.3. The values vary greatly from those determined by fitting theoretical expressions to the $\chi(T)$ data and are meant to serve only as guides. The ratio $\frac{\chi_{max}T_{max}}{C} \approx 0.34$ is used as a determination of the validity of the Heisenberg model [75]. In general, the values are similar to the theoretical quantity; those from the nickel compounds coming closest, meaning the Heisenberg model is a good representation of the magnetic interactions. It comes as no surprise that the largest deviation from this value occurs in the suspected Ising compounds, $CoSb_2O_6$ and $FeTa_2O_6$.

A partial summary of the results from this chapter is provided in Table 4.4. Values for $\mu_0 H_E$, $\mu_0 H_A$, and K can only be obtained from the earlier analysis if $\mu_0 H_{SF}$ is known. Despite this value being known for $CuSb_2O_6$ and $NiSb_2O_6$, the largest magnetization recorded at 9 T is too small of a fraction of M_{sat} [i.e. the slope of $M(H)$ is too small] to reliably calculate the saturation fields, and in turn the exchange and anisotropy fields. For example, given the value $M_{sat}/N = 2\mu_B$ and the slope of the $H \parallel [110]$ curve above H_{SF} for $NiSb_2O_6$, the value of the saturation field for the easy axis is about 78 Tesla! Furthermore, due to the non-linearity of the $H \parallel [001]$ curve, the hard axis saturation field is very difficult to extrapolate. These issues make the determination of H_A and H_E very problematic. However, knowledge of the spin-flop field can still be used to approximate the anisotropy energy, K, through the use of Eq. 4.6. The values for $\chi_\perp$ and $\chi_\parallel$ at the lowest measured temperature are gathered from the plots of magnetic susceptibility in Section 4.2. The results for K are provided in the right-most column of Table 4.4. Excluding the trigonal compound, $MnSb_2O_6$, the values of K increase (non-linearly) with increasing magnetic moment and decreasing exchange coupling. Interestingly, $NiSb_2O_6$, $CoTa_2O_6$, and $FeTa_2O_6$ all show spin-flop transitions near the same field strength. Since H_{SF} is comparable in each case, the anisotropy energy given by Eq. 4.6 is dictated mainly by the magnitude

Table 4.4: Results from magnetic susceptibility and spin-flop investigations. Parameters are the exchange coupling, measured spin-flop field, exchange field, anisotropy field, and anisotropy energy, respectively. †The value of $\mu_0 H_{SF}$ for $NiTa_2O_6$ was determined by Law *et al.* [14] from a powder sample.

Compound	$\lvert J\rvert/k_B$ [K]	$\mu_0 H_{SF}$ [T]	$\mu_0 H_E$ [T]	$\mu_0 H_A$ [T]	K [μeV/ion]
$CuSb_2O_6$	97.1(4)	1.25(5)	–	–	0.135
$NiSb_2O_6$	26.0(1)	8.125(5)	–	–	12.3
$NiTa_2O_6$	18.92(2)	12.80(5)†	–	–	69.9
$CoSb_2O_6$	10.603(6)	–	–	–	–
$CoTa_2O_6$	6.1(2)	7.0(5)	14.8	1.76	95.8
$FeTa_2O_6$	2.888(6)	7.07(9)	8.64	1.89	206
$MnSb_2O_6$	2.478(2)	0.94(6)	12.7	0.035	1.05

of the moments via $\chi_\perp$. That is to say, since $\chi_\parallel$ tends toward zero below T_N, the compounds with the largest value of K are also those with the largest value of $\chi_\perp$.

Interestingly, the coupling constants determined from fits to the magnetic susceptibility and arranged in Table 4.4 are all about 3 times larger than those in Table 4.3 calculated from spin-wave theory, but otherwise follow the same trend. In general, the magnitude of the exchange coupling depends on the magnitude of the magnetic moments of the transition metals, the metal-oxygen orbital overlap, and the M-O-O-M bond angle. Since the crystal structures of the trirutiles are very similar, the bond angle should not vary much between each compound, leaving a combination of the other two parameters to determine the value of J. In Fig. 4.11, the value of the exchange coupling is plotted against the ionic radius, R_{ion}, of the transition metals divided by the M-O separation, $D_{M\text{-O}}$. This ratio serves as an indication of the amount of orbital overlap between ions. Values of R_{ion} are provided by Shan-

non [97]; lattice parameters are provided in the tables of the Appendix. The exchange coupling is observed increase exponentially, i.e. $J/k_B \sim Ae^{BR_{ion}/D_{M\text{-}O}}$, where A and B are fitting parameters. Therefore, compounds with larger orbital overlap have a larger exchange coupling, which is highly sensitive to the amount of that overlap. This is in qualitative agreement with Whangbo *et al.* [24]. Furthermore, it is observed here that the strength of the coupling is, in general, inversely related to the spin of the transition metal ion. An increase in the number of unpaired electrons seems to therefore hinder the value of J/k_B.

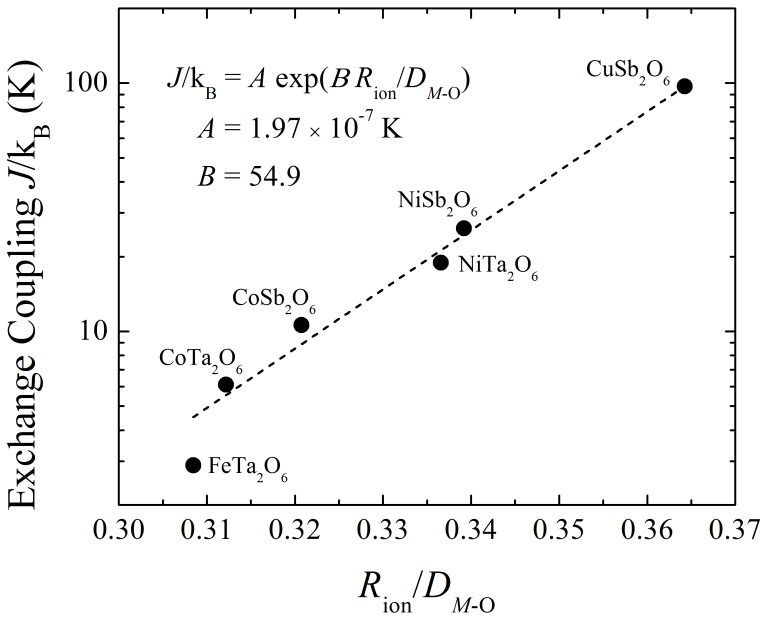

Figure 4.11: Semi-log plot of the exchange coupling versus the ratio of the ionic radius to M-O separation, $R_{ion}/D_{M\text{-}O}$. The dotted line is fit using the phenomenological equation $J/k_B \sim Ae^{BR_{ion}/D_{M\text{-}O}}$. Values of A and B are provided in the figure.

5. HEAT CAPACITY

5.1 Introduction

The heat capacity, C, of a material is the proportionality constant between the heat that the material absorbs or loses and the resulting temperature change. However, despite the word "constant," this quantity can vary with temperature and pressure, especially near phase transitions when there is a sizable change in entropy. Heat capacity can provide valuable information about a material's lattice, electronic, and magnetic properties. When taken below the Debye temperature, measurements directly probe the electronic and magnetic energy levels. Such knowledge is important to the understanding of the material's magnetic structure and its behavior with changing temperature and magnetic field.

In the current study, heat capacity was measured using a heat-capacity puck [98] which consists of a copper frame from which eight delicate platinum wires suspend a 3×3 mm^2 alumina platform. Samples were mechanically and thermally coupled to the platform using Apiezon thermal grease. (The heat capacity of the Apiezon grease was measured prior to mounting the sample and later subtracted from the sample/grease data.) The underside of the platform contains a small heater and thermometer which are fed currents through the small platinum wires. A copper cap was placed over the calorimeter puck to serve as a radiation shield that thermally isolates the sample from stray heat sources.

A thermal-relaxation technique was employed to measure heat capacity at constant pressure, C_P, between 1.9 and 300 K. A small current between a few nanoamps and a few milliamps is sent through the platinum leads for a short time t_0 to activate

the heater. A constant power P_0 is supplied during this time which raises the sample temperature to $T_0 \equiv T_b + \Delta T$, where T_b is the temperature of the thermal bath (i.e. the sample puck). When the power is shut off after t_0, the sample temperature decays towards T_b. Because the measurement is done at high vacuum (around 0.01 mTorr), the conductive cooling via exchange gas is negligible. Instead, the thermal conduction between the sample platform and the puck is dominated by the bridging platinum wires. This process is repeated multiple times at each measured temperature. A value for C_P is determined by fitting the time-dependent decay of the sample temperature with one of two models. The first model uses a single decay constant in situations where coupling between the sample and platform is close to 100%. The second utilizes two decay constants when coupling is between 90% and 98%.

In the first model, the temperature T of the sample/grease/platform system as a function of time t obeys the differential equation

$$C_{total}\frac{\mathrm{d}T}{\mathrm{d}t} = -K_w(T - T_b) + P(t), \qquad P(t) = \begin{cases} P_0 & 0 \le t \le t_0 \\ 0 & t > t_0 \end{cases}, \tag{5.1}$$

where K_w is the thermal conductance of the platinum wires. The solution to Eq. 5.1 can be obtained by integration, resulting in

$$T(t) = \frac{P_0}{K_w}\left(1 - \mathrm{e}^{-\frac{K_w}{C_{total}}t}\right) + T_b, \qquad 0 \le t \le t_0 \tag{5.2a}$$

$$T(t) = (T_0 - T_b)\mathrm{e}^{-\frac{K_w}{C_{total}}(t-t_0)} + T_b, \qquad t > t_0, \tag{5.2b}$$

where $T_0 = T(t_0)$ is highest temperature reached during the pulse before the current is turned off. Note that a natural time constant $\tau = C_{total}/K_w$ forms in Eqs. 5.2a and 5.2b. The value of C_{total} can be extracted from the temperature decay curve ($t > t_0$) using a non-linear least squares fitting algorithm. The heat capacity of the sample is

found by subtracting $C_{addenda}$, which is measured prior to mounting the sample, from C_{total}.

The second model, aptly named the Two-Tau Model$^{\text{TM}}$, is used when the coupling between the sample and platform is poor (i.e. when poor thermal attachment of the sample to the platform results in a temperature difference between the two). The two-tau model accounts for heat flowing between the sample and sample platform, and between sample platform and puck. This can be represented mathematically through the expressions

$$C_{platform}\frac{\mathrm{d}T_p}{\mathrm{d}t} = P(t) - K_w\big(T_p(t) - T_b\big) + K_g\big(T_s(t) - T_p(t)\big), \tag{5.3}$$

$$C_{sample}\frac{\mathrm{d}T_s}{\mathrm{d}t} = -K_g\big(T_s(t) - T_p(t)\big), \tag{5.4}$$

where K_g is the thermal conductance between the sample and platform due to the grease. The respective temperatures of the sample and platform as a function of time are given by $T_s(t)$ and $T_p(t)$. Note that in the limit as $T_s \to T_p$, we recover Eq. 5.1. The solutions to Eqs. 5.3 and 5.4 take the simple form $T_x(t) = A_x + B_x\mathrm{e}^{-t/\tau_1} + D_x\mathrm{e}^{-t/\tau_2}$ where x designates either the sample or the platform and A_x, B_x, and D_x are inconsequential constants. The time constants are rather complicated, taking the form [98] $\tau_1 = 1/(\alpha+\beta)$ and $\tau_2 = 1/(\alpha-\beta)$, where α and β are given by

$$\alpha = \frac{K_w}{2C_{plat}} + \frac{K_g}{2C_{plat}} + \frac{K_g}{2C_{samp}}, \tag{5.5a}$$

$$\beta = \frac{\sqrt{K_g^2(C_{samp}+C_{plat})^2 + K_gK_wC_{samp}(2C_{samp}-C_{plat}) + K_w^2C_{samp}^2}}{2C_{samp}C_{plat}}. \tag{5.5b}$$

The software that runs the measurement fits the data using both Eq. 5.1 and the two tau model. It then selects the result that provides the best fit. Generally, when the sample coupling defined by $100 \times K_g/(K_g+K_w)\%$ is around 99% or less, the two tau

model is chosen. Alternatively, when the coupling is close to 100%, the first model is typically preferred.

Once the specific heat is experimentally determined, we can apply theory to obtain useful information about the magnetic states. At low temperature, the specific heat is often modeled using the polynomial

$$C = \gamma T + \beta_3 T^3 + \beta_5 T^5 \tag{5.6}$$

The first term is the Sommerfeld electron contribution which increases with the number of conduction electrons. The last two terms are the lattice (or phonon) contribution, i.e. the Debye T^3 Law with a higher-order correction. Typically β_5 is small and usually neglected. The coefficients are given by [99]

$$\gamma = \frac{\pi^2 N_A k_B^2}{2E_F}, \quad \text{and} \quad \beta_3 = \frac{12\pi^4 N_A k_B}{5\Theta_D^3}, \tag{5.7}$$

where E_F is the Fermi energy and Θ_D is the Debye temperature. The Fermi energy is inversely proportional to the effective mass of the conduction electrons, which is governed by the interactions with ion cores, phonons, and other electrons. Therefore γ depends not only on the number of conduction electrons, but also on their effective mass.

The coefficients can be obtained by applying Eq. 5.6 to C_P at low temperature but above T_N. The Debye temperature can then be determined using $\Theta_D \equiv [(12\pi^4 NR)/(5\beta_3)]^{1/3}$ where N equals the number of atoms per chemical formula unit and R is the ideal gas constant, $N_A k_B$. Qualitatively, Θ_D can be interpreted as the temperature needed to activate all of the phonon modes in a crystal. This temperature can also be expressed as $\hbar\omega_D/k_B$, where ω_D is the Debye frequency. A low value of Θ_D means a low ω_D, which leads to weak interatomic bonds. Therefore a large Θ_D means the crystal is stiffer than others with a lower value.

5.2 Specific Heat of $M(\mathrm{Sb,Ta})_2\mathrm{O}_6$

The heat capacity of various $M(\mathrm{Sb,Ta})_2\mathrm{O}_6$ compounds was measured at constant pressure in zero field and then normalized to the samples' molar amount. The data are shown in Fig. 5.1. Data acquired from the two nonmagnetic analogs $\mathrm{ZnSb_2O_6}$ (grey circles) and $\mathrm{MgTa_2O_6}$ (grey squares) are also provided in each figure. In general, the tantalates (plotted in red) have a larger specific heat due to the larger mass of the tantalum atoms. A sharp peak is observed for each magnetic compound which indicates the onset of long-range antiferromagnetic order at T_N. These features coincide with the changes in slope observed in magnetic susceptibility. The deviation between the magnetic and nonmagnetic data above T_N is due to the presence of short-range magnetic order.

Data from the nonmagnetic analogs have been subtracted from the C_P data of the magnetic samples, leaving the magnetic contribution of the specific heat δC_P. The data for each compound have been normalized to the height and position of the broad peak and are shown in Fig. 5.2. Recall from Section 3.2.2 that systems with multiple energy levels separated by a gap Δ will display a broad maximum in magnetic heat capacity data near $T_{max} = 0.42\Delta$ due to an increase in probability of transitions to an excited state. The general shape of the broad peak in δC_P for each compound are in agreement after normalization, suggesting that the mechanism driving short-range order is similar. Data for $\mathrm{MnSb_2O_6}$ is not included in this plot since very little magnetic contribution remains above T_N. Normalization to a broad peak is therefore indeterminable. The shortage of magnetic heat capacity above T_N should come as no surprise since there is little indication of short-range order suggested by magnetic susceptibility measurements (see Fig. 4.5a).

Looking carefully at Fig. 5.2, we notice that the separation between the sharp peaks that indicate long-range order and the peak of the normalized broad maximum decreases as the spin value increases. Furthermore, this separation is much smaller for the tantalates than for the antimonates. Short-range order therefore seems to be more prevalent in the antimonate compounds with lower spin values. This assessment is similar to the observations of Fig. 4.11 in which the exchange coupling is seen to increase for compounds with lower quantum spin number. The exchange coupling is roughly determined by the location of the broad maximum in magnetic susceptibility. Compounds with a larger coupling therefore display their peaks at higher temperature. The location of this broad peak in χ is related to the broad peak in magnetic heat capacity, as they both are associated with short-range order. In fact, a relationship between the two quantities was derived by Fisher [100] who suggested $(d/dt)(\chi T)$ has the same functional form as the magnetic specific heat δC_P. Normalizing to the broad peak in magnetic specific heat therefore allows us to not only compare the form of the short-range order for multiple compounds, but also get a sense of the relative coupling strength. That is to say, compounds with a greater coupling will show the narrow peaks further removed from the normalized broad maximum.

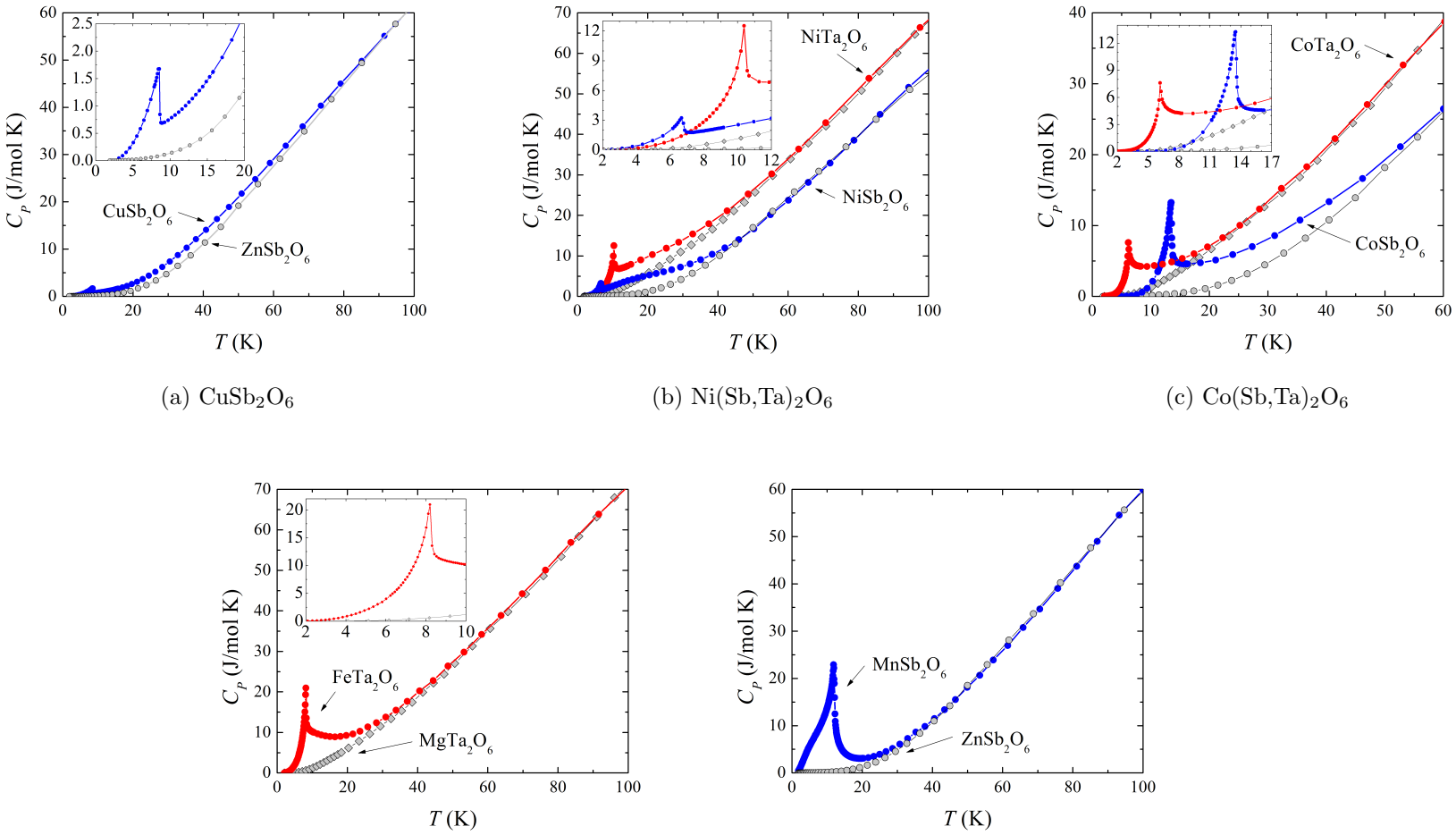

(a) $CuSb_2O_6$ (b) $Ni(Sb,Ta)_2O_6$ (c) $Co(Sb,Ta)_2O_6$

(d) $FeTa_2O_6$ (e) $MnSb_2O_6$

Figure 5.1: Specific heat of $M(Sb,Ta)_2O_6$ compounds. Non-magnetic analogs, $ZnSb_2O_6$ and $MgTa_2O_6$, are denoted by grey circles and diamonds, respectively.

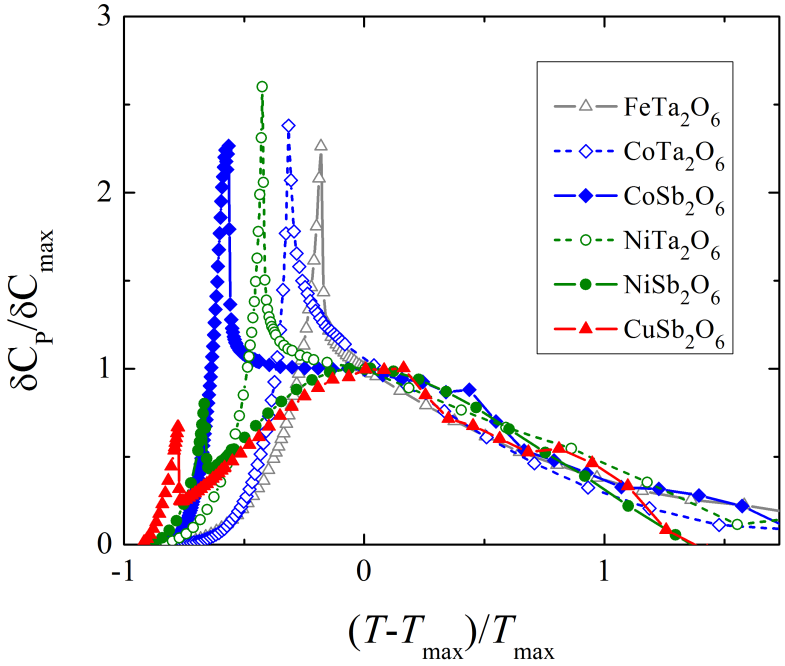

Figure 5.2: Magnetic contribution of $M(\mathrm{Sb,Ta})_2\mathrm{O}_6$ compounds to specific heat normalized by the height (δC_{max}) of the broad peak above T_N, and the temperature T_{max} at which the maximum occurs.

The height of the broad peak in δC_P indicating short-range order is theoretically determined to be $C_{max} = 3.6$ J/mol K for a system with two non-degenerate energy levels (see Section 3.2.2). The experimental height of the peaks are given in Table 5.1. The experimentally determined value of C_{max} for $\mathrm{CuSb_2O_6}$ and $\mathrm{CoTa_2O_6}$ is smaller than the predicted value. This suggests the degeneracy, g_0, of the lower level is larger than the degeneracy, g_1, of the excited state. On the other hand, the larger value of C_{max} for the other compounds suggests $g_1 > g_0$ [76].

The data above T_N have been fit using Eq. 5.6 to determine the Debye temperature as well as γ, of which the latter vanishes below T_N. The results are provided in Table 5.1. Since the samples studied herein are insulators, the γ term cannot be associated with the presence of conduction electrons. It must instead have a purely

magnetic origin. In the case of $CuSb_2O_6$, the disappearance of γ below T_N was attributed to the presence of an energy gap associated with the crossover from partially ordered moments to 3-d long-range order upon cooling [9]. A similar interpretation is made here for the remaining compounds. The values of these gaps are determined later in Section 5.3.

The value of γ for the simple case of the $S = 1/2$ Heisenberg chain was theoretically determined by Johnston *et al.* [55] to be $\gamma = (2/3)Nk_B^2/J$. Using the value of the exchange constant for $CuSb_2O_6$ determined from magnetic susceptibility, we can approximate $\gamma \approx 57$ mJ/mol K^2. The observed γ is remarkably close to the calculated value. Unfortunately, to the best of my knowledge no such approximation exists for $S > 1/2$ to compare against the other observed values.

Table 5.1: Specific heat parameters determined from fits using Eq. 5.6. δC_{max} is the maximum value of the broad peak above T_N observed in the magnetic contribution to the specific heat. T_{max} is the corresponding temperature at which the maximum occurs. Δ is the zero-field splitting discussed in Section 3.2.2.

Compound	Fit range [K]	Θ_D [K]	γ [mJ/mol K^2]	δC_{max} [J/mol K]	T_{max} [K]	Δ [K]
$CuSb_2O_6$	9.26-32.7	442(1)	53.9(7)	2.4(1)	40(3)	95(7)
$NiSb_2O_6$	8.30-10.0	342(2)	209(1)	3.9(1)	20.5(5)	49(1)
$NiTa_2O_6$	32.8-63.0	772(7)	427(3)	4.4(1)	18(2)	43(4)
$CoSb_2O_6$	22.6-43.3	575(2)	208(2)	3.9(1)	28(2)	67(4)
$CoTa_2O_6$	19.7-41.5	501(10)	309(10)	3.1(4)	9(1)	21(3)
$FeTa_2O_6$	28.3-53.2	652(10)	388(5)	9(2)	10(2)	24(4)
$MnSb_2O_6$	25.0-40.6	516(7)	79(5)	–	–	–

5.2.1 Experimental Determination of Magnetic Entropy

The magnetic entropy is an important quantity for determining the amount of ordered and disordered spins in the system. This is applicable for both long-range and short-range order. To determine the change in entropy, it is useful to plot the acquired specific heat data as $\delta C_P/T$ versus temperature. The area under the curve is then ΔS_m as per Eq. 3.22. The magnetic contribution to the specific heat scaled by temperature is shown in Fig. 5.3. The data above T_N for each compound (except $MnSb_2O_6$) display asymmetric peaks with long tails that tend toward zero between 20 K and 100 K indicating the temperature at which short-range order begins upon cooling.

Before we continue the general discussion of entropy, let us take a moment to note that the plot for $MnSb_2O_6$ is markedly different from that of other compounds. The trigonal structure containing a frustrated spin arrangement above T_N is not conducive to short-range order. The data therefore fall rapidly to zero above the peak located at the Néel temperature. Below T_N is an anomalous shoulder near 5 K. This feature in the heat capacity data was also observed, although much less pronounced, by Werner *et al.* [90] measured from a polycrystalline sample. They suggested the feature may be associated with coupling of spin and dielectric degrees of freedom, noting similar specific-heat behavior in the magnetoelectric compound $LiFePO_4$ which is said to be associated with changes of the dielectric function below T_N [90].

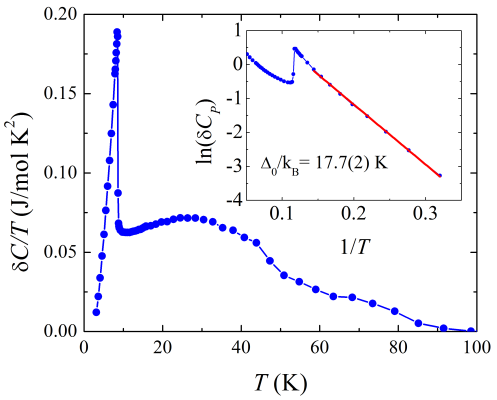

(a) $CuSb_2O_6$

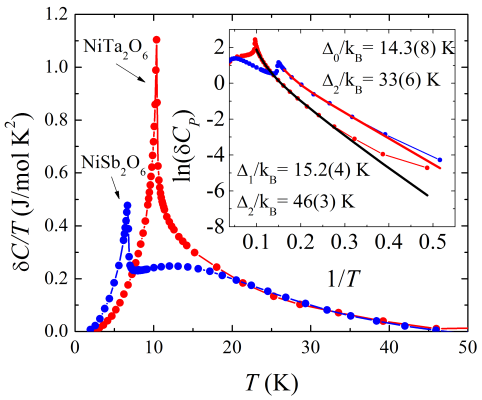

(b) $Ni(Sb,Ta)_2O_6$

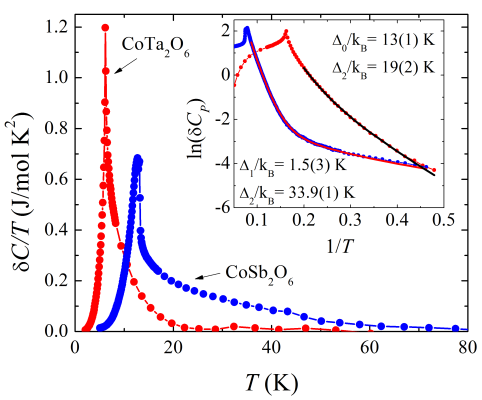

(c) $Co(Sb,Ta)_2O_6$

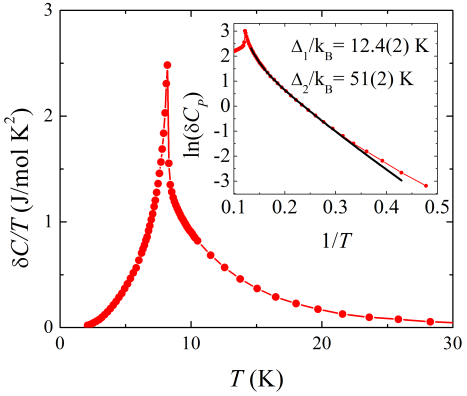

(d) $FeTa_2O_6$

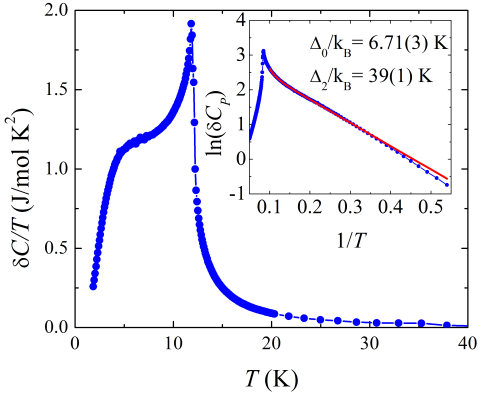

(e) $MnSb_2O_6$

Figure 5.3: Magnetic specific heat scaled by temperature. Insets show the behavior below T_N, plotted for easy extraction of the energy gap.

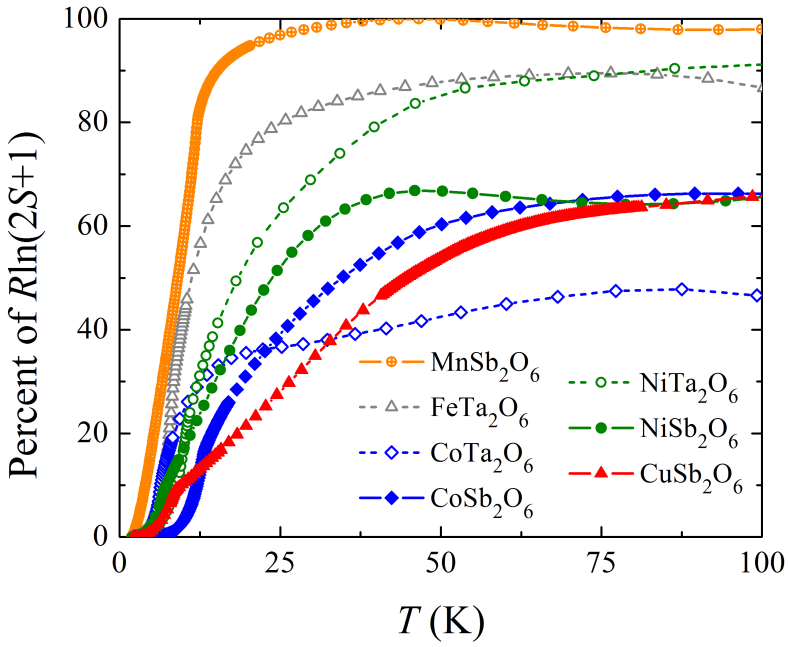

Figure 5.4: Magnetic entropy as a percent of $R\ln(2S+1)$ for $M(\mathrm{Sb,Ta})_2\mathrm{O}_6$.

Returning to the topic of entropy, the $\delta C_P/T$ curves have been integrated with respect to temperature and the results are plotted in Fig. 5.4 as a percentage of $R\ln(2S+1)$, being the theoretical maximum of the magnetic entropy derived in Section 3.2.1. The loss of entropy upon cooling from room temperature to T_N is significant. In multiple cases, over half of the magnetic moments are engaged in local magnetic order *prior* to the onset of long-range magnetic order below T_N. (See Table 5.2 for details). The change in magnetic entropy below T_N accounts for only a small portion of the theoretical maximum. Short-range order is thus a dominant physical property of these systems. Also noteworthy is the fact that the saturation values of the magnetic entropy for all compounds, except $\mathrm{MnSb_2O_6}$, fail to reach the full amount dictated by theory. The difference between the experimental saturation and $R\ln(2S+1)$ reveals the amount of entropy remaining at the lowest measured

temperature (2 K). It is clear that, in general, unordered moments remain even below T_N. For $MnSb_2O_6$, however, the change in entropy reaches the full theoretical amount with the majority of the contribution being below T_N. Long-range order is much more prevalent in this system than in the other compounds measured here.

An additional observation to be made in Fig. 5.4 is the abnormally low percentage of entropy for $CoTa_2O_6$. The data for this compound have been normalized to $R\ln(2S+1)$ assuming a spin state $S = 3/2$ as deduced from magnetic susceptibility measurements (see Section 4.2.3). However, if we assume instead a low-spin state $S = 1/2$ involving a Kramer's doublet ground state $t_{2g}^6 e_g^1$, then the change in entropy saturates to 94%. This would suggest that little disorder remains below T_N. A low-spin state was assumed in a study conducted by Kremer *et al.* [13] who observed a similar saturation value. However, no other reports on $CoTa_2O_6$ claiming a low-spin state for Co^{2+} could be found to corroborate this. Furthermore, the value of the effective magnetic moment ($\sim 4.7\mu_B$) determined from magnetic susceptibility does *not* suggest a low-spin state.

Table 5.2: Change in entropy associated with a change in temperature. All values are given in J/mol K. Percentages are with respect to the theoretical maximum, $R\ln(2S+1)$.

Compound	Saturated Entropy	ΔS_m above T_N	ΔS_m below T_N	$R\ln(2S+1)$
$CuSb_2O_6$	3.75 (65%)	3.23 (56%)	0.52 (9%)	5.763
$NiSb_2O_6$	6.03 (66%)	5.21 (57%)	0.82 (9%)	9.134
$NiTa_2O_6$	8.31 (91%)	6.39 (70%)	1.90 (21%)	9.134
$CoSb_2O_6$	7.61 (66%)	5.65 (49%)	1.96 (17%)	11.526
$CoTa_2O_6$	5.42 (47%)	4.50 (39%)	0.92 (8%)	11.526
$FeTa_2O_6$	11.9 (89%)	8.30 (62%)	3.61 (27%)	13.382
$MnSb_2O_6$	14.6 (98%)	2.53 (17%)	12.1 (81%)	14.898

5.3 Determining the Low-Temperature Energy Gaps

It has been shown by Tari [76] that an exponential decrease of δC_P with decreasing temperature can indicate the presence of an energy gap between the ground state and first excited state. In such case, the data can be fit to the expression $\delta C_P = A\exp(-\Delta_0/k_BT)$. The value of Δ_0/k_B can then be easily extracted from a linear fit to the data plotted as $\ln(\delta C_P)$ versus $1/T$. Only the data from $CuSb_2O_6$ (Δ_0/k_B = 17.7(2) K) was found to be exponential over the full range below T_N (see the insets of Fig. 5.3). This value is very close to Δ_0/k_B = 17.48(6) K reported by Rebello *et al.* using the same method [9]. There, the gap was attributed to coupling between the 1-d Jordan-Wigner-transformed fermions and the 3-d phonons. The magnetic ordering at T_N was viewed as an alignment of the 1-d chains, rather than the formation of a truly 3-d magnetically ordered state.

Unlike $CuSb_2O_6$, the other compounds show either *two* linear regions, as seen for $CoSb_2O_6$, or, more commonly, a non-linear bow (see insets of Fig. 5.3). This non-linearity might be associated with multiple gaps present below T_N. New modes can become populated with an increase in temperature, resulting in a change in slope of δC_P. Antiferromagnetic spin waves (magnons), for example, can also introduce a gap in the energy spectrum [76]. The specific heat therefore requires a more elaborate description. Here, we can make use of the equation

$$\delta C_P = A_1 T\exp(-\Delta_1/k_BT) + A_2T^3\exp(-\Delta_2/k_BT). \tag{5.8}$$

The first term is associated with the decay of the linear-in-T excitations observed above T_N. These are probably due to the regions of the sample that remain unordered below T_N. The second term represents antiferromagnetic magnons with a gap in the dispersion relation [76]. When the data plotted as $\ln(\delta C_P)$ versus $1/T$ are *nearly*

linear, Eq. 5.8 can be used as a minor correction to $\delta C_P = A\exp(-\Delta_0/k_BT)$. This was done in the cases of $NiSb_2O_6$, $CoTa_2O_6$, and $MnSb_2O_6$, where only the magnon term is introduced. It is very interesting to note in the insets of Fig. 5.3e that the plot of $\ln(\delta C_P)$ versus $1/T$ for $MnSb_2O_6$ is almost linear below T_N despite the feature near 5 K in the δC_P data. Without the correction terms of Eq. 5.8, the value of the gap is found to be $\Delta_0/k_B = 7.05(3)$ K.

5.4 Discussion

In this chapter, we have deduced that the short-range order is less prevalent in the tantalate compounds than in the antimonates (see Fig. 5.2). This may be associated with different sizes of the electron orbitals and their ability to overlap with those of the transition metals. The average ionic radii for Sb^{5+} and Ta^{5+} are 0.62 Å and 0.70 Å, respectively [97]. The larger ionic radius for the tantalum ion means that orbital overlap is able to occur over a smaller temperature range upon cooling than for the antimony ion. Therefore the onset of long-range three-dimensional order in the bulk of the samples more rapidly follows the short-range order. Contrarily, the amount of orbital overlap between the antimony ions and the transition metals in the antimonates may be lower, allowing for short-range order to occur over of more extensive temperature range without prompting long-range order.

Despite the observation that long-range order occurs at low temperature, the large change in entropy that occurs above T_N, as well at the fact that the entropy does not reach the full theoretical maximum, suggests that strong magnetic frustration is present in the vicinity of T_N for all of these compounds. The magnetic system must involve Néel ordered regions (i.e., long-range antiferromagnetic ordering), short-range

ordered regions, and unordered regions. The unique antiferromagnetic structure is expected to play a role in generating magnetic frustration, since the 90° orientation of alternating chains along c would most likely weaken the magnetic coupling along this direction, leading to a less robust ordered state below T_N [15]. The weak magnetic exchange [14] within the a-b plane, but in directions other than the chain direction, must also play a role. The nature of the short-range order is probably in the form of dimers, or larger collections of magnetic moments, separated by disordered spins, which can be thought of as a spin liquid. The spin-liquid state is essentially a collection of frustrated spins [101, 102, 103]. At T_N and below, the relatively modest change in entropy suggests that the Néel, dimer, and spin-liquid states coexist.

6. THERMAL EXPANSION

6.1 Introduction

As pointed out in many introductory physics texts, the temperature of a substance is related to its average molecular or atomic energy. For a crystal, atoms are usually depicted in a particular arrangement interconnected by conceptual springs, allowing them to oscillate about their equilibrium position. As the temperature increases, the atoms vibrate faster and their average internal energy increases. If the potential in which the atoms rest, i.e. if the forces binding one atom to another, was purely harmonic, then their average position would remain unchanged as the energy increases, regardless of the oscillation amplitude. Thus, a solid with only harmonic interatomic forces would not expand with temperature. Clearly the inclusion of anharmonic terms are necessary to fully explain thermal expansion. Indeed, the potential energy curves for real solids are not simply harmonic but rather asymmetric. For example, due to additional interatomic forces, it is harder to push atoms together than it is to pull them apart. Therefore, the center of oscillation increases with energy [104]. This is graphically represented in Fig. 6.1.

The technique employed later in this chapter measures *linear* thermal expansion along a single direction. The change in sample length ΔL is normalized by the length of the sample at room temperature, $L_{295\mathrm{K}}$. For an isotropic solid, the coefficient of linear thermal expansion is defined by

$$\alpha = \frac{1}{L}\left(\frac{\partial L}{\partial T}\right)_P = \frac{1}{3V}\left(\frac{\partial V}{\partial T}\right)_P = \frac{1}{3B}\left(\frac{\partial P}{\partial T}\right)_V, \tag{6.1}$$

where V is the sample volume, P is the pressure, and B is the bulk modulus defined as $-V(\partial P/\partial V)_T$. Using the pressure given by the equation of state $P = -(\partial U_0/\partial V) +$

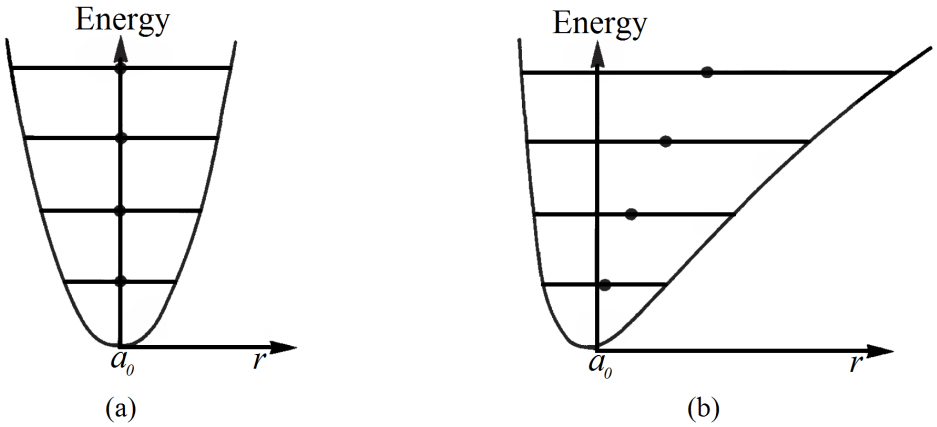

Figure 6.1: (a) Potential for a simple harmonic oscillator. Note that the average separation is always a_0. (b) Asymmetric potential for atoms in a real solid. Note that the average separation increases with energy (temperature), resulting in thermal expansion.

$\gamma(U_D/V)$ derived by Grüneisen [105], and the heat capacity at constant volume $C_V = (\partial U/\partial T)_v$, we may write

$$\alpha = \frac{\gamma}{3B}\left[\frac{\partial}{\partial T}\left(\frac{U_D}{V}\right)\right]_V = \frac{\gamma C_v}{3BV}, \tag{6.2}$$

where U_0 is the internal energy at zero kelvin, U_D is the internal energy in the Debye approximation, and γ is the Grüneisen parameter. This parameter is associated with the various phonon vibrational modes within a crystal and is defined [52] as the weighted average of individual $\gamma_{\mathbf{k}s}$ terms for a specific mode $\mathbf{k}s$

$$\gamma = \frac{\sum_{\mathbf{k},s}\gamma_{\mathbf{k}s}c_{vs}(\mathbf{k})}{\sum_{\mathbf{k},s}c_{vs}(\mathbf{k})}. \tag{6.3}$$

The contribution of each normal mode is weighted by its contribution to the specific heat. The $\gamma_{\mathbf{k}s}$ are often expressed in terms of the phonon frequency mode $\omega_s(\mathbf{k})$ as

$$\gamma_{\mathbf{k}s} = -\frac{\partial(\ln\omega_s(\mathbf{k}))}{\partial(\ln V)}. \tag{6.4}$$

In the Debye model, $\omega_s(\mathbf{k})$ is just the Debye frequency ω_D. Since the bulk modulus only weakly depends on temperature, the thermal expansion coefficient should have

the same temperature dependence as the specific heat. In particular, at low temperature, where very few vibrational modes are active, both specific heat and α tend toward zero; and at temperatures much larger than the Debye temperature Θ_D, both values approach a constant.

6.2 Negative Thermal Expansion

In general, the coefficient of thermal expansion is positive over the entire temperature range, i.e. the material expands with an increase in temperature. However, some unconventional materials display *negative* thermal expansion, in which the lattice shrinks with increasing temperature. Water ice is a classic example, exhibiting negative thermal expansion over the range 0 K to $\sim$ 63 K [106]. This phenomenon is usually observed in materials at low temperatures where anomalous (negative) vibrational modes $\gamma_{\mathbf{k}s}$ dominate the weighted sum, such that γ in Eq. 6.3 is negative.

The sign of the individual Grüneisen parameters is determined by the dynamic interactions between adjacent ions. There are three basic mechanisms which will be discussed: bond-stretching, tension, and bond-rotation [107]. The first mechanism is that which drives the anharmonicity of Fig. 6.1b and occurs when the vibrational displacements have components along a bond direction. Relating it to Eq. 6.4; when the volume V increases, the bonds lengthen thus weakening the interatomic forces and decreasing the phonon frequencies. This results in a positive contribution to $\gamma_{\mathbf{k}s}$ and the thermal expansion. Alternatively, when the vibrational displacements have components perpendicular to the bond direction, a tension effect is introduced. In this situation, transverse oscillations increase the distance between adjacent atoms which increases tension in the bonds. In turn, the phonon frequency also increases,

much akin to frequencies increasing as one increases the tension in a string. With both $\omega_s(\mathbf{k})$ and the atomic separation increasing, it follows that $\gamma_{\mathbf{k}s}$ in Eq. 6.4 is negative, resulting in negative thermal expansion. The final mechanism, bond-rotation, is a combination of the two aforementioned effects with an additional torque introduced. This mechanism is typically much less important because different vibrational modes have a tendency to rotate the bonds in different directions, counteracting one another.

Usually the bond-stretching mechanism dominates over the others, resulting in an overall positive thermal expansion. The modes which allow the tension mechanism to dominate usually involve lower frequencies. It is for this reason that negative thermal expansion often occurs at very low temperatures.

6.3 Experimental Procedure using a Quartz Dilatometer

There are various methods to measure the thermal expansion of solids. One of the oldest methods uses simple mechanical dilatometry in which the length of the sample is transmitted through the use of push-rods to a sensor that is separated from the heat source. Optical methods can also be employed which utilize high-magnification microscopes, interferometers, and even x-ray diffraction. James *et al.* offers a nice review of the above, and additional, techniques [108]. Some off-the-shelf capacitor bridges offer relative resolution of 1 part in 10^8. If the change in separation between the capacitor plates Δd is coupled to the length change of a sample ΔL, then capacitance-based dilatometer cells are able to resolve changes in sample length of 0.1 Å.

Capacitance-based dilatometers have commonly been made out of copper or copper alloys. However, copper has a very large thermal expansion coefficient, which

means that the contribution from the samples being measured is often small in comparison. Furthermore, insulating spacers placed at critical positions in the cell are needed to electrically isolate the two capacitor plates. These spacers necessitate the subtraction of differential thermal expansion effects from the data. This is far from ideal when trying to observe subtle changes associated with phase transitions. The current setup employed herein uses fused quartz rather than copper. There are a couple of reasons for this decision. Firstly, fused quartz has a very small thermal expansion coefficient which translates to a smaller contribution of the cell material to the data. However, this advantage is only appreciated above 27 K, below which the thermal expansion coefficients of copper and quartz are about equal, with copper being the smaller of the two. Secondly, because fused quartz is an electrical insulator, there is no need for insulating spacers to electrically isolate the two capacitor plates. Without them, the *empty cell effect* (the change in capacitance of the dilatometer cell without the sample present) is better behaved and smaller in magnitude.

The construction of the quartz dilatometer and the details surrounding the calibration have been thoroughly outlined and reported elsewhere [79, 109]. Therefore, only a brief summary will be replicated here. The dilatometer cell is constructed from only five parts: two L-shaped pieces, two springs, and a wedge. One of the L-shaped pieces constitutes the base and a vertical side of the cell. Gold is deposited on the inside wall of this piece which serves as one of the capacitor plates. The other gold capacitor plate is deposited upon the second L-shaped piece, which is flipped vertically from the former's orientation and rests suspended by the vertical pair of delicate quartz springs. The springs are no more than thin plates roughly 0.1 mm in thickness and are adhered using a Ni_2SiO_3 solution. (See Fig. 6.2 for a detailed schematic.) This setup allows the capacitor plates to remain parallel as the L-shaped pieces are pushed apart by the sample that is placed within the valley between them.

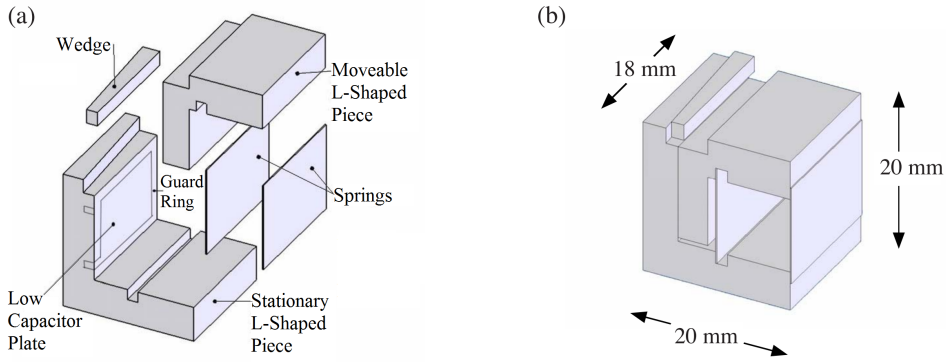

Figure 6.2: Fused-quartz dilatometer cell. Reprinted from Neumeier *et al.* [109]. (a) Exploded view of the constituent pieces. (b) Fully assembled cell.

Since the sample is often too small to span the entire gap, a small quartz wedge is placed between the sample and the stationary wall. The wedge and the wall are both tapered by 3°, allowing the wedge to push the sample against the moveable L-shaped piece in opposition of the tension supplied by the springs.

The capacitance is measured using an Andeen-Hagerling precision capacitance bridge. The sensitivity is less than an attofarad which corresponds to a change in sample length on the order of 0.1 Å for samples that are 1-2 mm long. This relative resolution is about a thousand times better than the highest resolution diffraction measurements. The sample temperature is measured using a LakeShore 340 temperature controller. Inside the controller are two resistive thermometers, one made of Cernox^{TM}and the other of platinum. The former is a semiconducting thin-film resistor which has high sensitivity at low temperatures. The temperature used in the measurement is a weighted average of the two thermometer readings. (Below 50 K, the temperature is read almost exclusively by the Cernox^{TM} thermometer.) The dilatometer cell is calibrated using a sample of high-purity annealed copper [109] prior to measuring the samples.

6.4 Thermal Expansion and its Coefficient of $M(\mathrm{Sb,Ta})_2\mathrm{O}_6$

The normalized change in sample length for each compound studied herein is shown in Figs. 6.3 and 6.4. Compounds containing like transition metals show similar expansion within the magnetic planes. That is to say, the magnitude of the relative change in length over the temperature range 5 K$< T <$300 K is approximately the same. The expansion along the c-axis, however, varies greatly between the antimonates and the tantalates. This observation seems reasonable since the magnetic planes for each compound contain only transition metals and oxygen atoms. Apart from the lattice spacings, which differ by only a couple percent, the crystallographic planes of the antimonates and tantalates with common transition metals are identical. On the other hand, the ionic radius of Ta^{5+} is about 13% larger than the ionic radius of Sb^{5+}. It seems, therefore, that the diamagnetic ions separating the magnetic planes are responsible for the vastly different expansions along the c-axis observed between compounds with like transition metals.

A change in slope of $\Delta L/L$ occurs at T_N for each axis measured. Since a change in slope is observed rather than a jump, the phase transitions appear to be *continuous* in nature, i.e. the first derivative is continuous. This is also known as a *second-order* phase transition. Physically, this means that the transition from one phase to the other takes place without abrupt changes in the entropy or Gibbs free energy. For the tetragonal compounds, which include $\mathrm{Ni(Sb,Ta)_2O_6}$, $\mathrm{Co(Sb,Ta)_2O_6}$, and $\mathrm{FeTa_2O_6}$, the data above T_N for the change in length along the a-axis is identical to that of the b-axis within experimental uncertainty. This is consistent with the tetragonal crystal structure of each compound. The subtle differences observed in the data for $\mathrm{CuSb_2O_6}$ is associated with the known monoclinic distortion that occurs below $T = 380$ K.

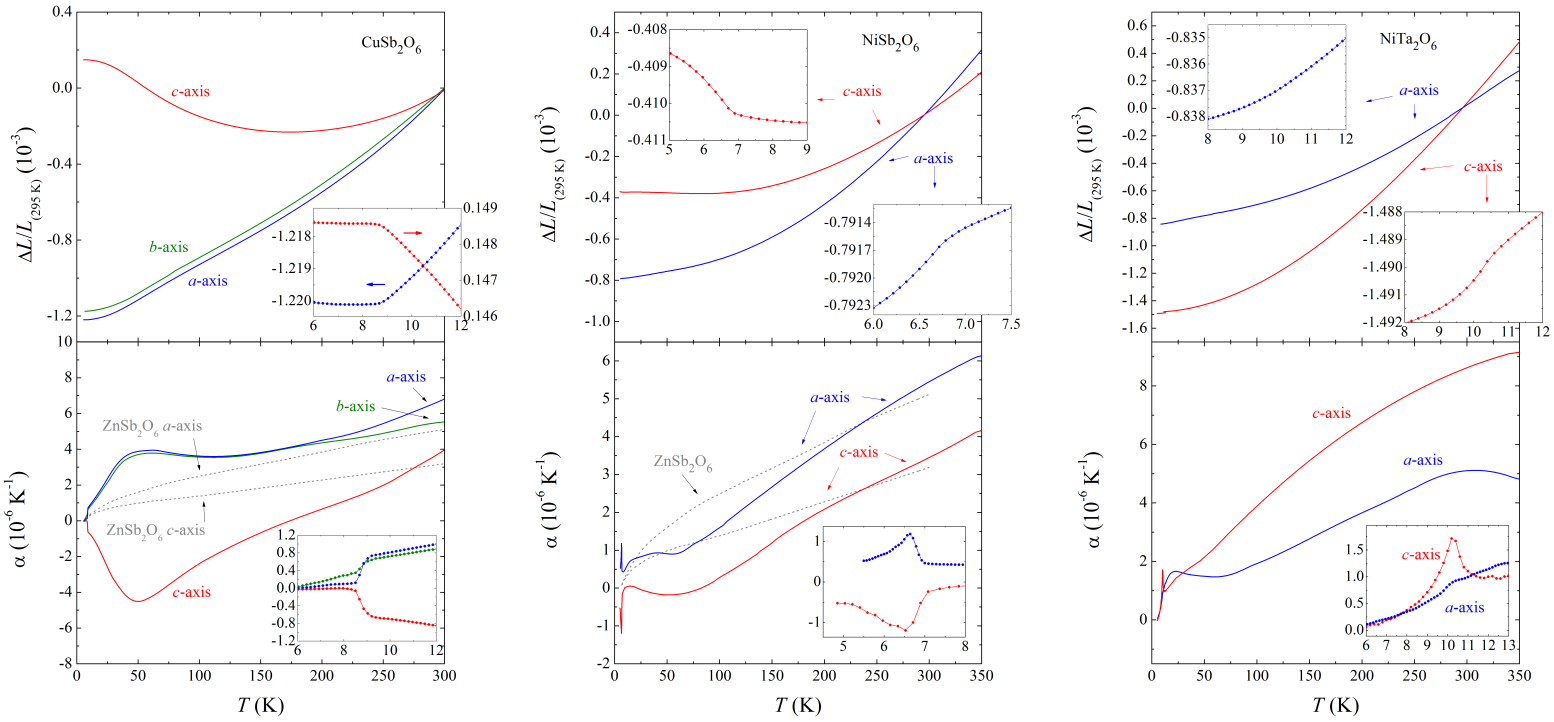

(a) $CuSb_2O_6$ (b) $NiSb_2O_6$ (c) $NiTa_2O_6$

Figure 6.3: (Upper panels) Linear thermal expansion $\Delta L/L$ of $CuSb_2O_6$ and $Ni(Sb,Ta)_2O_6$ normalized to the length at 295 K. The insets reveal the region near T_N. (Lower panels) Thermal expansion coefficient $\alpha = d/dT(\Delta L/L)$ for $M(Sb,Ta)_2O_6$ (solid lines) and the nonmagnetic analog $ZnSb_2O_6$ (dashed lines). Data for $CuSb_2O_6$ is generously provided by Dr. Alwyn Rebello.

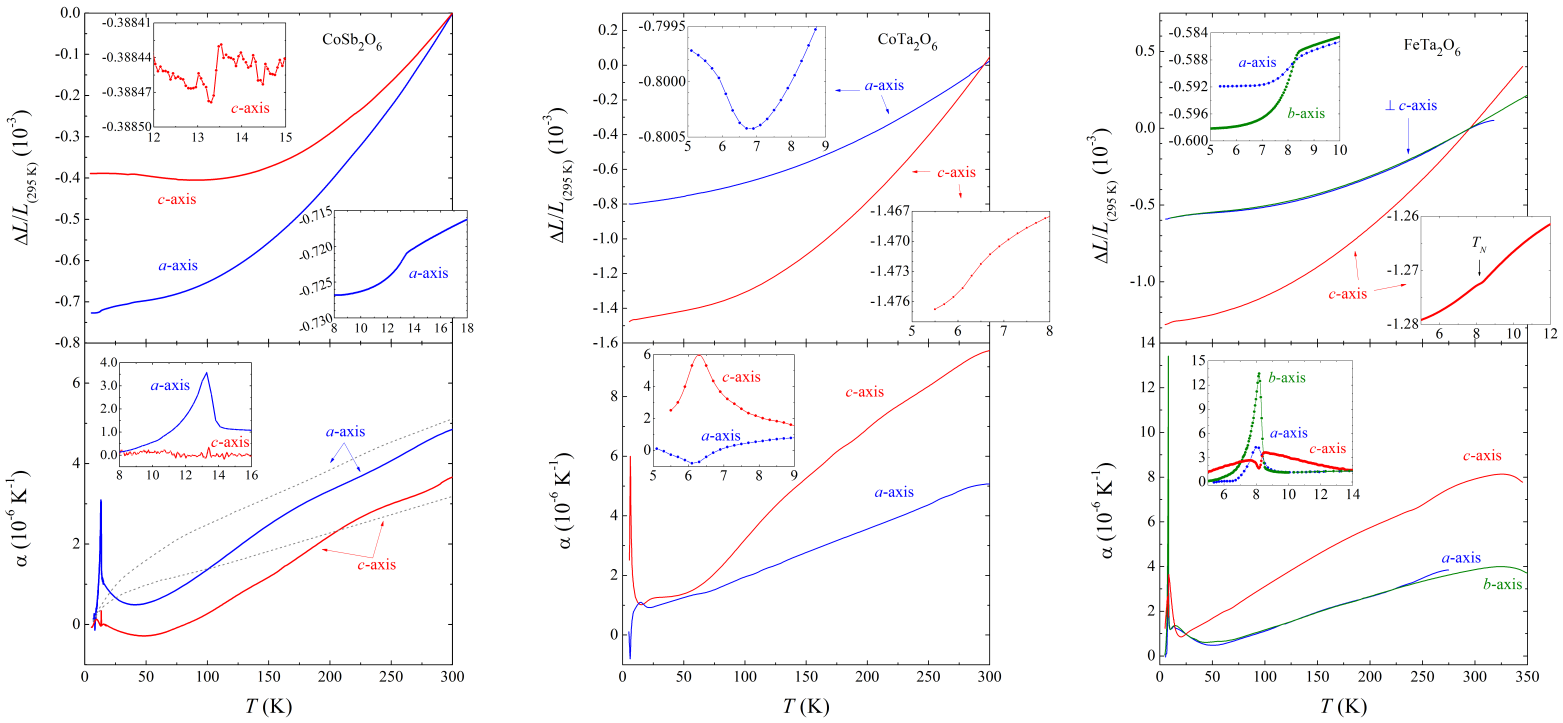

(a) $CoSb_2O_6$ (b) $CoTa_2O_6$ (c) $FeTa_2O_6$

Figure 6.4: (Upper panels) Linear thermal expansion $\Delta L/L$ of $Co(Sb,Ta)_2O_6$ and $FeTa_2O_6$ normalized to the length at 295 K. The insets reveal the region near T_N. (Lower panels) Thermal expansion coefficient $\alpha = d/dT(\Delta L/L)$ for $M(Sb,Ta)_2O_6$ (solid lines) and the nonmagnetic analog $ZnSb_2O_6$ (dashed lines).

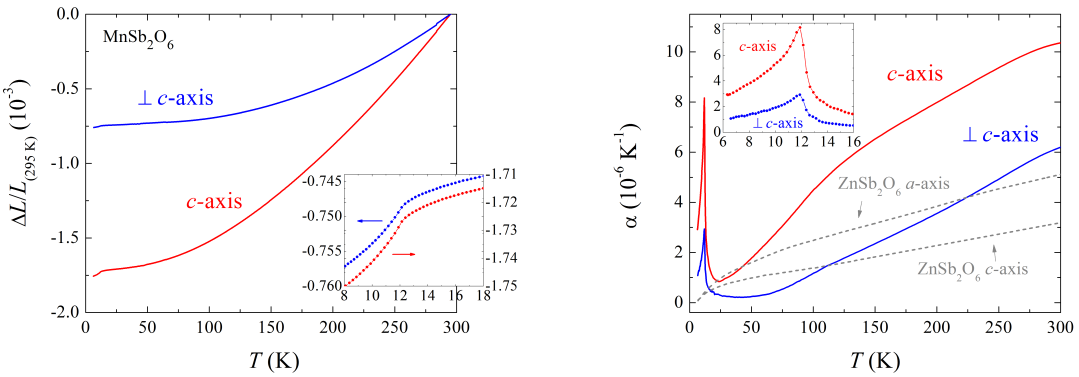

Figure 6.5: (a) Linear thermal expansion $\Delta L/L$ and (b) its coefficient for the trigonal compound $MnSb_2O_6$. The data is normalized to the length at 295 K. The insets show expanded views of the region around T_N.

Dilatometry is most accurate when the sample sizes are large. Unfortunately, the samples measured in this study are typically 1 mm in length or less. Multiple measurements for each direction have been averaged in order to obtain a smooth $\Delta L/L$ curve. However, despite this effort, the point-by-point derivative can still contain small fluctuations. To tackle this issue, the data away from T_N was fit using Chebyshev polynomials, following the method outlined by White [79], in order to obtain smooth derivatives. The derivative of the normalized change in length provides the thermal expansion coefficient, α, plotted in the lower panels of Figs. 6.3 and 6.4. The minima observed in the coefficients occur near the onset of short-range order. While the coefficient is positive over much of the temperature range for each compound, there are some occurrences of negative thermal expansion. $CuSb_2O_6$ and $NiSb_2O_6$ both show a negative α value for the c-axis below temperatures beginning well above T_N. The c-axis of $CoSb_2O_6$ also shows negative thermal expansion, but the region terminates before reaching T_N, below which α returns to positive. The value of α for the a- and b-axis of $CoTa_2O_6$ is negative only below T_N. As stated in

Section 6.2, these regions are associated with transverse oscillation modes. Compare these data to those of the nonmagnetic analog $ZnSb_2O_6$, drawn as dotted grey curves, which exhibit monotonic behavior and are positive over the entire temperature range. The tetragonal lattice parameters of the nonmagnetic analog differ from the other compounds by only $\sim 2\%$. Therefore this difference in α must be associated with the magnetic ions and local magnetic order along the M-O-O-M chains. This local magnetic order would directly affect the pair potentials in ordered regions of the samples, which in turn could dramatically alter the phonon spectra, especially given the large fraction of magnetic ions participating in magnetic order indicated by the magnetic entropy data in Section 5.2.1.

Large features in α at T_N indicate that the coupling between the lattice and the magnetic order is strong. The size of these features measured along the a- and c-axis are comparable in $CuSb_2O_6$ and $NiSb_2O_6$. In $CoSb_2O_6$ and $FeTa_2O_6$, the features measured perpendicular to the c-axis are the dominant ones. Contrastingly, the features measured parallel to the c-axis dominate in the compounds $NiTa_2O_6$, $CoTa_2O_6$, and $MnSb_2O_6$. These latter results are expected for $MnSb_2O_6$ since magnetic susceptibility has shown the easy axis to be along [001]. The magnetic structure of $CoTa_2O_6$ is also suspected [29] to contain moments with projections along [001]. However, because the moments are thought to be mainly confined to the a-b plane in $NiTa_2O_6$, the large feature in α observed for measurement along [001] is quite unexpected. The relatively large size of this feature in measurements along this direction in both $NiSb_2O_6$ and $NiTa_2O_6$ might have origins in the canting of the moments out of the magnetic plane for $T < T_N$, as suggested by the increase in magnetic susceptibility upon cooling.

6.5 Thermodynamic Scaling Relations and Critical Exponents

In this section, let us revisit heat capacity and its relation to the thermal expansion. Data from these independent measurements can be used to predict interesting thermodynamic quantities, such as the pressure dependence of the transition temperature. The heat capacity in the vicinity of the transition can be written as [110]

$$C_P = T\left(\frac{\partial S}{\partial T}\right)_N + \nu T\Omega\left(\frac{\partial P}{\partial T}\right)_N, \tag{6.5}$$

where S, P, ν, and Ω are the molar entropy, pressure, molar volume, and volume thermal expansion coefficient, respectively. The subscript N denotes that the equation is valid near the Néel temperature. The quantity Ω is taken to be the sum of the linear expansion coefficients $(\alpha_a + \alpha_b + \alpha_c)$ near T_N. The first term in Eq. (6.5) is a linear entropy term that is subtracted from C_P to yield $C_P^* \equiv C_P - a - bT$. With $\nu/\lambda = dT_N/dP$, C_P^* scales with $\lambda\Omega T$. The values a, b, and λ are chosen such that the two curves (C_P^* and $\lambda\Omega T$) have the best possible overlap. A good overlap would suggest that the phase transition at T_N is continuous. This analysis has been applied to $M(\mathrm{Sb,Ta})_2\mathrm{O}_6$ and the plots of C_P^* and $\lambda\Omega T$ versus temperature are shown in Fig. 6.6 for the antimonates and Fig. 6.7 for the tantalates. In most cases, there is good overlap above and below T_N. Unfortunately, minor discrepancies occur at the peak for the tantalates. In the cases of $\mathrm{NiTa_2O_6}$ and $\mathrm{CoTa_2O_6}$, small amplitudes of the peak in α associated with the a-b plane contribute insufficient amounts to Ω, causing the overall peak of $\lambda\Omega T$ to be smaller than that for C_P^*. In the case of $\mathrm{FeTa_2O_6}$, heat capacity data falls short of the $\lambda\Omega T$ peak. This can occur if the sample is too massive to allow even heating [79]. Despite the failure of the peaks to perfectly match between the two methods, the slopes above and below the peak are in agreement. Acceptable

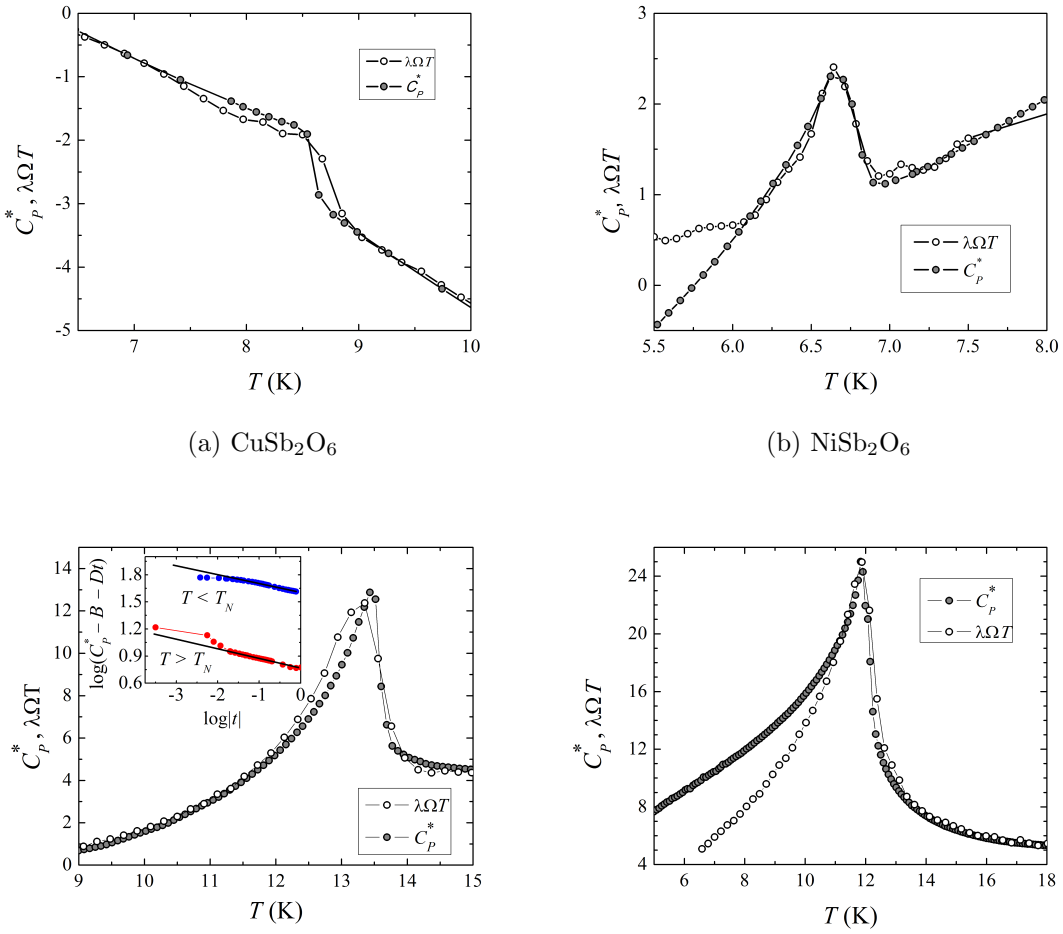

(a) $CuSb_2O_6$ (b) $NiSb_2O_6$

(c) $CoSb_2O_6$ (d) $MnSb_2O_6$

Figure 6.6: Plot of C_P^* and $\lambda\Omega T$ versus temperature illustrating the overlap of heat capacity and volume thermal expansion coefficient data near T_N for the antimonates. Insets show the critical behavior of C_P^*. The slope of the curves provide $-\alpha_{\pm}$.

parameters can, therefore, still be extracted. The parameters used to overlap the C_P^* and $\lambda\Omega T$ data is provided in Table 6.1.

The data for C_P^* can be further analyzed in the vicinity of the phase transition to determine the heat-capacity critical exponent, $\alpha_{\pm}$. Knowledge of critical exponents can be useful in classifying the behavior of physical quantities. The singularity in the heat capacity around a phase transition originates from a nonanalytic term in

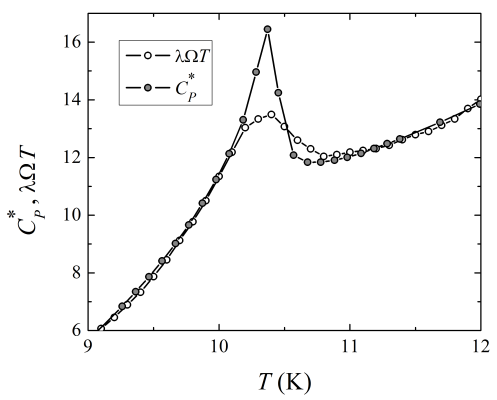

(a) $NiTa_2O_6$

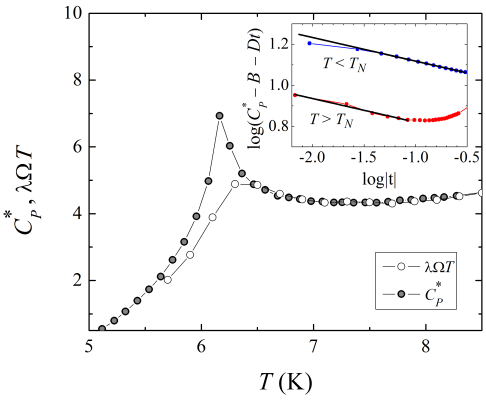

(b) $CoTa_2O_6$

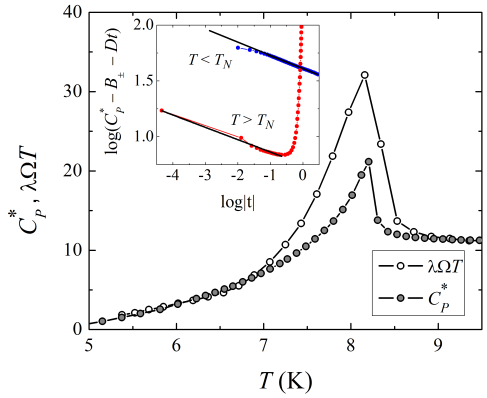

(c) $FeTa_2O_6$

Figure 6.7: Plot of C_P^* and $\lambda\Omega T$ versus temperature illustrating the overlap of heat capacity and volume thermal expansion coefficient data near T_N for the tantalates. Insets show the critical behavior of C_P^*. The slope of the curves provides $-\alpha_\pm$.

the thermodynamic free energy, and it can be asymptotically described [110] by a function of the form

$$C_P^* = \left(\frac{A_\pm}{\alpha_\pm}\right)|t|^{-\alpha_\pm} + B_\pm + Dt, \tag{6.6}$$

where t is the reduced temperature $t \equiv |T - T_N|/T_N$ and $A_\pm$, $B_\pm$, and D are constants [79, 110]. The subscripts denote values of the parameters above $(+)$ and below $(-)$ T_N.

Table 6.1: Parameters used to overlap C_P^* and $\lambda\Omega T$.

Compound	ν [cm^3/mol]	a [J/mol K]	b [J/mol K^2]	λ [MJ/mol K]	dT_N/dP [K/GPa]
$CuSb_2O_6$	60.13	−7.1	1.25	−0.550	−0.11
$NiSb_2O_6$	59.79	6.2	−0.79	0.280	0.21
$NiTa_2O_6$	61.43	17	−2.0	0.365	0.17
$CoSb_2O_6$	60.42	0.2	−0.06	0.170	0.36
$CoTa_2O_6$	61.93	3.5	−0.46	0.170	0.36
$FeTa_2O_6$	62.76	3.5	−0.45	0.205	0.31
$MnSb_2O_6$	95.49	−2.0	−0.01	0.150	0.64

The values of $\alpha_\pm$ can be determined from the C_P data by plotting $\log(C_P^* - B_\pm - Dt)$ against $\log(t)$ and adjusting fit parameter values until the regions above and below the phase transition become linear, with similar slopes. For a continuous phase transition, we should expect $\alpha_+ \approx \alpha_-$.

Predictions for a given universality class (e.g. Heisenberg, XY, Ising, etc.) are usually calculated assuming a ferromagnetic model, which differs from an antiferromagnetic model only in the sign of the magnetic interaction strength. However, the specific value of the spin has no influence on the universality class [111, 112]. The partition functions for each case will therefore be identical if the sign of one of the magnetic interactions is changed. Consequently, predictions for the critical behavior are the same [113]. A report by Kornblit showed that experimentally determined values of critical exponents measured for an antiferromagnetic system can correspond to critical behavior predicted for an analogous ferromagnetic system [114]. Therefore, in the current investigation, we assume that critical exponents theoretically determined for the ferromagnetic models can serve as a guide for the antiferromagnetic cases.

Table 6.2: Thermodynamic Scaling Relations and Critical Exponents of $M(\mathrm{Sb,Ta})_2\mathrm{O}_6$ Compounds. The values for $\alpha_\pm$ are unitless. All other quantities are given in J/mol K.

Compound	A_+	A_-	B_+	B_-	D	α_+	α_-
$\mathrm{CoSb_2O_6}$	0.229(2)	0.499(8)	−4.5	−45	5.0	0.1062(9)	0.100(2)
$\mathrm{CoTa_2O_6}$	0.23(2)	0.314(3)	−2	−11	−2.9	0.115(7)	0.115(1)
$\mathrm{FeTa_2O_6}$	0.23(1)	0.56(1)	4	−43	1.5	0.110(3)	0.113(1)

Using Eq. 6.6 and the following procedure, critical exponents have been obtained for $\mathrm{Co(Sb,Ta)_2O_6}$ and $\mathrm{FeTa_2O_6}$. Plots of $\log(C_P^* - B_\pm - Dt)$ versus $\log(t)$ are shown in the insets of Figs. 6.6 and 6.7. Quantities used in the analysis are provided in Table 6.2. Unfortunately, parameters could not be found for the compounds $\mathrm{CuSb_2O_6}$, $\mathrm{Ni(Sb,Ta)_2O_6}$, and $\mathrm{MnSb_2O_6}$ such that $\alpha_- = \alpha_+$.

The resulting values of $\alpha_\pm$ are all similar to the value 0.11 required for the 3D Ising model [115]. The ratio A_+/A_- is also of importance and is predicted to be a universal quantity that should be identical for all systems in a given universality class. For the Ising model, the ratio A_+/A_- is theoretically calculated [116, 117] to be 0.523(9). The analysis described above yields A_+/A_- equal to 0.459(11), 0.73(7), and 0.41(3) for $\mathrm{CoSb_2O_6}$, $\mathrm{CoTa_2O_6}$, and $\mathrm{FeTa_2O_6}$ respectfully. These results are in the neighborhood of the expected theoretical value and are quite acceptable considering that in some instances the linear regions expand only a couple decades. This outcome supports the claim of Ising-like behavior of the magnetic interactions within these three compounds.

7. MAGNETOCALORIC EFFECT

7.1 Introduction

The first observation of the magnetocaloric effect (MCE) occurred in 1917 by Weiss and Piccard while investigating nickel [118]. Since then, a vast number of materials that display the MCE have been discovered. Those used in applications that utilize the effect are most often polycrystalline or inherently isotropic. This is because they are usually magnetically soft or contain crystal structures with cubic symmetry [119]. However, a material that is single-crystalline and contains low-dimensional spin chains can have interesting anisotropic responses to applied field, setting it apart from the more conventional compounds.

Despite the fact that low-dimensional materials have been around since the mid 1900s, there have been surprisingly few theories that describe the field-dependence of the ordering temperature which also take into account the spin and lattice dimensionalities. Furthermore, many of these theories limit themselves to only $S = 1/2$ systems. Villain and Loveluck have helped to advance the theory by discussing the effect of magnetic field on the correlation lengths [120]. The authors suggest that at low temperatures, the application of magnetic field H which satisfies the relation

$$k_B T \lesssim \mu_{\text{eff}}(\mu_0 H) \ll 4|J||\mathbf{S}|^2 \tag{7.1}$$

reduces the spin dimensionality and transforms an XY chain into an Ising chain, and a Heisenberg chain into an XY chain by suppressing fluctuations along all directions, especially that of the applied field. Upon the transformation to a lower spin-dimensionality, the correlation length increases [120, 121, 122]. Longer correlation

Figure 7.1: (a) Magnetic field applied perpendicular to the spin cone axis causes the cones to flatten. (b) The spin cones are broadened when exposed to a magnetic field applied parallel to the axes.

lengths mean that a transition to long-range order is more probable, i.e. the transition occurs at higher temperature. Qualitatively, when a magnetic field is applied perpendicular to the spin cones (see Fig. 7.1a), the fluctuations of spin components parallel to the field within the cones are suppressed, and the cones flatten (and slightly cant) in the direction of the applied field [123]. This flattening increases the antiferromagnetic exchange interactions along the chains and in turn causes the Néel temperature to increase. Similarly, when the field is applied along the axes of the spin cones, i.e. along the easy axis, the cones broaden (see Fig. 7.1b), which decreases the correlation length along their axes. Subsequently, a decrease in T_N is observed.

More thorough theoretical expressions describing the behavior of the Néel temperature in response to applied magnetic field have been developed by Singh *et al.* [124], which expanded upon a relation obtained previously by Oguchi [125]. In developing the theory, it is stated that the only restrictions on the system are that (1) the magnetic structure contains only one easy axis and (2) the two anti-aligned ferromagnetic sublattices that define the AFM ordered state should be translationally invariant [126]. While the compounds studied herein do not meet the first criteria, we

shall continue with the use of the theory as a qualitative guide. The theory utilizes the Hamiltonian

$$\mathscr{H} = 2\sum_{<ij>} J_{ij}\mathbf{S_i}\cdot\mathbf{S_j} - g\mu_B H\sum_i S_i^Z - K\sum_i (S_i^Z)^2, \tag{7.2}$$

where J_{ij} is the usual exchange interaction between nearest neighboring spins, H is the magnetic field applied along the antiferromagnetic axis (the Z direction), and K is the uniaxial anisotropy along the Z direction. (Note here that, because the Hamiltonian is positive, a positive value of J now corresponds to antiferromagnetic behavior, whereas in previous chapters a positive value meant ferromagnetic coupling.) Using approximations for the parallel susceptibility determined by Joenk [127], Singh *et al.* arrived at the expression

$$\frac{\Theta}{T_N} = \frac{1}{\pi^3}\int_0^{\pi}\!\!\int\!\!\int \frac{\mathrm{d}q_x\mathrm{d}q_y\mathrm{d}q_z}{(K/2J - AH^2) + (1-\cos q_z) + \eta(1-\cos q_x) + \eta(1-\cos q_y)}, \tag{7.3}$$

where $\Theta = 4JS(S+1)/(3k_B)$, $\eta = J'/J$, and J and J' are exchange integrals within the chain and between the chains, respectively. The anisotropy and exchange fields can be determined upon replacing $K/2J$ with the ratio of the two fields H_A/H_E and making the substitution $A = 1/(2H_E^2)$ [124]. The value of η provides a sense of the degree of one-dimensionality of the spin chains. For a truly 1-d system, $\eta = 0$. It is clear from Eq. 7.3 that the increase of anisotropy, K, decreases the value of the triple integral which, in turn, increases the value of T_N. In a Heisenberg system, K is small. This value increases when the spin dimensionality, D, decreases, i.e. when going from a Heisenberg system ($D = 3$) to an XY system ($D = 2$), or from XY to Ising ($D = 1$). Increasing the anisotropy therefore has the same effect as reducing the dimensionality as described by Villain and Loveluck [120].

When field is applied perpendicular to the easy axis, the spins are canted toward the paramagnetic phase by an angle ϕ. In this configuration, the *planar* anisotropy

is taken to be zero. Applying similar approximations as before, Singh *et al.* obtained the following expression for the Néel temperature with respect to field

$$\frac{\Theta}{T_N} = \frac{1}{\pi^3}\int_0^{\pi}\!\!\int\!\!\int \{2(1+2\eta)\sin^2\phi \pm (K/2J)\cos^2\phi + \cos 2\phi \\ \times [(1-\cos q_z) + \eta(1-\cos q_x) + \eta(1-\cos q_y)]\}^{-1} \mathrm{d}q_x \mathrm{d}q_y \mathrm{d}q_z, \tag{7.4}$$

where $\sin\phi = H/(2H_E \pm H_A)$. In this equation, the (+) sign pertains to field along the hard axis and the (−) sign pertains to field along the easy axis when $H > H_{SF}$. Application of field perpendicular to the moments increases the effective anisotropy in Eq. 7.4 which, in turn, increases T_N. Qualitatively, the magnetic field stabilizes the moments against thermal fluctuations, allowing them to order at higher temperature. The fact that the moments order at temperatures either higher or lower than the zero-field case, depending upon the field direction, means that the peaks in heat capacity associated with the phase transition will also shift correspondingly. This change in heat capacity due to the application of field is fundamental to the magnetocaloric effect, due to the associated magnetic entropy change.

Many of the antiferromagnets studied herein are shown, for the first time, to exhibit the magnetocaloric effect. Two compounds which do not are $CuSb_2O_6$ and $MnSb_2O_6$. The absence of a MCE in these two cases is attributed to their different antiferromagnetic structure and their propensity to exhibit a spin-flop transition at magnetic fields much lower than the other compounds (see Section 4.3). A spin-flop transition allows the compounds to lower the energy of their moments in the presence of H without a noticeable reduction of T_N. In the spin-flop configuration the material behaves paramagnetically when $H < H_{sat}$. The lack of additional phase transitions in this region prevents any rapid change in entropy (or similarly, heat capacity) upon which the MCE so heavily relies.

7.2 $NiSb_2O_6$

Magnetic susceptibility χ and its temperature derivative of $NiSb_2O_6$ for a variety of field strengths are shown in Fig. 7.2. Typically it is the magnetization, and not χ, that is used to analyze the MCE; but the latter is presented here to better display the shifts of T_N. From the figure, we observe that application of field along [110] results in two kinks in χ that shift away from $T_N(H = 0)$ with increasing field; one to lower and the other to higher temperature. These kinks can be understood if one considers the two-sublattice model. When field is applied along either [110] or $[1\bar{1}0]$, one sublattice contains moments parallel to the field (denoted as the easy sublattice) while the other contains moments which are perpendicular (denoted as the hard sublattice). The susceptibility at temperatures immediately below the high-temperature kink deviates slightly upward upon cooling, similar to what is seen for $H \parallel [001]$ (i.e. when field is perpendicular to the moments). At temperatures below the low-temperature kink, χ drops more steeply, similar to what is observed in a standard AFM phase transition when magnetic field is applied along the easy axis. We can therefore say with confidence that the kinks above and below 6.7 K are attributed to the long-range order of the hard and easy sublattices, respectively. The shifts to higher and lower temperature are best seen in the data when plotted as $\mathrm{d}\chi/\mathrm{d}T$.

As expected, the shifted Néel temperatures are accompanied by a corresponding shift of the peaks in heat capacity shown in Fig. 7.3a. No appreciable shift of the peak occurs when field is along either the a- or b-axis. In this case the moments are angled 45° to H. An effective field of $H/\sqrt{2}$ is therefore projected along the moments of either sublattice, causing a minor shift of T_N to lower/higher temperature for the

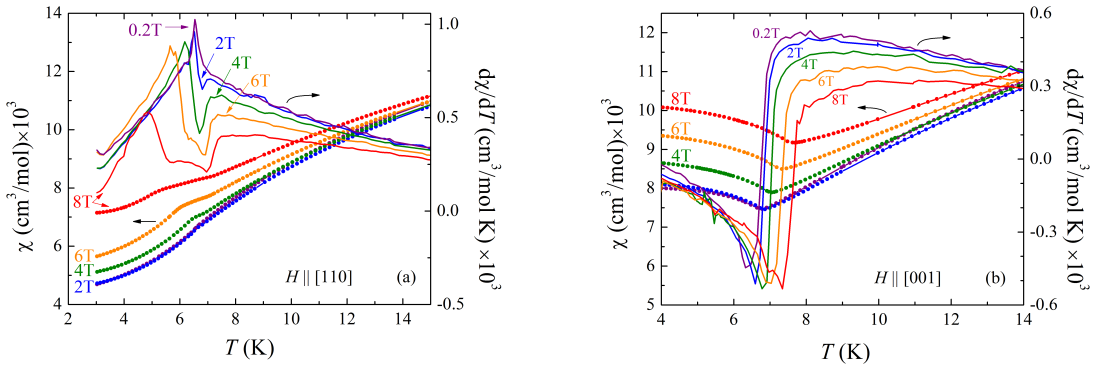

(a) Field $H \parallel [110]$ (b) Field $H \parallel [001]$

Figure 7.2: Magnetic susceptibility χ (left vertical axis) and its derivative $\mathrm{d}\chi/\mathrm{d}T$ (right vertical axis) versus temperature T for $NiSb_2O_6$ in various fields.

easy/hard sublattice, respectively. The net effect is a slight broadening of the peak in C_P.

The field dependence of T_N is plotted in Fig. 7.3b. Data for H parallel to the easy sublattice and to the c-axis have been fit using Eqs. 7.3 and 7.4, respectively. The value of the exchange coupling used in the fits was restricted to $|J|/k_B = 26$ K determined from magnetic susceptibility. The measured value of the spin-flop field can be used with Eq. 4.9 to restrict either H_A or H_E, limiting the number of fitting parameters to two: η and either one of the fields. The two curves fit the data very well, resulting in the parameters listed in the figure. The low value of η indicates the system can be regarded as pseudo one-dimensional. The value of the anisotropy energy corresponds to 5.5 μeV, which is about half the value determined by Eq. 4.6 using the low-temperature magnetic susceptibility.

The increase of T_N when field is applied perpendicular to the moments is consistent with the notion of reducing the spin-dimensionality described in the introduction to this chapter. Using the exchange constant, J, determined from magnetic suscepti-

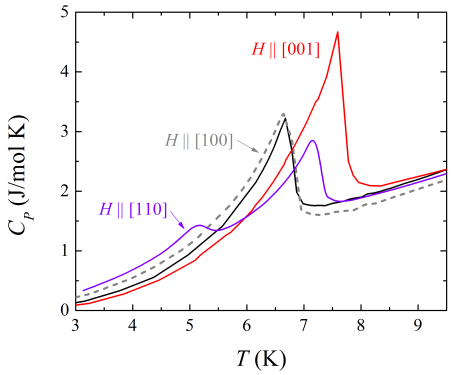

(a) In-field heat capacity C_P of $NiSb_2O_6$.

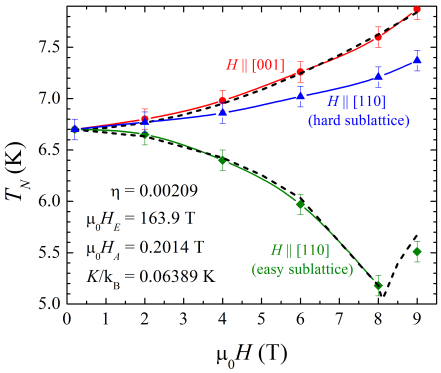

(b) The field dependence of T_N for $NiSb_2O_6$

Figure 7.3: (a) The field dependence of C_P. Here, $\mu_0 H = 8$ T. For $H \parallel [110]$ (purple curve), two peaks emerge in the C_P data as magnetic field is increased in magnitude. For $H \parallel [100]$ (grey dotted line) no appreciable shift of the peak from the zero-field measurement (solid black line) is observed. (b) Néel temperature plotted as a function of external magnetic field for $H \parallel [001]$ (red circles) and $H \parallel [110]$. The two curves for $H \parallel [110]$ are for the sublattices whose moments are parallel (green squares) and perpendicular (blue triangles) to the field. The black dashed curves are fits from Eqs. 7.3 and 7.4 using the parameters in the lower left. The spin-flop field marks a turn-around point of $T_N(H)$ when H is parallel to the moments. Solid lines are guides for the eye.

bility, the right inequality of Eq. 7.1 is easily satisfied. Using $T = 6.7$ K and μ_{eff} from the Curie-Weiss analysis, the left inequality is satisfied for fields above ~ 3 T (corresponding to $\mu_{\text{eff}}(\mu_0 H) \approx 0.58$ meV).

7.3 $NiTa_2O_6$

The derivative of the magnetization of $NiTa_2O_6$ is shown in Fig. 7.4 for a variety of fields along different axes. Data for $H \parallel [1\bar{1}0]$ and $H \parallel [010]$ are indistinguishable from those for $H \parallel [110]$ and $H \parallel [100]$, respectfully, and are therefore omitted. Just as with $NiSb_2O_6$, a shift of T_N to lower temperature is observed when field is applied within

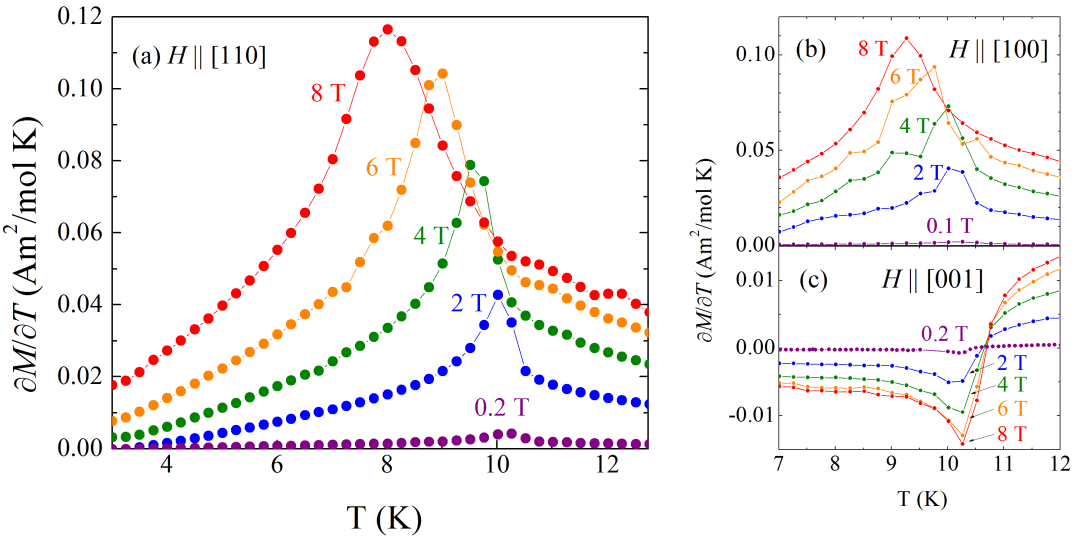

Figure 7.4: Derivative of magnetization with respect to temperature $\partial M/\partial T$ for $NiTa_2O_6$ in various magnetic fields. (a) Field applied parallel to [110] lowers T_N as field strength increases. (b) Field applied parallel to [100] has less of an effect on T_N. (c) Field applied parallel to [001] has no effect on T_N.

the magnetic plane. The greatest shift occurs when $H \parallel [110]$. Unlike the previous example, however, only a single peak is observed for fields along this direction. This suggests there is no canting of the moments within the hard sublattice and that only the moments within the easy sublattice are affected by applied field. For $H \parallel [100]$, the moments of each sublattice are affected equally and the shift in T_N is about half that observed in the case of the easy sublattice for the same field strength. No appreciable shift is observed for $H \parallel [001]$.

Data for C_P in applied field are shown in Fig. 7.5a. When $H \parallel [001]$ (see inset of Fig. 7.5a), there is a single peak in C_P at T_N upon which application of field has little influence, as expected from $\partial M/\partial T$ data. Very different behavior is observed when $H \parallel [110]$. For $\mu_0 H > 2$ T, the single peak in C_P splits into two, with one peak remaining at $T_N(H = 0)$, and the other peak moving to lower T with the increase of

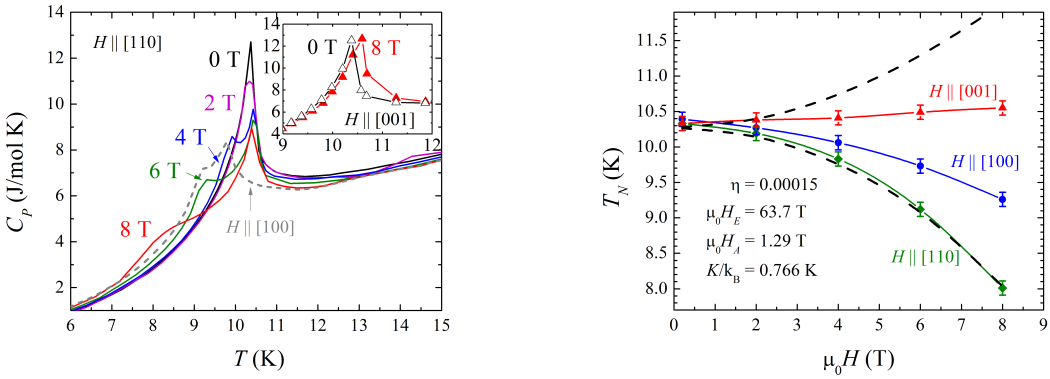

(a) In-field heat capacity C_P of $NiTa_2O_6$. (b) The field dependence of T_N for $NiTa_2O_6$

Figure 7.5: (a) The field dependence of C_P. Application along [110] results in a splitting of the peak into two, with one migrating to lower temperature with increasing field. The grey dotted curve is for $\mu_0 H = 8$ T parallel to [100]. Data with $H \parallel [001]$ is provided in the inset. (b) Néel temperature plotted as a function of external magnetic field for $H \parallel [100]$ (blue circles), $H \parallel [110]$ (green squares), and $H \parallel [001]$ (red triangles). The black dashed curves are fits from Eqs. 7.3 and 7.4 using the parameters in the lower left. Solid lines are guides for the eye.

H. At the same time, the original peak reduces in integrated intensity with the lost intensity emerging in the newly formed peak. The effect is identical for $H \parallel [1\bar{1}0]$ (data for this direction are not shown, for clarity). When C_P is measured at 8 T for $H \parallel [100]$ (grey dashed curve) a single, asymmetric peak is evident approximately midway between the two peaks in the $H \parallel [110]$ data. The peak's asymmetry is likely associated with misalignment of the suspended sample platform with respect to H. Law *et al.* [14] measured heat capacity in magnetic field on a polycrystalline sample of $NiTa_2O_6$ and observed the peak in C_P at T_N to smear out. In light of the observations herein, the behavior they observed is expected.

The positions of T_N were determined from both the heat capacity and magnetization data. The values of T_N associated with the easy sublattice when $H \parallel [110]$ are plotted in Fig. 7.5b along with those for $H \parallel [100]$ and $H \parallel [001]$. An attempt

was made to fit the data using Eqs. 7.3 and 7.4 (black dashed curves). The value of J was restricted to that obtained from the susceptibility fit in Section 4.2.2. The spin-flop field, $\mu_0 H = 12.8$ T, determined by Law *et al.* [14] was used to restrict H_A via the relation, $H_{SF} \approx \sqrt{2 H_E H_A}$. While the behavior of the data is similar to that of $NiSb_2O_6$, no combination of η or H_E was able to satisfy both fits simultaneously. The parameters shared between the two fits were therefore chosen such that data for $H \parallel [110]$ was successfully described by Eqs. 7.3. The resulting parameters are shown in the lower left of Fig. 7.5b. The anisotropy term corresponds to 66.0 μeV which, despite the imperfect fit of the $H \parallel [001]$ data, agrees well with the value 69.9 μeV suggested by the spin-flop analysis.

7.4 $CoSb_2O_6$

The derivative of magnetization data for $CoSb_2O_6$ in presented in Fig. 7.6. The behavior of the phase transition under applied magnetic field is similar to $NiTa_2O_6$. However, the shift of the peak in $CoSb_2O_6$ for $H \parallel [110]$ observed in Fig. 7.6a is about twice as great as the former two compounds under the same conditions. Such a large shift of the peak in $\partial M/\partial T$ allows for an interesting observation in the data with $\mu_0 H > 6$ T. In these two high-field cases, the peak is sufficiently removed from the region near $T_N(H = 0)$ and a small bump can be observed at this location. This feature is associated with the long-range order of the hard sublattice. Since this feature occurs at $T_N(H = 0)$, we can deduce that the application of field up to 8 T has no effect on the moments perpendicular to it. The data for $H \parallel [001]$ (i.e. when H is

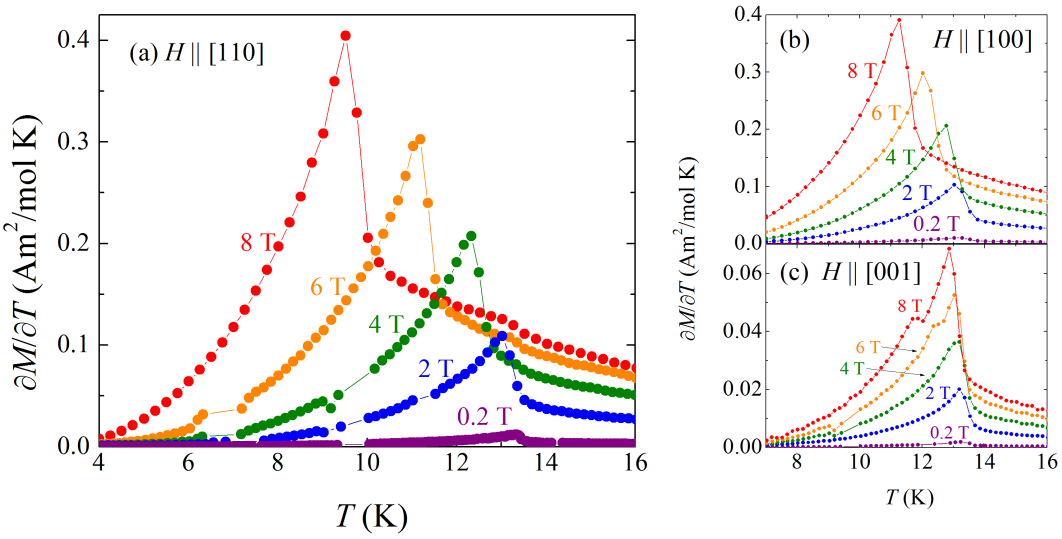

Figure 7.6: Derivative of magnetization with respect to temperature $\partial M/\partial T$ for $CoSb_2O_6$ in various magnetic fields. (a) Field applied parallel to [110] lowers T_N as field strength increases. (b) Field applied parallel to [100] has less of an effect on T_N. (c) Field applied parallel to [001] has no effect on T_N.

perpendicular to the moments of *both* sublattices) provided in Fig. 7.6c corroborates this assessment since no shift of the peak is apparent.

Heat capacity data for various applied fields are shown in Fig. 7.7a and are very similar to those of $NiTa_2O_6$. A single peak occurs at $T_N = 13.5$ K. When field is applied along [110] or [1$\bar{1}$0], a second peak associated with the easy sublattice emerges and migrates to lower temperature as field increases. The position of the original peak remains unaffected but the peak itself reduces in integrated intensity with the lost intensity emerging in the newly-formed peak. The peak associated with the easy sublattice is much more defined than that observed for $NiTa_2O_6$, indicating that moments undergo long-range order over a smaller temperature range in the present case. For $H \parallel [100]$ or $H \parallel [010]$ (latter not shown), we again observe a single asymmetric peak shifted to lower temperature by half the temperature shift of the

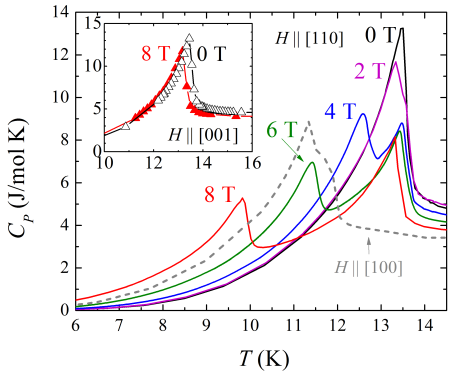

(a) In-field heat capacity C_P of $CoSb_2O_6$.

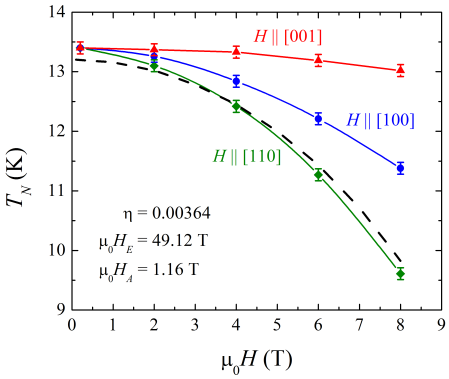

(b) The field dependence of T_N for $CoSb_2O_6$

Figure 7.7: (a) The field dependence of C_P. Application along [110] results in a splitting of the peak into two, with one migrating to lower temperature with increasing field. The grey dotted curve is for $\mu_0 H = 8$ T parallel to [100]. Data for $H \parallel [001]$ is provided in the inset. (b) Néel temperature plotted as a function of external magnetic field for $H \parallel [100]$ (blue circles), $H \parallel [110]$ (green squares), and $H \parallel [001]$ (red triangles). The black dashed curve is a fit from Eq. 7.3 using the parameters in the lower left. Solid lines are guides for the eye.

lower $H \parallel [110]$ peak under the same field strength. Data with $H \parallel [001]$ is shown in the inset. Applied field has little influence on the transition along this direction, in agreement with Fig. 7.6c. Since the magnetic moments lie in the a-b plane, and the magnetic exchange within the a-b plane is dominant [7, 14], there is minimal affect on the position or shape of the peak in C_P when $H \parallel [001]$.

The values of $T_N(H)$ have been determined from the peak positions in Figs. 7.6 and 7.7a. These values are plotted with respect to H in Fig. 7.7b. Because the peak associated with $H \parallel [001]$ does not increase with field, we are unable to use Eq. 7.4 to fit the data. We must rely, therefore, solely on Eq. 7.3 applied to the easy sublattice in order to extract information regarding the coupling ratio. The attempted fit (black dashed curve) using $|J|/k_B = 10.6$ K agrees very well with the data, yielding $\eta = 0.00364$. The values of the exchange and anisotropy fields suggest a

spin-flop transition occurs near 10.7 T. Although the PPMS used in our experiments is unable to achieve fields high enough to confirm this value, it seems reasonable in light of the slight deviation from linearity in $M(H)$ when $H \perp [001]$, which suggests a spin-flop above 9 T (see Fig. 4.8a).

7.5 $CoTa_2O_6$

Plots of $\partial M/\partial T$ for $CoTa_2O_6$ are shown in Fig. 7.8. Due to the spin-flop transition that occurs near 7 T, the curve for $\mu_0 H = 8$ T parallel to [110] lies *below* that for $\mu_0 H = 6$ T. The antiferromagnetic transition of the easy sublattice is disrupted as a portion of the moments become paramagnetic in the spin-flop configuration. The hard sublattice, on the other hand, remains mostly unaffected as indicated by the position of the small feature around $T_N(H = 0)$ for all curves with $H \parallel [110]$. As with the previous compounds, the shift of the peak when field is applied along either [100] or [010] is approximately half the amount observed for the easy sublattice when field is along either [110] or $[1\bar{1}0]$. Field applied along [001] results in a lowering of T_N by only a modest amount. The shift of T_N for fields along this direction is substantiated by heat capacity data (see below). This shift suggests that the magnetic structure contains a portion of anti-aligned moments with projections along the *c*-axis, as proposed by Reimers *et al.* [29] based upon powder neutron diffraction (see Section 1.3).

The heat capacity of $CoTa_2O_6$ for various applied magnetic fields is shown in Fig. 7.9a. The position of the peaks are in agreement with the peaks observed in $\partial M/\partial T$. Data for $H \parallel [010]$ are identical to those for $H \parallel [100]$ and are therefore omitted for clarity. The implication that there are moments with projections along

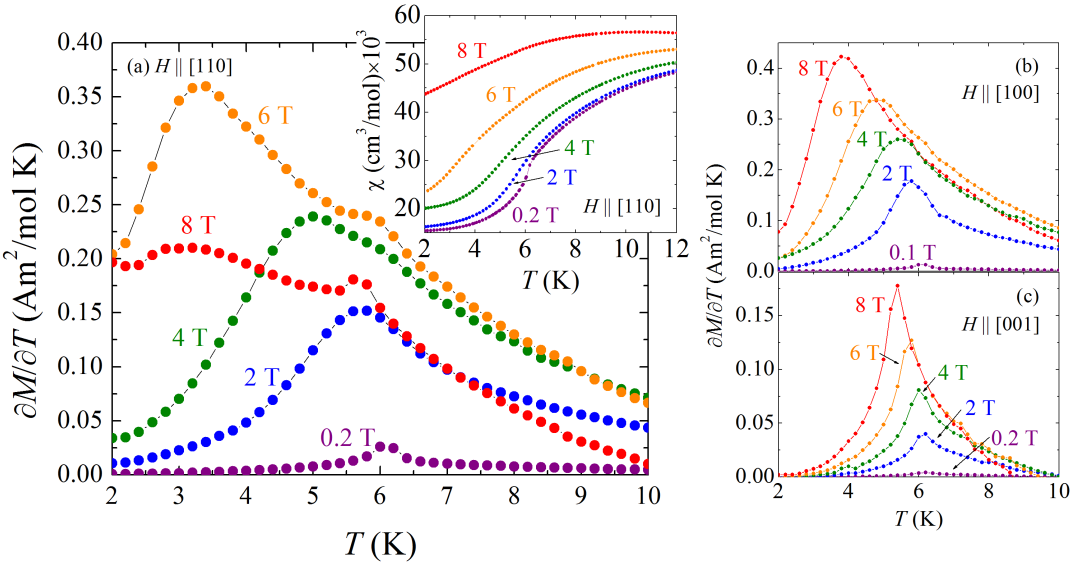

Figure 7.8: Derivative of magnetization with respect to temperature $\partial M/\partial T$ for $CoTa_2O_6$ for various magnetic fields. (a) Field applied parallel to [110] lowers T_N as field strength increases. The spin-flop near 8 T prohibits the rapid antiferromagnetic drop in χ upon cooling (see inset) and results in a lessening of the magnitude of $\partial M/\partial T$ below T_N for data acquired at that field. (b) $\partial M/\partial T$ for field applied parallel to [100]. This data is identical for $H \parallel [010]$, which is not shown. (c) $\partial M/\partial T$ for field applied parallel to [001].

the c-axis, which moreover are aligned antiferromagnetically, suggests a moderate interchain coupling along this direction. The presence of moments with projections along [001] may also account for the observation that the peak in magnetic susceptibility (see Fig. 4.3) is higher for $H \parallel [001]$ than when $H \perp [001]$, the opposite of that observed in the analogous compound $CoSb_2O_6$ where the moments are known to be constrained to the a-b plane.

The Néel temperature obtained from $\partial M/\partial T$ is plotted as a function of applied field in Fig. 7.9b. The easy sublattice data was fit using Eq. 7.3. The values of H_E and H_A were restricted to those obtained from the spin-flop analysis, while η and J were allowed to vary. The results are given in the lower left of Fig. 7.9b. The coupling,

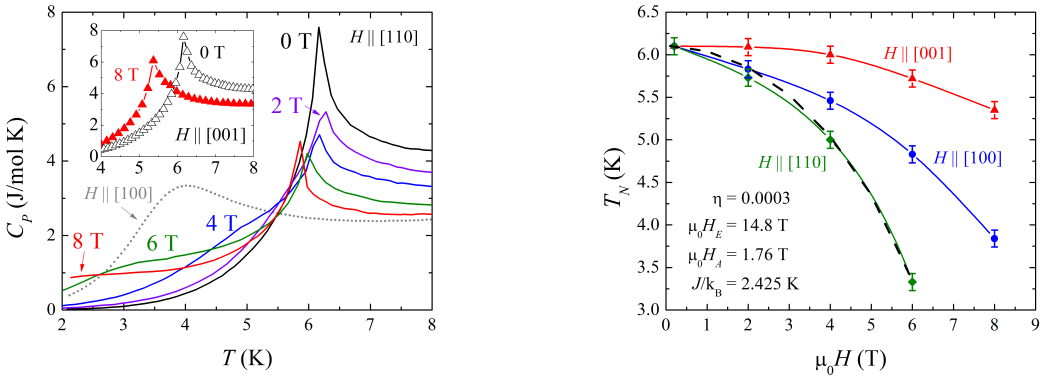

(a) In-field heat capacity C_P of $CoTa_2O_6$. (b) The field dependence of T_N for $CoTa_2O_6$

Figure 7.9: (a) The field dependence of C_P. Application along [110] results in the formation of an extended shoulder that migrates to lower temperature with increasing field. The grey dotted curve is for $\mu_0 H = 8$ T parallel to [100]. Data for $H \parallel [001]$ is provided in the inset. (b) T_N plotted as a function of external magnetic field for $H \parallel [100]$ (blue circles) and $H \parallel [110]$ (green squares). The black dashed curve is a fit from Eq. 7.3 using the parameters in the lower left. Solid lines are guides for the eye.

J/k_B, is comparable to 6.1 K determined from magnetic susceptibility in Section 4.2.3. The associated anisotropy energy, $K = 49.7$ μeV, is about half the value determined in Section 4.3.3. The value of η is on the order of 10^{-4}, suggesting the interplane coupling is small and that the chains are thoroughly isolated, as expected. However, similar fits can be obtained by varying both η and J from their aforementioned values and should therefore be considered with caution.

7.6 $FeTa_2O_6$

Plots of $\partial M/\partial T$ for $FeTa_2O_6$ in various applied fields is presented in Fig. 7.10. The application of field results in the lowering of T_N regardless of the direction. As expected, the greatest influence is when H is parallel to either [110] or [1$\bar{1}$0]. Under

this condition, we again observe a peak associated with the hard sublattice emerge near $T_N(H = 0)$. This feature is only weakly influenced by the applied field. The small amount of drift to lower temperature may be a result of sample misalignment. Just as with $CoTa_2O_6$, a lowering of T_N for $H \parallel [001]$ is observed. This shift is too large to be associated with sample misalignment. A report by Takano and Takada [12] concluded, based upon Mössbauer spectroscopy, that the ground state of $FeTa_2O_6$ consists of moments in a collinear antiferromagnetic arrangement angled 20° toward the c-axis. This would allow a field applied along [001] to have a moderate projection parallel to the moments, which may be sufficient to produce the effects observed in Fig. 7.10c. Recall from Section 4.2.4 that, just like the observations for $CoTa_2O_6$, the peak in the magnetic susceptibility is larger when $H \parallel [001]$ than when $H \perp [001]$ (see Fig. 4.4a), suggesting similarities in their magnetic structures.

In the inset of Fig. 7.10, the consequence of the spin-flop on the susceptibility data can be observed in the data for $\mu_0 H = 8$ T. The deflection upward upon cooling signifies the canting of magnetic moments along the direction of applied field. This results in the main-panel $\partial M/\partial T$ data for $\mu_0 H = 8$ T being almost entirely negative.

Specific heat measured in fields applied along various axes is presented in Fig. 7.11a. As expected, the peak associated with long-range order shifts to lower temperature with the increase of applied field. The position of the peaks when $H \parallel [001]$ and $H \parallel [110]$ agree with those observed in $\partial M/\partial T$. The data for $H \parallel [100]$, however, has unexpected behavior. Instead of a single shifted peak like that observed in the previous compounds, here we note features similar to the $H \parallel [110]$ data, namely both a peak and a low-temperature shoulder. At $\mu_0 H = 8$ T, the shifted peak is located near the same temperature as the $H \parallel [001]$ peak. Below about 4 K, the data is nearly indistinguishable from the $H \parallel [110]$ data, suggesting there exists a set of moments parallel to the a-axis. Data for $H \parallel [010]$ follows the same behavior as the

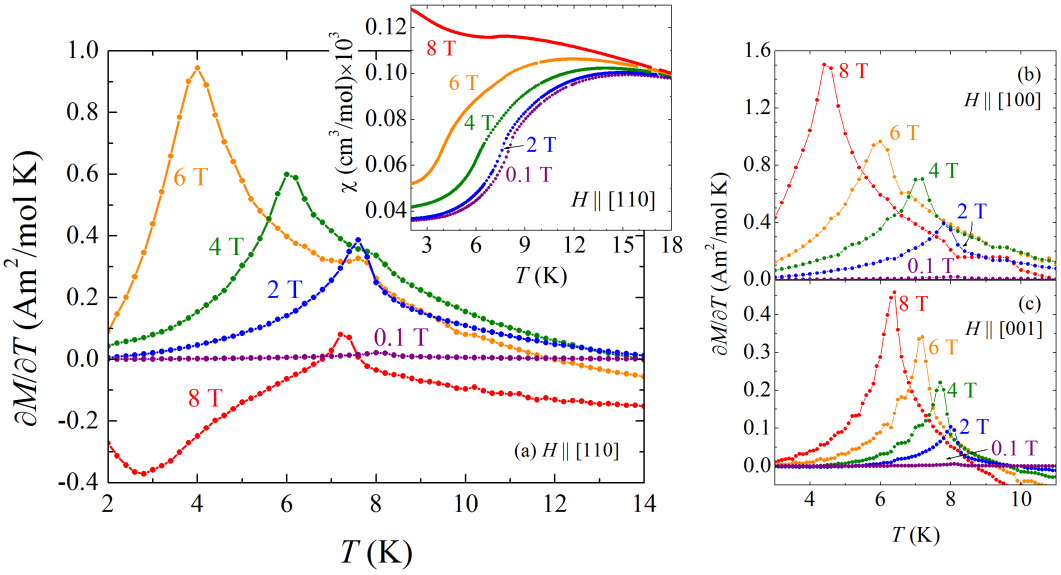

Figure 7.10: Derivative of magnetization with respect to temperature $\partial M/\partial T$ for $FeTa_2O_6$ for various magnetic fields. (a) Field applied parallel to [110] lowers T_N as field strength increases. The spin-flop at $\mu_0 H_{SF} = 7$ T prevents the antiferromagnetic drop in χ (see inset) and results in a lessening of the magnitude of $\partial M/\partial T$. (b) $\partial M/\partial T$ for field applied parallel to [100]. This data is identical to the set with $H \parallel [010]$, which is not shown. (c) $\partial M/\partial T$ for field applied parallel to [001].

data for $H \parallel [100]$. The shoulder that emerges from the peak when field is along either these two directions suggests that the moments are not solely along [110] or $[1\bar{1}0]$, but instead that there are additional sublattices with moments oriented along other directions. These observations are inconsistent with the proposed magnetic structures [12, 30]. The magnetic structure is clearly more complicated than the two-sublattice model shared by the other compounds. Neutron diffraction measurements on single crystals may be necessary to further deduce the precise magnetic structure.

The field dependence of the Néel temperature associated with moments in various applied field directions is shown in Fig. 7.11. An inflection point is observed at high field in the case of the easy sublattice with field applied along [110]. This is due to the spin-flop that occurs near 7 T. At $H = H_{SF}$, the internal field-dependent energy

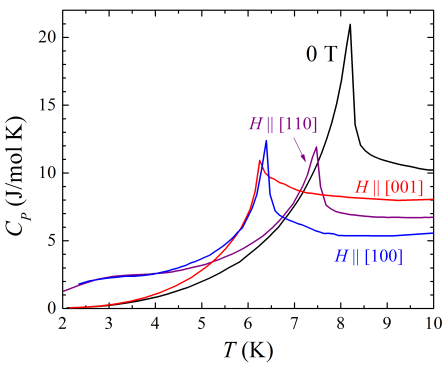

(a) Heat capacity of $FeTa_2O_6$ for 0 T and 8 T.

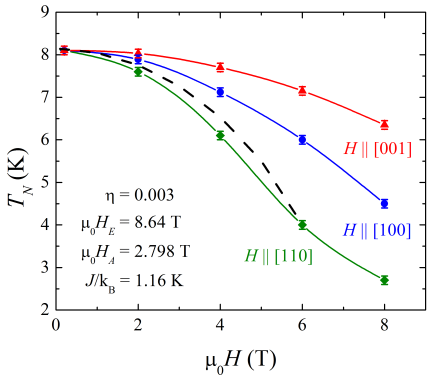

(b) The field dependence of T_N for $FeTa_2O_6$

Figure 7.11: (a) Plots of C_P for 0 T and 8 T. The sharp peak shifts to lower temperature for field applied along any direction, but is greatest for $H \parallel [100]$ and $H \parallel [001]$. Application of field perpendicular to [001] results in the formation of an extended shoulder that also migrates to lower temperature with increasing field. (b) Néel temperature plotted as a function of external magnetic field for H along various axes. The black dashed curve is a fit using Eq. 7.3, yielding the parameters in the lower left. Solid lines are guides for the eye.

balances the anisotropy energy and the Néel temperature reaches its lowest possible value. Above H_{SF}, the field acts to stabilize the moments in the spin-flop phase by increasing the effective anisotropy, allowing T_N to occur at a higher temperature [124]. The spin-flop field, therefore, marks a turn-around point of $T_N(H)$ and will thereafter increase with increasing field strength [121, 124, 128].

Just as with the cobalt compounds, the fact that there is a decrease, rather than an increase, in the Néel temperature with applied field disallows the use of Eq. 7.4. Therefore, Eq. 7.3 was used to fit the data for field parallel to the moments along [110] (see black dashed curve of Fig. 7.11b). The value of H_E was constrained to the value obtained from the spin-flop analysis, while the values of H_A, η, and J were allowed to vary. The results are arranged in the lower left corner of the figure.

7.7 Changes in Magnetic Entropy Due to Applied Magnetic Field

The observation that the integrated intensity of the peak in C_P associated with antiferromagnetic ordering shifts to lower temperature with application of H implies that there exists a change in magnetic entropy ΔS_m. This change can be evaluated by analyzing the C_P data. The entropy change over a specific temperature range at constant H is calculated from C_P using the well-known thermodynamic equation $T\mathrm{d}S = C_P\mathrm{d}T$. By solving for $\mathrm{d}S$ and integrating, we arrive at

$$\Delta S_T(H) = \int_{T_{\min}}^{T_{\max}} \left(\frac{C_P(T,H)}{T} \right) \mathrm{d}T. \tag{7.5}$$

The results from Eq. 7.5 are then used to determine the change in magnetic entropy $\Delta S_m(\Delta H) = \Delta S_T(H_2) - \Delta S_T(H_1)$ associated with the change in magnetic field $\Delta H = H_2 - H_1$. Beginning the integration of Eq. 7.5 at the lowest measurement temperature $T_{\min}$, and terminating at any finite temperature $T_{\max} > T_{\min}$, allows determination of $\Delta S_m(T, \Delta H)$.

The magnetic entropy change can also be calculated using magnetization data. This can be appreciated through the Maxwell relation

$$\left(\frac{\partial M}{\partial T} \right)_H = \frac{1}{\mu_0} \left(\frac{\partial S}{\partial H} \right)_T \tag{7.6}$$

which is derived in Section 3.3.1. The change in S_m associated with a change in H is determined by integrating Eq. 7.6 to obtain

$$\Delta S_m = \mu_0 \int_0^{H_{\max}} \left(\frac{\partial M}{\partial T} \right)_H \mathrm{d}H \tag{7.7}$$

In practice, Eq. 7.7 is used to determine $\Delta S_m(T, \Delta H)$ at any temperature T for a field change $\Delta H = H_2 - H_1$. Note that H_1 here is small but nonzero, since a finite H is required to measure M.

Both methods of determining ΔS_m have been implemented on $Ni(Sb,Ta)_2O_6$, $Co(Sb,Ta)_2O_6$, and $FeTa_2O_6$ and are in remarkable agreement. The results are shown in Fig. 7.12. The set of fields used for magnetization data contain $\mu_0 H = 0.1$, 2.0, 4.0, 6.0, and 8.0 T. Data obtained from Eq. 7.7 can sometimes display multiple peaks when the full-width half-max is large and the discrete set of fields does not contain enough field values to make the ΔS_m curve appear smooth. Such is the case for $CoSb_2O_6$ and $FeTa_2O_6$ when field is along [110]. All curves saturate to zero for temperatures far away from T_N.

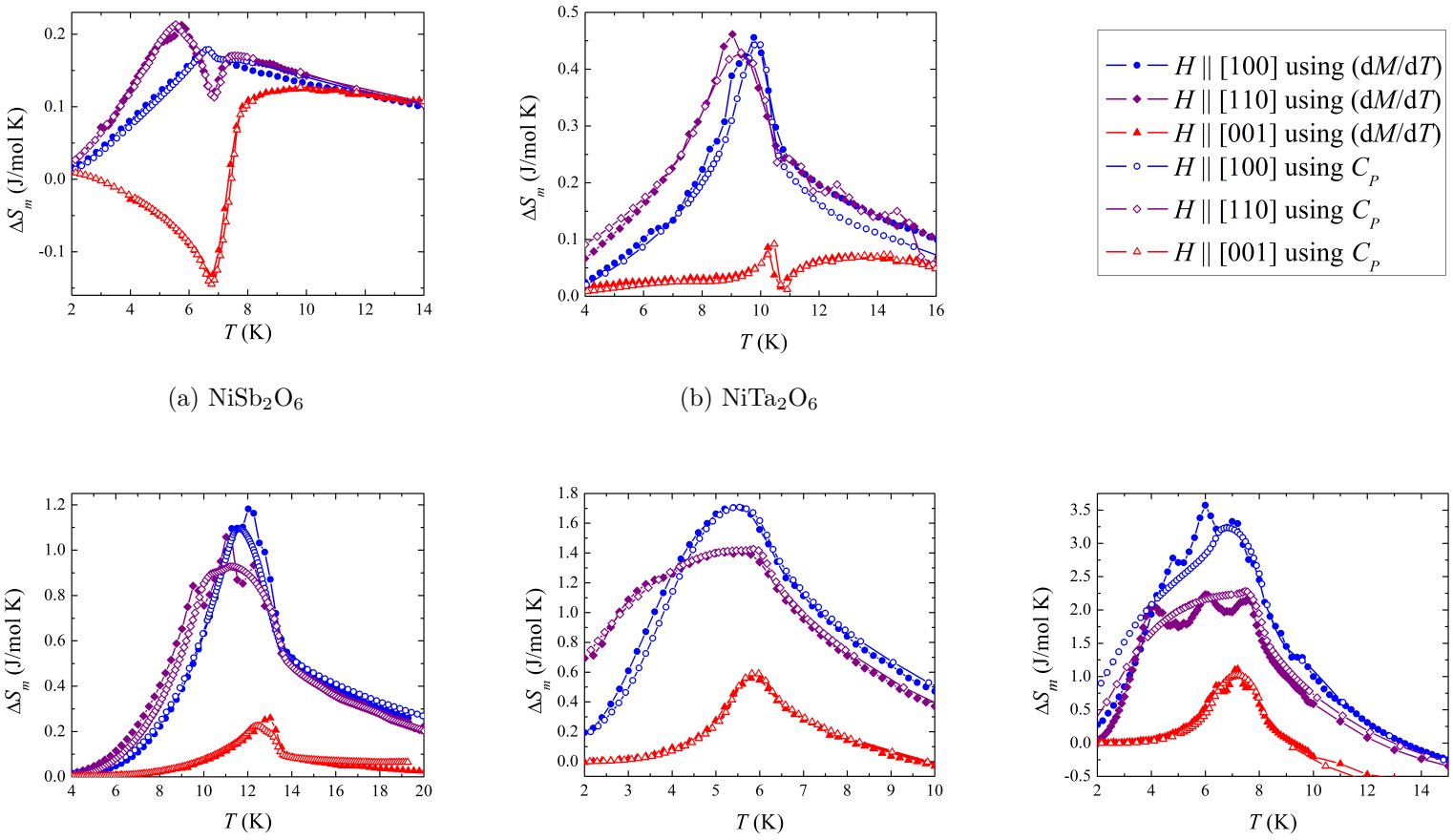

(a) $NiSb_2O_6$ (b) $NiTa_2O_6$

(c) $CoSb_2O_6$ (d) $CoTa_2O_6$ (e) $FeTa_2O_6$

Figure 7.12: Change in magnetic entropy due to applied magnetic field $\mu_0 H_{max} = 8$ T for $M(\mathrm{Sb,Ta})_2O_6$. Curves with filled data points are determined through the use of Eq. 7.7. Curves with open data points are determined through Eq. 7.5. Blue, purple, and red curves are for fields applied parallel to [100], [110], and [001], respectively. Data for field applied along [010] ($[1\bar{1}0]$) are identical to data for field applied along [100] ([110]) and are therefore not shown.

Table 7.1: The Relative Cooling Power of $M(\mathrm{Sb,Ta})_2\mathrm{O}_6$ in units of J/mol.

	$NiSb_2O_6$	$NiTa_2O_6$	$CoSb_2O_6$	$CoTa_2O_6$	$FeTa_2O_6$
$H \parallel [110]$	-2.13	-1.63	-4.66	-8.29	-11.3
$H \parallel [100]$	-1.57	-1.31	-4.12	-7.47	-17.2
$H \parallel [001]$	0.217	-0.06	-0.44	-1.13	-2.07

The ΔS_m peaks are broadest when field is applied parallel to the magnetic moments. This is expected since it is under this condition that the shift in T_N is greatest. Minor changes in magnetic entropy are observed for fields parallel to [001] for all compounds save $NiSb_2O_6$, in which a large negative change is observed. Recall from Fig. 4.2 that the magnetization increases upon cooling when field is applied along [001] for $T < T_N$. The derivative $\mathrm{d}M/\mathrm{d}T$ is therefore negative, resulting in negative values for ΔS_m in Eq. 7.7. This is reminiscent of common ferromagnetic magnetocaloric materials which also show a dip in ΔS_m and whose transition temperatures increase with field [129]. This suggests that a small amount of ferromagnetism is caused by the canting of moments in $NiSb_2O_6$ when field is applied along the hard axis.

An important quantity in many MCE investigations is the Relative Cooling Power (RCP) of a sample, which provides an easy method of comparing against other materials. This quantity is given by $RCP = -\int \Delta S_m(T) dT$. We can approximate this value by multiplying the height of the $\Delta S_m(T)$ peak by its width, ΔT, at half-max. The negative sign is introduced to indicate the lowering of energy with field. The results are given in Table 7.1. These quantities are about two orders of magnitude smaller than gadolinium-based materials [129] which are the most widely used MCE compounds. Although the values here cannot compete with those of other thoroughly studied materials for large-scale cooling, the $M(\mathrm{Sb,Ta})_2\mathrm{O}_6$ compounds may still have applications in small-scale systems operating near liquid-helium temperatures.

7.8 Changes in Temperature Due to Applied Magnetic Field

To obtain a complete evaluation of the magnetocaloric effect, we must discuss the change in sample temperature in response to an applied magnetic field. Direct measurements of the sample temperature can be performed using either contact or non-contact techniques depending upon the experimental setup. However, direct measurement of ΔT due solely to application of magnetic field (as opposed to temperature drifts due to environmental fluctuations) is challenging for a number of reasons. The main difficulty is that a rapid change in magnetic field is needed. The PPMS used in these experiments can only achieve a maximum field rate of 200 Oe/sec, which is too slow considering a magnetocaloric effect is not observed in these compounds until about 40 kOe. We must therefore determine the change in temperature indirectly through the use of other thermodynamic quantities. Using the Maxwell relation given by Eq. 7.6, we may derive (see Section 3.3.2) the expression

$$\Delta T = -\mu_0 \int_0^{H_{\max}} \left(\frac{T}{C(T,H)} \right) \left(\frac{\partial M}{\partial T} \right) \Big|_H \mathrm{d}H \tag{7.8}$$

where $\mathrm{d}M/\mathrm{d}T$ is the derivative of the magnetization and $C(T,H)$ is the total heat capacity measured in a constant field H. This expression has been applied to the previous five compounds which exhibit a magnetocaloric effect. The results are shown in Fig. 7.13. All samples show a lowering of temperature when magnetic field is applied near T_N. (Two exceptions are observed in the case of the two nickle compounds when $H \parallel [001]$. These results ultimately stem from the fact that the transition temperatures rise for these two compounds when the moments are perpendicular to the field.) In general, curves for H applied within the magnetic plane agree above T_N and bifurcate below, with field along the chain directions providing the largest change

in temperature. All curves tend toward $\Delta T = 0$ K for temperatures adequately above T_N.

The large anisotropy observed in ΔT between curves for $H \parallel [001]$ and $H \parallel [110]$ has possible industrial applications. The data suggests that simply rotating the crystal in a constant magnetic field of 8 T from an orientation in which H is along [001] to one with H along [110] will cool the sample by about 1-4 K, depending upon the chosen crystal. The crystal could therefore be used in environmentally-friendly magnetic refrigeration systems which could replace traditional methods that involve pumping on potentially hazardous refrigerants. However, the operating temperature and amount of cooling power makes these compounds best suited for cryogens near 10 K and where only small volumes are required.

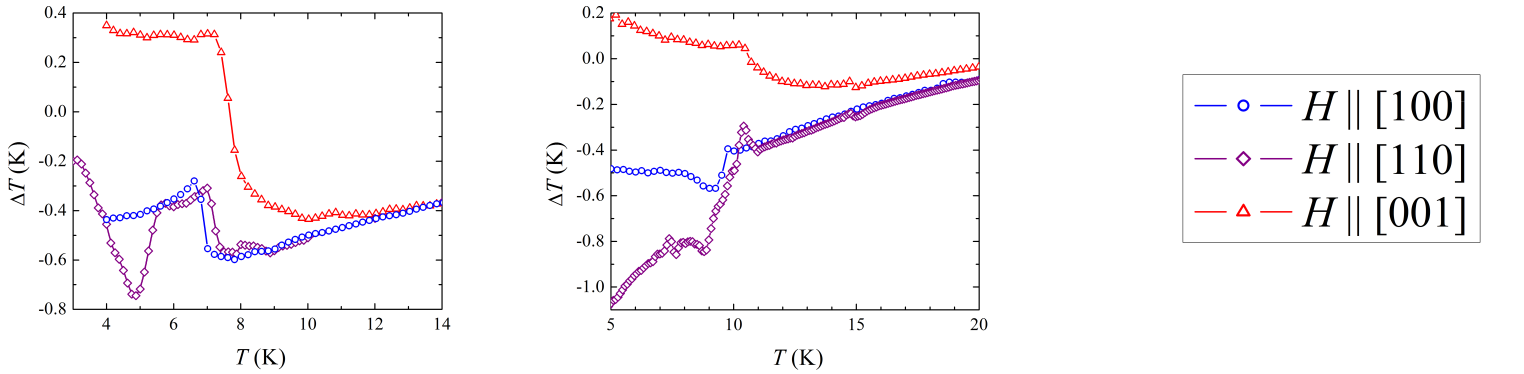

(a) $NiSb_2O_6$ (b) $NiTa_2O_6$

(c) $CoSb_2O_6$ (d) $CoTa_2O_6$ (e) $FeTa_2O_6$

Figure 7.13: Temperature dependence of the adiabatic temperature change due to applied magnetic field $\mu_0 H = 8$ T for $M(\mathrm{Sb,Ta})_2O_6$. Curves with blue circles, purple diamonds, and red triangles indicate cases with $H \parallel [100]$, $H \parallel [110]$, and $H \parallel [001]$ respectively. Curves are determined through the use of Eq. 7.8.

7.9 Discussion

In this chapter, we have examined the behavior of magnetization and heat capacity in response to the application of considerable magnetic fields. These observations have contributed to the understanding of the magnetic structures of the $M(\mathrm{Sb,Ta})_2\mathrm{O}_6$ compounds. The data for $\mathrm{Ni(Sb,Ta)_2O_6}$ and $\mathrm{CoSb_2O_6}$ are consistent with the two sublattice magnetic structure discussed in Section 1.3 and with the band structure calculations reported by Law *et al* [14]. The moments appear to be constrained to the *a*-*b* plane, as expected. The extremely weak coupling between the sublattices in the quasi 1-d magnetic solids leads to the presence of two antiferromagnetic transitions when the magnetic field H is parallel to the quasi 1-d chains of one lattice and perpendicular to the those of the other.

The data for $\mathrm{CoTa_2O_6}$ and $\mathrm{FeTa_2O_6}$ are similar to those of the previous compounds, but furthermore suggest that these two compounds contain sets of magnetic moments with modest projections along the *c*-axis. These results are in accordance with the conclusions drawn by Reimers *et al.* [29] and Takano and Takada [12] but disagree with those of Kinast *et al* [32]. While the current study has corroborated the findings of the former two reports, these conflicting interpretations reinforce the need for neutron diffraction measurements performed on single crystals.

Let us now address the issue as to why some changes in T_N are positive while the majority are negative. The lowering of T_N with field is a common trait among many antiferromagnets and is generally ascribed to the increase in magnetic entropy through the destabilization of the moments [130]. An *increase* in T_N is much less common in AFM materials and requires a closer inspection. Turning our attention to Eq. 7.1 can provide a better understanding. As mentioned previously, magnetic fields

which satisfy this inequality can reduce the dimensionality of the spin chains. Many of the spin chains in this study have been shown to exhibit Heisenberg behavior. A Heisenberg system, which has a spin dimensionality $D = 3$, is therefore afforded the opportunity to decrease its dimensionality with the application of magnetic field. A reduction to an XY ($D = 2$) or Ising ($D = 1$) system would increase the correlation length and, in turn, T_N. This mechanism may be responsible for the increase of T_N observed in $Ni(Sb,Ta)_2O_6$ when $H \parallel [001]$. In the antimonate compound, this increase is clear and has been analyzed above. The tantalate compound, however, displays only a minor increase in T_N (about 0.22 K) when $\mu_0 H = 8$ T. $NiTa_2O_6$ was determined in Section 4.2.2 to be a Heisenberg system with effective moment around $3.26\mu_B$ per Ni^{2+} ion. Using this moment value and $T = 10.3$ K we find that the left side of Eq. 7.1 is not satisfied until $\mu_0 H \approx 5$ T. Thus, according to this theory, larger fields are necessary in order to observe appreciable changes.

No increase in T_N is observed for any other members of the antimontates or tantalates. Recall that for $Co(Sb,Ta)_2O_6$ and $FeTa_2O_6$, the spin chains were determined to be Ising-like using fits to χ, specific heat, and critical exponent analysis [11, 13, 30, 89]. Their dimensionality, therefore, cannot be reduced any further, preventing the opportunity to increase the correlation length. In the case of either $CuSb_2O_6$ or $MnSb_2O_6$, neither an increase nor decrease in T_N is observed. This is due to the fact that both compounds exhibit spin-flop transitions at relatively low fields (~ 1.25 T and ~ 0.94 T, respectively). Both spin-flop field values are much lower than those necessary to satisfy Eq. 7.1. This means that neither compound is able to take advantage of the applied magnetic field (in regards to raising or lowering T_N) before a new magnetic configuration is established.

8. CONCLUSIONS

In this study we have investigated the magnetic and thermal properties of single-crystalline $M(\mathrm{Sb,Ta})_2\mathrm{O}_6$ compounds. Magnetic interactions along M-O-O-M chains have been determined to be Heisenberg-like for $\mathrm{CuSb_2O_6}$, $\mathrm{Ni(Sb,Ta)_2O_6}$, and $\mathrm{MnSb_2O_6}$ while those of $\mathrm{Co(Sb,Ta)_2O_6}$ and $\mathrm{FeTa_2O_6}$ have been shown to be Ising-like. The use of single-crystalline samples has offered a distinct advantage over powder samples by allowing the measurements to be conducted along individual axes. The two-sublattice antiferromagnetic structure exhibited by $\mathrm{Ni(Sb,Ta)_2O_6}$ and $\mathrm{CoSb_2O_6}$; and the more complex structures of $\mathrm{CoTa_2O_6}$ and $\mathrm{FeTa_2O_6}$, exhibit particularly interesting properties due to the 90° rotation of the neighboring M-O-O-M chains along the c-axis. The unusual magnetic structures are responsible for the anisotropy observed in magnetization and thermal expansion measurements, as well as in-field heat capacity. By identifying and analyzing this anisotropy, we have gained insight into the behavior of the inter- and intrachain couplings that dictate the low-dimensionality of these systems.

Various measurements provided herein have shown a crossover from one- to three-dimensional antiferromagnetic behavior that occurs at low temperature for each compound. Above this transition, broad peaks in magnetic susceptibility of the trirutile compounds indicate that short-range order manifests as the partial ordering of clusters of moments along the chains. The broad peaks with $H \perp [001]$ typically occur at the same temperature as that with $H \parallel [001]$, typical of Heisenberg systems. Exceptions occur for $\mathrm{Co(Sb,Ta)_2O_6}$ and $\mathrm{FeTa_2O_6}$, which show the maxima with $H \parallel [001]$ located at lower temperatures due to Ising anisotropy. In general, these broad peaks occur at higher temperatures in the antimonates than in the tantalates, suggesting that

short-range order is more prevalent in the former compounds. The exchange coupling, J/k_B, related to the temperatures at which the broad peaks occur was found to depend exponentially on the ratio $R_{ion}/D_{M\text{-O}}$, revealing that the coupling is highly sensitive to the amount of orbital overlap between ions.

At the Néel temperature, individual clusters of ordered spins combine to form long-range order evidenced by the rapid drop in $\chi(T)$ upon cooling and the accompanying peak in heat capacity at the same temperature. However, residual entropy suggests that the structures contain partially disordered regions even at the lowest temperatures measured. At T_N, the magnetic structure therefore contains a mixture of Néel, short-range order, and disordered (spin-liquid) states.

It has been thoroughly shown that the magnetic order at T_N can be disrupted by magnetic fields above 2 T, corresponding to an energy on the order of 0.5 meV. The fact that the application of field can influence the transition temperature leads to a magnetocaloric effect that is highly anisotropic by virtue of the low-dimensional nature of the antiferromagnetism. Although the effect is modest in magnitude, the directional dependence indicates that the rotation of single crystals in a constant magnetic field would cause the sample temperature to change. The MCE reported herein differs from that observed [131] and theoretically studied [132, 133, 134, 135] for low-dimensional quantum-spin systems, where saturation to a fully-polarized magnetic system is responsible. The directional dependence of the MCE displayed by these low-dimensional compounds has potentially useful applications. Normally in magnetocaloric systems, heat is removed through a multiple-step process that involves applying a magnetic field to a material followed by a reduction of the field either by discharging an electromagnet or removing the material from the field source. If, however, a single-crystalline sample chosen from Table 7.1 was used as the magnetocaloric material, neither of these field-reduction methods would be necessary. While

the comparatively small Relative Cooling Power cannot compete with gadolinium-based materials for large-scale cooling, the low-dimensional compounds may have applications in small-scale systems operating near liquid-helium temperatures.

8.1 Future Perspectives

The compounds studied herein have been stoichiometric with only one magnetic ion per chemical formula unit. An interesting pursuit, therefore, would be to investigate the anisotropy and possible magnetocaloric effect of mixed compounds. For example, $Co_{1-x}Ni_xSb_2O_6$, where x is between 0 and 1, may display traits similar to both $CoSb_2O_6$ and $NiSb_2O_6$. The introduction of Ni to the cobalt antimonate might increase the RCP due to the increase in T_N associated with the Ni moments perpendicular to the applied field. Furthermore, the diamagnetic ion could be replaced as well. Earlier studies of the niobates, MNb_2O_6, for example, have also displayed low-dimensional behavior with Néel temperatures as high as 14 K, as in the case of $NiNb_2O_6$ [136]. This substitution would provide a host of new materials to investigate in terms of the anisotropic magnetocaloric effect.

One may never be certain of the merits of research. When asked by the layman, "What good is any of this?" The response that it "contributes to the understanding of magnetic interactions of low-dimensional spin systems" is often, to them, unsatisfying. The anisotropic magnetocaloric effect is an elegant phenomenon of these compounds, but the low operating temperatures and modest effect may currently have limited real-world applications. Therefore, I leave the reader to reflect on Kroemer's Lemma of New Technology [137] which states, "The principal applications of any sufficiently new and innovative technology always have been–and will continue to be–applications *created* by that technology."

APPENDIX

CRYSTALLOGRAPHIC PARAMETERS

Table A.1: Crystallographic Parameters for $ZnSb_2O_6$ at Room Temperature [138].

Space group	a [Å]	c [Å]	
$P4_2/mnm$	4.6638(4)	9.263(1)	Z = 2
Atom	x	y	z
Zn	0	0	0
Sb	0	0	0.3322(1)
O_1	0.315(1)	0.315(1)	0
O_2	0.304(2)	0.304(2)	0.325(1)

Table A.2: Crystallographic Parameters for $CuSb_2O_6$ at Room Temperature. Crystal structure is monoclinic with $\beta = 91.124(2)$ [139].

Space group	a [Å]	b [Å]	c [Å]
$P2_1/n$	4.6349(1)	4.6370(1)	9.2931(1)
Atom	x	y	z
Cu	0	0	0
Sb	0.0011(9)	0.0080(10)	0.3338(6)
O_1	0.3130(9)	0.2983(8)	0.0017(4)
O_2	0.2991(8)	0.3176(7)	0.3291(4)
O_3	-0.3012(8)	-0.2915(9)	0.3248(4)

Table A.3: Crystallographic Parameters for $NiSb_2O_6$ at Room Temperature [28].

Space group	a [Å]	c [Å]	
$P4_2/mnm$	4.62957(7)	9.19811(20)	Z = 2
Atom	x	y	z
Ni	0	0	0
Sb	0	0	0.3333(10)
O_1	0.3107(10)	0.3107(10)	0
O_2	0.3021(6)	0.3021(6)	0.3270(5)

Table A.4: Crystallographic Parameters for $NiTa_2O_6$ [140].

Space group	a [Å]	c [Å]	
$P4_2/mnm$	4.7219(11)	9.150(5)	Z = 2
Atom	x	y	z
Ni	0	0	0
Sb	0	0	0.3316(3)
O_1	0.307(8)	0.307(8)	0
O_2	0.297(6)	0.297(6)	0.327(4)

Table A.5: Crystallographic Parameters for $CoSb_2O_6$ at Room Temperature [29].

Space group	a [Å]	c [Å]	
$P4_2/mnm$	4.6495(2)	9.2763(6)	Z = 2
Atom	x	y	z
Co	0	0	0
Sb	0	0	0.3358(9)
O_1	0.3082(9)	0.3082(9)	0
O_2	0.3026(5)	0.3026(5)	0.3264(5)

Table A.6: Crystallographic Parameters for $CoTa_2O_6$ at Room Temperature [29].

Space group	a [Å]	c [Å]	
$P4_2/mnm$	4.7358(3)	9.1708(7)	Z = 2
Atom	x	y	z
Co	0	0	0
Sb	0	0	0.3304(4)
O_1	0.3109(7)	0.3109(7)	0
O_2	0.2967(4)	0.2967(4)	0.3255(4)

Table A.7: Crystallographic Parameters for $FeTa_2O_6$ at Room Temperature [141].

Space group	a [Å]	c [Å]	
$P4_2/mnm$	4.7595(5)	9.2001(2)	Z = 2
Atom	x	y	z
Fe	0	0	0
Ta	0	0	0.3308(1)
O_1	0.2938(10)	0.2938(10)	0.3229(6)
O_2	0.3125(14)	0.3125(14)	0

Table A.8: Crystallographic Parameters for $MnSb_2O_6$ at Room Temperature [142].

Space group	a [Å]	b [Å]	c [Å]
P3	8.8056(1)	8.8056(1)	4.7232(1)
Atom	x	y	z
Mn	0.0001	0.63166	0.5067
Sb_1	0.69557(3)	0.69557(3)	0.00681(8)
Sb_2	0.66667(0)	0.33333(0)	0.00000(0)
Sb_3	0.00000(0)	0.00000(0)	0.5069(1)
Sb_4	0.33333(0)	0.66667(0)	0.0137(1)
O_1	0.7752(3)	0.5545(3)	0.2264(7)
O_2	0.4721(4)	0.5894(4)	0.2361(7)
O_3	0.7876(4)	0.8963(4)	0.2715(8)
O_4	0.8920(4)	0.1044(4)	0.7451(8)
O_5	0.8815(4)	0.4091(4)	0.7797(7)
O_6	0.5545(4)	0.7747(4)	0.7908(8)

REFERENCES CITED

[1] Lenz, W., Beitrag zum Verständnis der magnetischen Erscheinungen in festen Körpern, *Physikalische Zeitschrift*, **21**, 613 (1920).

[2] Ising, E., *Beitrag zur Theorie des Ferro-und Paramagnetismus*, Ph.D. thesis, University of Hamburg (1924).

[3] Peierls, R., On Ising's model of ferromagnetism, *Mathematical Proceedings of the Cambridge Philosophical Society*, **32**(3), 477 (1936).

[4] Nix, F. C. and Shockley, W., Order-Disorder Transformations in Alloys, *Rev. Mod. Phys.*, **10**, 1 (1938).

[5] Fowler, R. H., Adsorption isotherms. Critical conditions, *in Mathematical Proceedings of the Cambridge Philosophical Society*, volume 32, pp. 144–151, Cambridge University Press (1936).

[6] Brush, S. G., History of the Lenz-Ising Model, *Rev. Mod. Phys.*, **39**, 883 (1967).

[7] Kasinathan, D., Koepernik, K., and Rosner, H., Quasi-One-Dimensional Magnetism Driven by Unusual Orbital Ordering in $CuSb_2O_6$, *Phys. Rev. Lett.*, **100**, 237202 (2008).

[8] Kato, M., Kajimoto, K., Yoshimura, K., Kosuge, K., Nishi, M., and Kakurai, K., Magnetic Structure of $CuSb_2O_6$, *Journal of the Physical Society of Japan*, **71**(Suppl), 187 (2002).

[9] Rebello, A., Smith, M. G., Neumeier, J. J., White, B. D., and Yu, Y.-K., Transition from one-dimensional antiferromagnetism to three-dimensional antiferromagnetic order in single-crystalline $CuSb_2O_6$, *Phys. Rev. B*, **87**, 224427 (2013).

[10] Kremer, R. K. and Greedan, J. E., Magnetic ordering in $CoTa_2O_6$ and $NiTa_2O_6$, *Journal of Solid State Chemistry*, **73**(2), 579 (1988).

[11] Christian, A. B., Rebello, A., Smith, M. G., and Neumeier, J. J., Local and long-range magnetic order of the spin $-\frac{3}{2}$ system $CoSb_2O_6$, *Phys. Rev. B*, **92**, 174425 (2015).

[12] Takano, M. and Takada, T., Magnetic properties of MTa_2O_6 (M = Fe, Co or Ni), *Materials Research Bulletin*, **5**(6), 449 (1970).

[13] Kremer, R. K., Greedan, J. E., Gmelin, E., Dai, W., White, M. A., Eicher, S. M., and Lushington, K. J., Specific Heat of MTa_2O_6 (M = Co, Ni, Fe, Mg) Evidence for Low Dimensional Magnetism, *J. Phys. Colloques*, **49**(8), 1495 (1988).

[14] Law, J. M., Koo, H.-J., Whangbo, M.-H., Brücher, E., Pomjakushin, V., and Kremer, R. K., Strongly correlated one-dimensional magnetic behavior of $NiTa_2O_6$, *Phys. Rev. B*, **89**, 014423 (2014).

[15] Christian, A. B., Masunaga, S. H., Schye, A. T., Rebello, A., Neumeier, J. J., and Yu, Y.-K., Magnetic field influence on the Néel, dimer, and spin-liquid states of the low-dimensional antiferromagnets $NiTa_2O_6$ and $CoSb_2O_6$, *Phys. Rev. B*, **90**, 224423 (2014).

[16] Pytte, E., Lattice distortions in one-dimensional Ising chains, *Phys. Rev. B*, **10**, 2039 (1974).

[17] Cross, M. C. and Fisher, D. S., A new theory of the spin-Peierls transition with special relevance to the experiments on TTFCuBDT, *Phys. Rev. B*, **19**, 402 (1979).

[18] Rice, M. J. and Strässler, S., Effects of fluctuations and interchain coupling on the peierls transition, *Solid State Communications*, **13**(9), 1389 (1973).

[19] Haldane, F. D. M., Spontaneous dimerization in the S=1/2 Heisenberg antiferromagnetic chain with competing interactions, *Phys. Rev. B*, **25**, 4925 (1982).

[20] Earnshaw, A., *Introduction to Magnetochemistry*, Academic Press Inc., London (1968).

[21] Jahn, H. A. and Teller, E., Stability of polyatomic molecules in degenerate electronic states. I. Orbital degeneracy, *in Proceedings of the Royal Society of London A: Mathematical, Physical and Engineering Sciences*, volume 161, pp. 220–235, The Royal Society (1937).

[22] Heinrich, M., von Nidda, H.-A. K., Krimmel, A., Loidl, A., Eremina, R. M., Ineev, A. D., Kochelaev, B. I., Prokofiev, A. V., and Assmus, W., Structural and magnetic properties of $CuSb_2O_6$ probed by ESR, *Phys. Rev. B*, **67**, 224418 (2003).

[23] Opel, M., Spintronic oxides grown by laser-MBE, *Journal of Physics D: Applied Physics*, **45**(3), 033001 (2012).

[24] Whangbo, M.-H., Koo, H.-J., Dai, D., and Jung, D., Interpretation of the Magnetic Structures of $Cu_2Te_2O_5X_2$ (X = Cl, Br) and $Ca_{3.1}Cu_{0.9}RuO_6$ on the Basis of Electronic Structure Considerations: Cases for Strong Super-Superexchange Interactions Involving Cu^{2+} Ions, *Inorganic Chemistry*, **42**(12), 3898 (2003), pMID: 12793828.

[25] Nakua, A. and Greedan, J., Confirmation of Long-Range Magnetic Order in $CuSb_2O_6$, *Journal of Solid State Chemistry*, **118**(1), 199 (1995).

[26] Gibson, B. J., Kremer, R. K., Prokofiev, A. V., Assmus, W., and Ouladdiaf, B., Elastic neutron diffraction study of long-range antiferromagnetic order in the S=1/2 quantum chain system $CuSb_2O_6$, *Journal of Magnetism and Magnetic Materials*, **272276, Part 2**(0), 927 (2004), proceedings of the International Conference on Magnetism (ICM 2003).

[27] da Silva Wheeler, E. M., *Neutron scattering from low-dimensional quantum magnets*, Ph.D. thesis, Oxford University (2007).

[28] Ehrenberg, H., Wltschek, G., Rodriguez-Carvajal, J., and Vogt, T., Magnetic structures of the tri-rutiles $NiTa_2O_6$ and $NiSb_2O_6$, *Journal of Magnetism and Magnetic Materials*, **184**(1), 111 (1998).

[29] Reimers, J. N., Greedan, J. E., Stager, C. V., and Kremer, R., Crystal Structure and Magnetism in $CoSb_2O_6$ and $CoTa_2O_6$, *Journal of Solid State Chemistry*, **83**, 20 (1989).

[30] Eicher, S. M., Greedan, J. E., and Lushington, K. J., The magnetic properties of $FeTa_2O_6$. Magnetic structure and low-dimensional behavior, *Journal of Solid State Chemistry*, **62**(2), 220 (1986).

[31] Kinast, E. J., Antonietti, V., Schmitt, D., Isnard, O., da Cunha, J. B. M., Gusmão, M. A., and dos Santos, C. A., Bicriticality in $Fe_xCo_{1-x}Ta_2O_6$, *Phys. Rev. Lett.*, **91**, 197208 (2003).

[32] Kinast, E., dos Santos, C., Schmitt, D., Isnard, O., Gusmo, M., and da Cunha, J., Magnetic structure of the quasi-two-dimensional compound $CoTa_2O_6$, *Journal of Alloys and Compounds*, **491**(12), 41 (2010).

[33] Johnson, R. D., Cao, K., Chapon, L. C., Fabrizi, F., Perks, N., Manuel, P., Yang, J. J., Oh, Y. S., Cheong, S.-W., and Radaelli, P. G., $MnSb_2O_6$: A Polar Magnet with a Chiral Crystal Structure, *Phys. Rev. Lett.*, **111**, 017202 (2013).

[34] Reimers, J., Greedan, J., and Subramanian, M., Crystal structure and magnetism in $MnSb_2O_6$: Incommensurate long-range order, *Journal of Solid State Chemistry*, **79**(2), 263 (1989).

[35] Kinoshita, M., Seki, S., Sato, T. J., Nambu, Y., Hong, T., Matsuda, M., Cao, H. B., Ishiwata, S., and Tokura, Y., Magnetic Reversal of Electric Polarization with Fixed Chirality of Magnetic Structure in a Chiral-Lattice Helimagnet $MnSb_2O_6$, *Phys. Rev. Lett.*, **117**, 047201 (2016).

[36] Westin, G. and Grins, J., Rutile-Type $Mn_{1-x}Sb_{1+x}O_4$ Phases, $0 \leq x \leq 1/3$, Synthesized by the Sol-Gel Technique, *Acta Chemica Scandinavica*, **47**, 1053 (1993).

[37] Donaldson, J. D., Kjekshus, A., Nicholson, D. G., and Rakke, T., Properties of Sb-Compounds with Rutile-like Structure, *Acta Chemica Scandinavica*, **29**, 803 (1975).

[38] Byström, A., Hök, B., and Mason, B., The Crystal Structure of Zinc Metantimonate and Similar Compounds, *Ark. Kemi Mineral. Geol.*, **15** (1941).

[39] Berlepsch, P., Armbruster, T., Brugger, J., Criddle, A. J., and Graeser, S., Tripuhyite, $FeSbO_4$, revisited, *Mineralogical Magazine*, **67**, 31 (2003).

[40] Huang, Y. and Ruiz, P., The nature of antimony-enriched surface layer of Fe-Sb mixed oxides, *Applied Surface Science*, **252**(22), 7849 (2006).

[41] Prokofiev, A. V., Ritter, F., Assmus, W., Gibson, B. J., and Kremer, R. K., Crystal growth and characterization of the magnetic properties of $CuSb_2O_6$, *Journal of Crystal Growth*, **247**(34), 457 (2003).

[42] Tanaka, I., Kanai, H., and Kojima, H., The growth of tapiolite ($FeTa_2O_6$) single crystals by the floating zone method, *Journal of Crystal Growth*, **73**(1), 175 (1985).

[43] Cullity, B. D., *Elements of X-Ray Diffraction*, Addison-Wesley Publishing Company, Inc., 2 edition (1978).

[44] Wilkins, S., *Qlaue (Version 0.2) [CAD]* (2011).

[45] Dirac, P. A. M., Quantum Mechanics of Many-Electron Systems, *Proceedings of the Royal Society of London A: Mathematical, Physical and Engineering Sciences*, **123**(792), 714 (1929).

[46] Eicher, S. M., *Quasi Two Dimensional Magnetic Properties of the Tri-Rutile Phases MTa_2O_6, M = V, Fe, Co, Ni*, Ph.D. thesis, McMaster University (1984).

[47] Carlin, R., *Magnetochemistry*, Springer-Verlag (1986).

[48] Landau, L. D. and Lifshitz, E. M., *Statistical Physics*, Pergamon Press, 3 edition (1980).

[49] Onsager, L., Crystal Statistics. I. A Two-Dimensional Model with an Order-Disorder Transition, *Phys. Rev.*, **65**, 117 (1944).

[50] Mermin, N. D. and Wagner, H., Absence of Ferromagnetism or Antiferromagnetism in One- or Two-Dimensional Isotropic Heisenberg Models, *Phys. Rev. Lett.*, **17**, 1133 (1966).

[51] Giamarchi, T., *Quantum Physics in One Dimension*, Claredon Press, Oxford (2003).

[52] Kittel, C., *Introduction to Solid State Physics*, Wiley, New York, 7 edition (1996).

[53] Bonner, J. C. and Fisher, M. E., Linear Magnetic Chains with Anisotropic Coupling, *Phys. Rev.*, **135**, A640 (1964).

[54] Eggert, S., Affleck, I., and Takahashi, M., Susceptibility of the spin 1/2 Heisenberg antiferromagnetic chain, *Phys. Rev. Lett.*, **73**, 332 (1994).

[55] Johnston, D. C., Kremer, R. K., Troyer, M., Wang, X., Klümper, A., Bud'ko, S. L., Panchula, A. F., and Canfield, P. C., Thermodynamics of spin $S = 1/2$ antiferromagnetic uniform and alternating-exchange Heisenberg chains, *Phys. Rev. B*, **61**, 9558 (2000).

[56] Klümper, A., The spin-1/2 Heisenberg chain: thermodynamics, quantum criticality and spin-Peierls exponents, *Eur. Phys. J. B*, **5**(3), 677 (1998).

[57] Hall, J. W., *The magnetic properties of copper cluster complexes*, Ph.D. thesis, University of North Carolina at Chapel Hill (1977).

[58] Hatfield, W. E., New magnetic and structural results for uniformly spaced, alternatingly spaced, and ladderlike copper (II) linear chain compounds (invited), *Journal of Applied Physics*, **52**(3), 1985 (1981).

[59] Watanabe, T., Magnetic Properties of $NiSO_4{\cdot}7H_2O$ and α-$NiSO_4{\cdot}6H_2O$ at Low Temperatures, *Journal of the Physical Society of Japan*, **17**(12), 1856 (1962).

[60] Janicki, J. and Troc, R., Quasi-one-dimensional magnetic properties of the $(In;Sc;Lu;Y)_2Cu_2O_5$ oxides, *Journal of Physics: Condensed Matter*, **4**(29), 6267 (1992).

[61] Haldane, F. D. M., Nonlinear Field Theory of Large-Spin Heisenberg Antiferromagnets: Semiclassically Quantized Solitons of the One-Dimensional Easy-Axis Néel State, *Phys. Rev. Lett.*, **50**, 1153 (1983).

[62] Botet, R., Jullien, R., and Kolb, M., Finite-size-scaling study of the spin-1 Heisenberg-Ising chain with uniaxial anisotropy, *Phys. Rev. B*, **28**, 3914 (1983).

[63] Renard, J. P., Verdaguer, M., Regnault, L. P., Erkelens, W. A. C., Rossat-Mignod, J., and Stirling, W. G., Presumption for a Quantum Energy Gap in the Quasi-One-Dimensional S = 1 Heisenberg Antiferromagnet $Ni(C_2H_8N_2)_2NO_2(ClO_4)$, *EPL (Europhysics Letters)*, **3**(8), 945 (1987).

[64] Souletie, J., Drillon, M., Rabu, P., and Pati, S. K., Antiferromagnetic Heisenberg spin-1 chain: Magnetic susceptibility of the Haldane chain described using scaling, *Phys. Rev. B*, **70**, 054410 (2004).

[65] White, S. R., Density matrix formulation for quantum renormalization groups, *Phys. Rev. Lett.*, **69**, 2863 (1992).

[66] Yamashita, M., Ishii, T., and Matsuzaka, H., Haldane gap systems, *Coordination Chemistry Reviews*, **198**(1), 347 (2000).

[67] Coombes, D., Xiang, T., and Gehring, G. A., Calculation of the susceptibility of the S = 1 antiferromagnetic Heisenberg chain with single-ion anisotropy using the transfer matrix renormalization group method, *Journal of Physics: Condensed Matter*, **10**(10), L159 (1998).

[68] Regnault, L. P., Zaliznyak, I. A., and Meshkov, S. V., Thermodynamic properties of the Haldane spin chain: a statistical model for the elementary excitations, *Journal of Physics: Condensed Matter*, **5**(50), L677 (1993).

[69] White, S. R. and Huse, D. A., Numerical renormalization-group study of low-lying eigenstates of the antiferromagnetic S=1 Heisenberg chain, *Phys. Rev. B*, **48**, 3844 (1993).

[70] Sørensen, E. S. and Affleck, I., Large-scale numerical evidence for Bose condensation in the S=1 antiferromagnetic chain in a strong field, *Phys. Rev. Lett.*, **71**, 1633 (1993).

[71] Carlin, R. L. and van Duyneveldt, A. J., *Magnetic Properties of Transition Metal Compounds*, volume 3, Springer, New York (1977).

[72] Fisher, M. E., Magnetism in One-Dimensional Systems-The Heisenberg Model for Infinite Spin, *American Journal of Physics*, **32**(5), 343 (1964).

[73] Law, J. M., Benner, H., and Kremer, R. K., Padé approximations for the magnetic susceptibilities of Heisenberg antiferromagnetic spin chains for various spin values, *Journal of Physics: Condensed Matter*, **25**(6), 065601 (2013).

[74] Lines, M. E., The quadratic-layer antiferromagnet, *Journal of Physics and Chemistry of Solids*, **31**(1), 101 (1970).

[75] de Jongh, L. J. and Miedema, A. R., Experiments on simple magnetic model systems, *Advances in Physics*, **23**(1), 1 (1974).

[76] Tari, A., *The Specific Heat of Matter at Low Temperatures*, Imperial College Press, London (2003).

[77] *Physical Property Measurement System: Vibrating Sample Magnetometer (VSM) Option User's Manual*, first edition (2003).

[78] *Physical Property Measurement System: Hardware Manual*, third edition (2000).

[79] White, B. D., *Application of high-resolution dilatometry to the study of critical phenomena in antiferromagnetic systems*, Ph.D. thesis, Montana State University (2010).

[80] Blundell, S., *Magnetism in Condensed Matter*, Oxford University Press (2001).

[81] Gupta, R. R., *Diamagnetische Suszeptibilität*, volume 16 of *Landolt-Börnstein, New Series II*, Springer-Verlag, Heidelberg (1986).

[82] Ashcroft, N. and Mermin, N., *Solid State Physics*, Holt, Rinehart and Winston (1976).

[83] dos Santos, E. G. S., *Estudo teórico e experimental das propriedades magnéticas de óxidos de metais de transição quase-bidimensionais do tipo AB_2O_6*, Ph.D. thesis, Université de Grenoble (2012).

[84] Kato, M., Hatazaki, A., Yoshimura, K., and Kosuge, K., One-dimensional magnetic behavior of $CuSb_2O_6$, *Physica B: Condensed Matter*, **281282**(0), 663 (2000).

[85] Bersuker, I. B., *Electronic Structure and Properties of Transition Metal Compounds: Introduction to the Theory*, Wiley, New York, 2 edition (2010).

[86] Muraoka, Y., Idogaki, T., and Uryû, N., Susceptibility Analysis of Two-Dimensional Antiferromagnet $FeTa_2O_6$, *Journal of the Physical Society of Japan*, **57**(5), 1758 (1988).

[87] Morrish, A. H., *The Physical Principles of Magnetism*, Wiley-IEEE Press, 1 edition (2001).

[88] Giere, E.-O., Brahimi, A., Deiseroth, H., and Reinen, D., The Geometry and Electronic Structure of the Cu^{2+} Polyhedra in Trirutile-Type Compounds $Zn(Mg)_{1x}Cu_xSb_2O_6$ and the Dimorphism of $CuSb_2O_6$: A Solid State and {EPR} Study, *Journal of Solid State Chemistry*, **131**(2), 263 (1997).

[89] Chung, E. M. L., Lees, M. R., McIntyre, G. J., Wilkinson, C., Balakrishnan, G., Hague, J. P., Visser, D., and Paul, D. M., Magnetic properties of tapiolite ($FeTa_2O_6$); a quasi two-dimensional (2D) antiferromagnet, *Journal of Physics: Condensed Matter*, **16**(43), 7837 (2004).

[90] Werner, J., Koo, C., Klingeler, R., Vasiliev, A. N., Ovchenkov, Y. A., Polovkova, A. S., Raganyan, G. V., and Zvereva, E. A., Magnetic anisotropy and the phase diagram of chiral $MnSb_2O_6$, *Phys. Rev. B*, **94**, 104408 (2016).

[91] Date, M. and Nagata, K., Antiferromagnetic Resonance in Hydrated Copper Salts, *Journal of Applied Physics*, **34**(4), 1038 (1963).

[92] Paduan-Filho, A., Becerra, C. C., and Palacio, F., Hysteresis at the spin-flop transition in the antiferromagnets $K_2Fe(Cl_{1-x}Br_x)_5{\cdot}H_2O$, *Phys. Rev. B*, **43**, 11107 (1991).

[93] Anderson, F. B. and Callen, H. B., Statistical Mechanics and Field-Induced Phase Transitions of the Heisenberg Antiferromagnet, *Phys. Rev.*, **136**, A1068 (1964).

[94] Yung-Li, W. and Callen, H. B., Spin waves in the spin-flop phase of an antiferromagnet, and metastability of the spin-flop transition, *Journal of Physics and Chemistry of Solids*, **25**(12), 1459 (1964).

[95] Keffer, F. and Chow, H., Dynamics of the Antiferromagnetic Spin-Flop Transition, *Phys. Rev. Lett.*, **31**, 1061 (1973).

[96] Phaff, A. C., Swuste, C. H. W., Kopinga, K., and de Jonge, W. J. M., Anomalous AFMR in some quasi-one-dimensional Mn^{2+} compounds, *Journal of Physics C: Solid State Physics*, **16**(34), 6635 (1983).

[97] Shannon, R. D., Revised effective ionic radii and systematic studies of interatomic distances in halides and chalcogenides, *Acta Crystallographica Section A*, **32**(5), 751 (1976).

[98] *Physical Property Measurement System: Heat Capacity Option User's Manual*, tenth edition (2003).

[99] Rohlf, J. W., *Modern Physics from α to Z^0*, John Wiley & Sons, Inc. (1994).

[100] Fisher, M. E., Relation between the specific heat and susceptibility of an antiferromagnet, *Philosophical Magazine*, **7**(82), 1731 (1962).

[101] Kenzelmann, M., Coldea, R., Tennant, D. A., Visser, D., Hofmann, M., Smeibidl, P., and Tylczynski, Z., Order-to-disorder transition in the XY-like quantum magnet Cs_2CoCl_4 induced by noncommuting applied fields, *Phys. Rev. B*, **65**, 144432 (2002).

[102] Dmitriev, D. and Krivnov, V., Quasi-one-dimensional anisotropic Heisenberg model in a transverse magnetic field, *Journal of Experimental and Theoretical Physics Letters*, **80**(5), 303 (2004).

[103] Kurmann, J., Müller, G., Thomas, H., Puga, M. W., and Beck, H., Anisotropic quantum spin chains, *Journal of Applied Physics*, **52**(3), 1968 (1981).

[104] Flowers, B. H. and Mendoza, E., *Properties of Matter*, John Wiley & Sons Ltd. (1970).

[105] Grüneisen, E., *Handbuch der Physik*, volume 10, Berlin: Springer (1926).

[106] Buckingham, D. T. W., Masunaga, S. H., Gile, F. C., and Neumeier, J. J., High-Resolution Thermal Expansion Measurements of H_2O Ice (2014), American Physical Society March Meeting, Denver CO.

[107] Barrera, G. D., Bruno, J. A. O., Barron, T. H. K., and Allan, N. L., Negative Thermal Expansion, *Journal of Physics: Condensed Matter*, **17**(4), R217 (2005).

[108] James, J. D., Spittle, J. A., Brown, S. G. R., and Evans, R. W., A review of measurement techniques for the thermal expansion coefficient of metals and alloys at elevated temperatures, *Measurement Science and Technology*, **12**(3), R1 (2001).

[109] Neumeier, J. J., Bollinger, R. K., Timmins, G. E., Lane, C. R., Krogstad, R. D., and Macaluso, J., Capacitive-based dilatometer cell constructed of fused quartz for measuring the thermal expansion of solids, *Review of Scientific Instruments*, **79**(3), 033903 (2008).

[110] Souza, J. A., Yu, Y.-K., Neumeier, J. J., Terashita, H., and Jardim, R. F., Method for Analyzing Second-Order Phase Transitions: Application to the Ferromagnetic Transition of a Polaronic System, *Phys. Rev. Lett.*, **94**, 207209 (2005).

[111] Stanley, H. E., *Introduction to Phase Transitions and Critical Phenomena*, The International Series of Monographs on Physics, Oxford University Press (1971).

[112] Fisher, M. E., The theory of equilibrium critical phenomena, *Reports on Progress in Physics*, **30**(2), 615 (1967).

[113] Kadanoff, L. P., Götze, W., Hamblen, D., Hecht, R., Lewis, E. A. S., Palciauskas, V. V., Rayl, M., Swift, J., Aspnes, D., and Kane, J., Static Phenomena Near Critical Points: Theory and Experiment, *Rev. Mod. Phys.*, **39**, 395 (1967).

[114] Kornblit, A. and Ahlers, G., Heat Capacity of $RbMnF_3$ near the Antiferromagnetic Transition Temperature, *Phys. Rev. B*, **8**, 5163 (1973).

[115] Getzlaff, M., *Fundamentals of Magnetism*, Springer-Verlag Berlin Heidelberg (2008).

[116] Liu, A. J. and Fisher, M. E., The three-dimensional Ising model revisited numerically, *Physica A: Statistical Mechanics and its Applications*, **156**(1), 35 (1989).

[117] Domb, C. and Lebowitz, J. L., *Phase Transitions and Critical Phenomena*, volume 14, Academic Press (1991).

[118] Weiss, P. and Piccard, A., Le phénomène magnétocalorique, *J. Phys. Theor. Appl.*, **7**(1), 103 (1917).

[119] Fries, M., Skokov, K. P., Karpenkov, D. Y., Franco, V., Ener, S., and Gutfleisch, O., The influence of magnetocrystalline anisotropy on the magnetocaloric effect: A case study on Co_2B, *Applied Physics Letters*, **109**(23), 232406 (2016).

[120] Villain, J. and Loveluck, J.M., Néel temperature of a low-dimensional antiferromagnet in a magnetic field, *J. Physique Lett.*, **38**(2), 77 (1977).

[121] Boersma, F., Cooper, D. M., de Jonge, W. J. M., Dickson, D. P. E., Johnson, C. E., and Tinus, A. M. C., Variation of the Néel temperature of the one-dimensional antiferromagnet K_2FeF_5 with applied field, *Journal of Physics C: Solid State Physics*, **15**(19), 4141 (1982).

[122] Blume, M., Heller, P., and Lurie, N. A., Classical one-dimensional Heisenberg magnet in an applied field, *Phys. Rev. B*, **11**, 4483 (1975).

[123] Oguchi, T. and Blume, M., Theory of the Field Dependence of the Néel Temperature in Quasi One-Dimensional Antiferromagnets, *Journal of the Physical Society of Japan*, **50**(8), 2547 (1981).

[124] Singh, B. B., Singh, H. S., Gupta, G. P., and Lal, K. C., The anisotropy and field dependence of the Neel temperature in pseudo-one-dimensional antiferromagnetic systems, *Journal of Physics C: Solid State Physics*, **18**(10), 2171 (1985).

[125] Oguchi, T., Exchange Interactions in $Cu(NH_3)_4SO_4{\cdot}H_2O$, *Phys. Rev.*, **133**, A1098 (1964).

[126] Lines, M. E., Green Functions in the Theory of Antiferromagnetism, *Phys. Rev.*, **135**, A1336 (1964).

[127] Joenk, R. J., Magnetic Field Dependence of Thermodynamic Properties of Antiferromagnets; Adiabatic Magnetization, *Phys. Rev.*, **128**, 1634 (1962).

[128] de Jonge, W. J. M., Hijmans, J. P. A. M., Boersma, F., Schouten, J. C., and Kopinga, K., Field dependence of the Néel temperature in pseudo-one-dimensional Heisenberg systems, *Phys. Rev. B*, **17**, 2922 (1978).

[129] Gschneidner Jr., K. A., Pecharsky, V. K., and Tsokol, A. O., Recent developments in magnetocaloric materials, *Reports on Progress in Physics*, **68**(6), 1479 (2005).

[130] Gschneidner Jr., K. A. and Pecharsky, V. K., Magnetocaloric Materials, *Annu. Rev. Mater. Sci.*, **30**(1), 387 (2000).

[131] Wolf, B., Tsui, Y., Jaiswal-Nagar, D., Tutsch, U., Honecker, A., Remović-Langer, K., Hofmann, G., Prokofiev, A., Assmus, W., Donath, G., and Lang, M., Magnetocaloric effect and magnetic cooling near a field-induced quantum-critical point, *Proceedings of the National Academy of Sciences*, **108**(17), 6862 (2011).

[132] Zhitomirsky, M. E. and Honecker, A., Magnetocaloric effect in one-dimensional antiferromagnets, *Journal of Statistical Mechanics: Theory and Experiment*, **2004**(07), P07012 (2004).

[133] Honecker, A. and Wessel, S., Magnetocaloric effect in two-dimensional spin-1/2 antiferromagnets, *Physica B: Condensed Matter*, **378380**(0), 1098 (2006).

[134] Derzhko, O. and Richter, J., Universal low-temperature behavior of frustrated quantum antiferromagnets in the vicinity of the saturation field, *The European Physical Journal B - Condensed Matter and Complex Systems*, **52**(1), 23 (2006).

[135] Jafari, R., Thermodynamic properties of the one-dimensional extended quantum compass model in the presence of a transverse field, *The European Physical Journal B*, **85**(5), 167 (2012).

[136] Munsie, T., Millington, A., Dube, P., Dabkowska, H., Britten, J., Luke, G., and Greedan, J., Crystal growth and magnetic characterization of a tetragonal polymorph of $NiNb_2O_6$, *Journal of Solid State Chemistry*, **236**, 19 (2016).

[137] Kroemer, H., All that Glitters isn't Silicon, *in Future Trends in Microelectronics*, volume 323 of *NATO ASI Series E*, edited by S. Luryi, J. Xu, and A. Zaslavsky, p. 1, Kluwer Academic Publishers, Dordrecht (1996).

[138] Ercit, T. S., Foord, E. E., and Fitzpatrick, J. J., Ordonezite from the Theodoso Soto Mine, Sapioris, Durango, Mexico: New Data and Structure Refinement, *Canadian Mineralogist*, **40**, 1207 (2002).

[139] Nakua, A., Yun, H., Reimers, J. N., Greedan, J. E., and Stager, C. V., Crystal structure, short range and long range magnetic ordering in $CuSb_2O_6$, *Journal of Solid State Chemistry*, **91**(1), 105 (1991).

[140] Müller-Buschbaum, H. K. and Wichmann, R., Kristallstrukturuntersuchung an $NiTa_2O_6$-Einkristallen Ein Beitrag zur Systematik geordneter und ungeordneter Oxometallate: AB_2O_6 und ABO_4, *Zeitschrift für anorganische und allgemeine Chemie*, **536**(5), 15 (1986).

[141] Peters, E. and Müller-Buschbaum, H. K., Hochtemperatursynthese und Kristallchemie der Oxotantalate $Cr^{2+}_{0.761}Ta_{2.095}O_6$ und $FeTa_2O_6$, *Zeitschrift für Naturforschung, B: Chemical Sciences*, **50**, 712 (1995).

[142] Vincent, H., Turrillas, X., and Rasines, I., A novel structural type of hexagonal closest packing the ternary oxide, β-$MnSb_2O_6$, *Materials Research Bulletin*, **22**, 1369 (1987).